

THESE DE DOCTORAT DE

L'UNIVERSITE
DE BRETAGNE OCCIDENTALE
COMUE UNIVERSITE BRETAGNE LOIRE

ECOLE DOCTORALE N°598

Sciences de la mer et du littoral

Spécialité : *Océanographie physique et Environnement*

Par

Benjamin I. Barton

**Climate change in the Barents Sea :
Ice-ocean interactions, water mass formation and variability**

Thèse présentée et soutenue à Plouzané, le 10 octobre 2019

Unité de recherche :

Laboratoire d'Océanographie Physique et Spatiale

Rapporteurs avant soutenance : Composition du jury :

Gilles REVERDIN Directeur de recherche CNRS
LOCEAN, Univ. Paris VI
Penny HOLLIDAY Professor
NOC, Southampton

Gilles REVERDIN Directeur de recherche CNRS
LOCEAN, Univ. Paris VI
Penny HOLLIDAY Professor
NOC, Southampton
Bernard BARNIER Directeur de recherche CNRS
MEOM/IGE, Grenoble

Président du Jury :

Xavier CARTON

Professeur des Universités
LOPS, UBO, Brest

Directrice de Thèse :

Anne-Marie TREGUIER

Directrice de recherche CNRS
LOPS, Brest

Co-encadrante :

Camille LIQUE

Chercheur IFREMER
LOPS, Brest

Yueng-Djern LENN

Senior Lecturer
SOS, Bangor University

Remerciements

I am grateful for the PhD funding I received through the joint UK-France PhD program by DGA/Dstl, and overseen by Carole Nahum and Timothy Clarke. I am also grateful for the funding from EU Horizon 2020-funded APPLICATE project to attend the Polar Prediction School 2018, funding from FAMOS to attend the FAMOS Arctic Ocean conference and funding from NERC Changing Arctic Ocean grant NE/R01275X/1 to be part of the SODA expedition on the RV Sikuliaq to the Beaufort Sea.

I would like to thank my supervisors Camille and Yueng for their support of my studies and guidance through the academic maze. In their own ways they have overseen my development and helped me confront the weaknesses in my skills and character. There are times when I became distracted by interesting data or my thoughts strayed for the path of logic but my supervisors gave me the nudges I needed to guide me through.

I would like to acknowledge the Ocean Modelling team (Verena Haid and Claude Talandier) for their work producing the Arctic Ocean regional NEMO model. I would like to thank Heather Regan for discussions of my work and for providing support in trying times. I am grateful to the kind administrative staff at UBO for their patience with my French language. The staff at Bangor University have been very accommodating of any requests of access to services or papers.

Undertaking PhD was something I'd wanted to do since high school, of course that path had a few wiggles in it but somehow I've got there in the end. Those wiggles have taken many forms, including the time I've spent in Bangor and Brest or the excursions during my studies to conferences, a Swedish summer school and a Arctic cruise. I'd like to thank all the friends I've made along this journey especially those in Brest who welcomed me into their international community and showed me their local traditions. I appreciate the invaluable programming and data analysis taught to me by Steve Spall before I started the PhD. I would like to thank Nicolas Bouhier for help with translating parts of my thesis to French. Thanks to Guillaume Boutin for the latex thesis template. I would also like to thank my friends Mike Jones and Laurence Jones who helped keep me grounded. Finally I am grateful to my parents who were always there for me with wise counsel and sympathy, they have supported and encouraged my interest in science all the way.

"It is not our part to master all the tides of the world, but to do what is in us for the succour of those years wherein we are set, uprooting the evil in the fields that we know, so that those who live after may have clean earth to till. What weather they shall have is not ours to rule."
Gandalf, J.R.R. Tolkien, *The Return of the King*

Table des matières

1	Introduction	11
1.1	Overview	12
1.2	Literature Review	13
1.2.1	Sea ice	13
1.2.2	Water Masses and Circulation	14
1.2.3	Atmosphere	19
1.2.4	Arctic Ocean and Norwegian Sea	20
1.3	Motivation	21
1.3.1	Remote Influence of the Barents Sea Processes	21
1.3.2	Local Influence of Barents Sea Processes	22
1.4	Aims and Objectives	25
1.4.1	Thesis Structure	27
2	Observed atlantification of the Barents Sea	29
2.1	Introduction	30
2.2	Data and Methods	32
2.2.1	Datasets	32
2.2.2	Methods	33
2.3	Seasonal and Interannual Variability of SST	34
2.4	The Polar Front's Constraint on the Sea Ice Edge	38
2.5	Atlantification and Implications	43
2.6	Conclusion	45
3	Satellite water mass properties	47
3.1	Introduction	48
3.2	Data and Methods	49
3.2.1	Data	49
3.2.2	Methods	51
3.3	Estimation of the BSW properties from satellite datasets	54
3.4	Understanding the variability of BSW	61
3.5	Conclusion	64
4	Model study of Barents Sea Water variability	67
4.1	Introduction	68
4.2	Data and Methods	70
4.2.1	Model Simulation	70
4.2.2	Observational Datasets	71
4.2.3	Methods	71
4.3	Model Evaluation	72
4.4	Quantifying Variability in BSW Properties	75
4.4.1	Volume and Properties	75
4.4.2	Transport and Flux Budget	78
4.5	Notable Events in BSW Variability	82

4.6	The Emergence of a Regime Shift	83
4.7	Conclusion	87
5	Summary and Synthesis	89
5.1	Summary	90
5.1.1	Chapter 2 : Observed atlantification of the Barents Sea	90
5.1.2	Chapter 3 : Satellite water mass properties	91
5.1.3	Chapter 4 : Model study of Barents Sea Water variability	93
5.2	Synthesis	93
5.3	Future Work	94
6	Résumé Étendu en Français	97
6.1	Résumé	98
6.1.1	Chapitre 2 : Atlantification observée dans la Mer de Barents	98
6.1.2	Chapitre 3 : Caractéristiques des masses d'eau observées par satellite . . .	101
6.1.3	Chapitre 4 : Etude par modélisation de la variabilité de la Mer de Barents	101
6.2	Synthèse	102
6.3	Perspectives	103
	Bibliography	105
A	Supplementary Materials	119
A.1	Satellite Based T-S Profiles	120

Table des figures

1.1	Map of North Atlantic and Arctic Oceans	12
1.2	Northern Hemisphere sea ice extent, 1979-2016	13
1.3	Schematic map of the major currents	15
1.4	Maps of water mass occurrence in the Barents Sea	16
1.5	Multi-decadal temporal variability in the Barents Sea sea ice and ocean temperature	18
1.6	Time series of temperature and salinity at the Barents Sea Opening	19
1.7	Observed and simulated change in winter surface air temperature (SAT) and atmospheric circulation associated with sea-ice retreat in the Barents-Kara region .	23
1.8	Potential temperature and salinity distributions in the Eurasian Basin	24
1.9	Interannual variability of Polar Lows over the Nordic Seas	25
1.10	Time series of biogeochemical properties at the Barents Sea Opening	26
2.1	Map showing the locations of boxes and transects used	30
2.2	SST seasonal climatology and fronts from 2005 to 2016	35
2.3	SST seasonal climatology and front from 1985 to 2004	36
2.4	Empirical Orthogonal Function analysis of SST	37
2.5	Spatial variability in SST trend in the Barents Sea	38
2.6	Transect and T-S properties of water mass properties through the eastern Barents Sea	40
2.7	Hovöller of the Polar Front latitude, sea ice edge and timeseries of BSW properties	41
3.1	Average and standard deviation in steric height, heat and freshwater content . . .	49
3.2	Regression of satellite steric height with EN4 steric height between various integration depths to the surface	53
3.3	Regression of satellite SST with <i>in situ</i> OID heat content	54
3.4	Timeseries of SSH, eustatic height, steric height, thermosteric and halosteric heights	56
3.5	Mean seasonal cycle and interannual variability in satellite water properties . . .	57
3.6	Regression of satellite SSS with <i>in situ</i> OID freshwater content	59
3.7	Regression of satellite halosteric height with EN4 halosteric height	60
3.8	Interannual variability in satellite water properties and fluxes over 2003 to 2013 .	62
3.9	Mean seasonal cycle and interannual variability in surface fluxes and sea ice extent	63
4.1	T/S diagram showing water mass properties	69
4.2	Map of the box used in the budget calculation	70
4.3	Validation of sea ice extent, volume and heat transport through the BSO	73
4.4	Seasonal climatology of the gradient in SST from 2005 to 2014 for model and observations	74
4.5	Timeseries of water mass properties and volume in the Barents Sea	76
4.6	Hovmöller of interannual variability in stratification anomalies for temperature, salinity and density	78
4.7	Timeseries of surface fluxes in the Barents Sea	79
4.8	Ocean volume, heat and freshwater transport	80
4.9	Lead and lag regression values for combinations of properties and fluxes	84
4.10	Schematic of lead-lag regressions showing the propagation of anomalies	86

5.1	Schematic of the Polar Front	91
5.2	Multi-decadal temporal variability in the Barents Sea sea ice and temperature . .	92
6.1	Schéma du Front Polaire	99
6.2	Variabilité temporelle multi-décennale de la glace de mer et de la température de la Mer de Barents	100
A.1	Satellite based T-S profiles	121

Liste des tableaux

1.1	Definitions of the water masses	14
4.1	Table of water mass properties for the model and observations	68

Chapitre 1

Introduction

1.2 Literature Review

In this section we review a selection of literature following the main themes and physical phenomena running through this thesis as a whole. The aim of this section is to give a broad background and understanding of the state of published knowledge on the region and identify the gaps in the knowledge.

1.2.1 Sea ice

The Arctic air temperature is warming faster than the rest of the globe, known as Arctic amplification. Arctic amplification has been partly attributed to the loss of sea ice which causes a positive feedback, increasing the solar radiation absorbed here (Screen and Simmonds, 2010a). This amplified warming is predicted to cause September sea-ice-free conditions by the middle of the twenty first century (Wang and Overland, 2012; Snape, 2013; Notz and Stroeve, 2016). The Barents Sea has seen the largest decrease in yearly sea ice compared to the rest of the Arctic, primarily because of a decline in winter sea ice (Parkinson and Cavalieri, 2008; Onarheim et al., 2018) (Figure 1.2). This makes the Barents Sea marginal ice zone a useful region to analyse possible future ice free conditions in the Arctic Ocean.

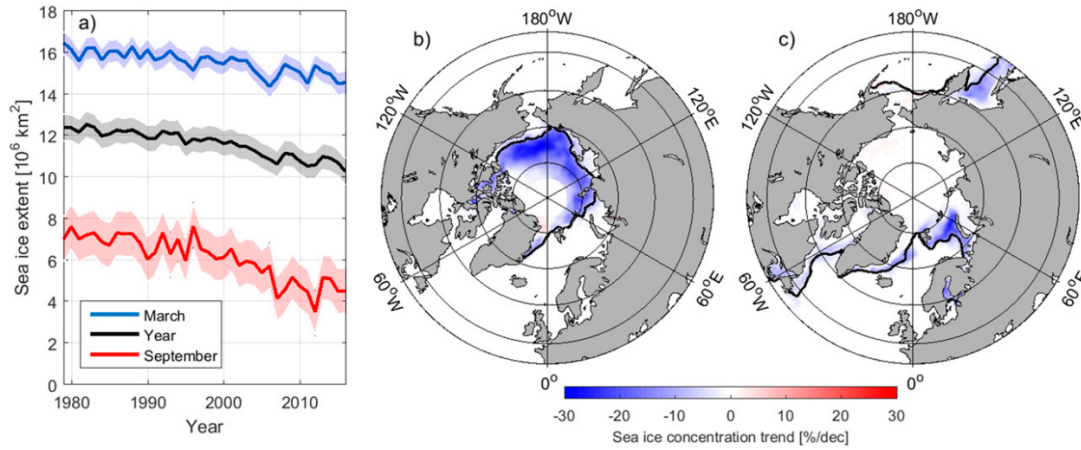


FIGURE 1.2 – (a) March (blue), September (red), and annual mean (black) Northern Hemisphere sea ice extent, 1979-2016. Shaded regions indicate plus and minus one standard deviation. Linear sea ice concentration trends ($\% \text{ decade}^{-1}$) in (b) September and (c) March, 1979-2016. Black contours show the mean sea ice edge. Figure from Onarheim et al. (2018).

In the Barents Sea, sea ice is seasonal, with a strong presence extending across the northern and south-eastern Barents Sea during winter and retreating to the north in the summer (Onarheim and Årthun, 2017) (Figure 1.2). Some sea ice volume forms locally within the Barents Sea, mostly around land and shallower bathymetric features (Gerland et al., 2008; Ivanov and Shapiro, 2005; Årthun et al., 2011; Ellingsen et al., 2009). Historically, the majority of interannual variability in sea ice volume comes from sea ice advected from the Eurasian Basin and Kara Sea (Kwok et al., 2005; Kwok, 2009; Ellingsen et al., 2009).

Between 1980 and 2015 the sea ice area has become more dependant on seasonal import as the summer sea ice extent minimum receded north of the Barents Sea and since 2005 import accounts for most of the sea ice area (Lind et al., 2018). The interplay between local formation and wind driven import is demonstrated by the first two empirical orthogonal function modes of sea ice concentration (Herbaut et al., 2015). This analysis shows sea ice concentration in the east is correlated with formation along Novaya Zemlya and easterly winds increasing or decreasing export from the coastal formation region. Sea ice concentration in the north shows variability based on the import of sea ice, which is correlated with variability in geostrophic winds on a daily basis and cyclones on an interannual basis (Kwok et al., 2005; Ellingsen et al., 2009; Sorteberg

and Kvingedal, 2006; Herbaut et al., 2015). However, total sea ice extent is a balance between the wind driven import and the local melting (Lind et al., 2018; Steele and Ermold, 2015). In the Barents Sea, this means interannual variability in ice extent is correlated with the temperature of advected Atlantic Water (AW) (Onarheim et al., 2015; Årthun et al., 2012).

Observations show there is a declining trend in Barents Sea sea ice area with a 50 % reduction between 1998 and 2008 (Årthun et al., 2012). A trend might be expected in winds driving reduced sea ice import, but there was no significant trend in the sea ice import from the Eurasian basin between 1979 and 2007 (Kwok, 2009). AW temperature does show a trend suggesting this is the cause (Årthun et al., 2012). The continuing loss of sea ice makes the remaining sea ice more mobile and vulnerable to atmospheric forcing and storms in the future (Simmonds and Keay, 2009).

1.2.2 Water Masses and Circulation

Several water masses are present in the Barents Sea. These are the relatively warm, saline Atlantic Water (AW); cool Barents Sea Water (BSW) that has intermediate salinity; relatively cool, fresh Arctic Water (ArW) and relatively warm, fresh Coastal Water (CW). The property boundaries between water masses are defined by literature-based estimates in Table 1.1.

TABLE 1.1 – Definitions of the water masses present in the Barents Sea used in this study, along with definitions used in previous studies. Note that Barents Sea Water can be referred to as Modified Atlantic Water in literature.

Water Mass	Source	Temperature	Salinity	Density
Atlantic Water (AW)	Present Study	T >3.0	S >35.0	
	Oziel et al. (2016)	T >3.0	S >34.8	
	Loeng (1991)	T >3.0	S >35.0	
Arctic Water (ArW)	Present Study	T <0.0	S <34.7	
	Oziel et al. (2016)	T <0.0	S <34.7	
	Loeng (1991)	T <0.0	34.3 <S <34.8	
Coastal Water (CW)	Present Study	T >2.0	S <34.7	
	Oziel et al. (2016)	T >3.0	S <34.4	
	Loeng (1991)	T >2.0	S <34.7	
Barents Sea Water (BSW)	Present Study	T <2.0	S >34.7	$\sigma >27.85$
	Schauer et al. (2002)			$\sigma >27.85$
	Oziel et al. (2016)	T <2.0	S >34.8	$\sigma >27.8$
	Loeng (1991)	-1.5 <T <2.0	34.7 <S <35.0	

The main current in the Barents Sea is the through-flow of AW (Figure 1.3). This current has a transport of 2.0 Sv in the BSO with 0.9 Sv of the inflow recirculating in Hopen Trench (Skagseth, 2008). The current brings a net 50 TW of heat into the Barents Sea (Skagseth, 2008). In addition, the Norwegian Coastal Current brings 1.25 Sv of CW into the Barents Sea with 20 TW of heat (Smedsrud et al., 2013, 2010). These estimates are based on 10 years of observational transport data. The estimates of BSW (modified AW) outflow through the BSX are based on one year of observations and model data. They suggest net transport of 1.6 Sv (2.3 to 2.6 Sv in models) and heat transport of -3.6 TW (7.4 to -5.6 in models) out of the the Barents Sea (Gammelsrød et al., 2009). These estimates cover a large range and are based on one year of data suggesting a need for improvment.

Between the water masses lie fronts which mostly keep AW in the south western Barents Sea, BSW in the Central Basin of the south eastern Barents Sea and ArW in the northern Barents Sea (Schauer et al., 2002; Oziel et al., 2016) (Figure 1.4). The Polar Front is an important feature of the Barents Sea because it is the boundary between the freshwater stratified ArW in the north and the more saline AW and BSW in the south (Våge et al., 2014; Harris et al., 1998). This front constrains the area for surface interaction of AW, BSW and ArW. The Polar Front in the western Barents Sea is consistent in its location along the south-eastern side of Spitsbergen Bank and

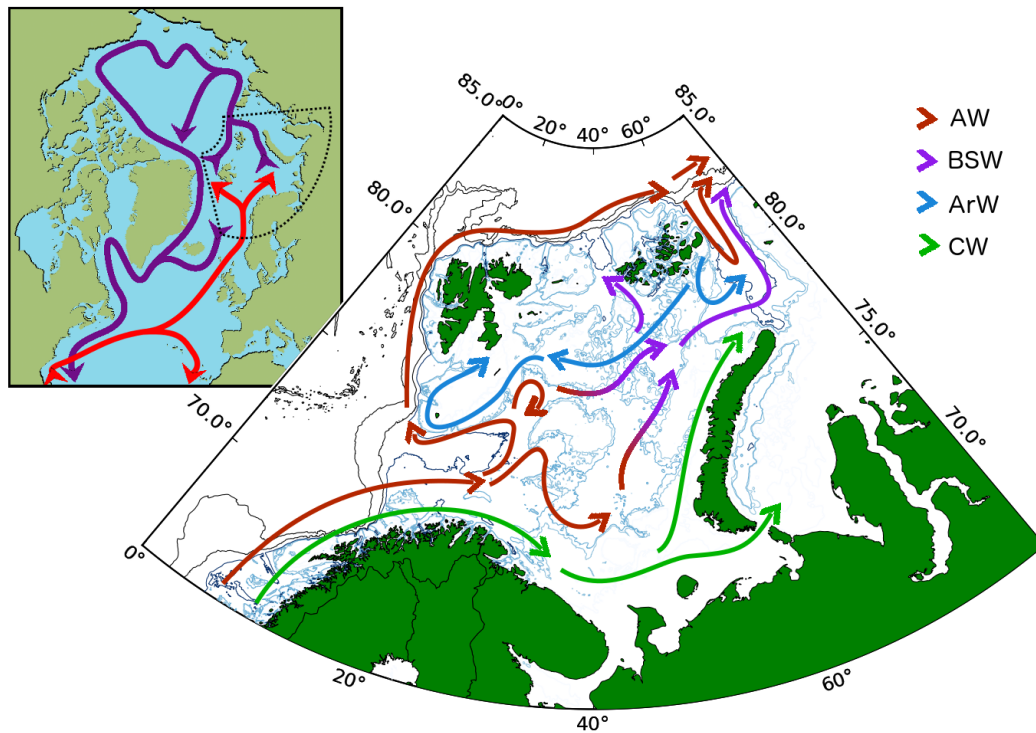


FIGURE 1.3 – Schematic map of the major currents. Inset of North Atlantic and Arctic shows AMOC where red arrows are currents in the warm upper ocean branches and purple arrows are the cooler, dense, deeper branches of circulation. Barents Sea circulation shows the transport routes of Atlantic Water (AW) the cooler Barents Sea Water (BSW), fresh Arctic Water (ArW) and Coastal Water (CW). Bathymetry is shown as contours at 100, 150, 200, 250, 300, 350, 400, 1000 and 2000 m.

along the south-western side of Great Bank (Johannessen and Foaster, 1978; Parsons et al., 1996; Fer and Drinkwater, 2014; Våge et al., 2014) (Figure 1.1). In the summer, the seasonal sea ice melts and a surface warm layer is formed. This traps the fresher sea ice melt water at the surface over the ArW and increases the salinity gradient at the front while maintaining the cross-front temperature gradient (Parsons et al., 1996). This section of the polar front in the western Barents Sea has been noted to be fixed to an isobath, though there are a range of isobaths suggested due to the way that the fronts tilt vertically; 100 – 150 m for the greatest subsurface density change (Johannessen and Foaster, 1978; Våge et al., 2014; Fer and Drinkwater, 2014) and 250 – 275 m for the location of the surface manifestation of the front (Harris et al., 1998; Gawarkiewicz and Plueddemann, 1995; Våge et al., 2014). Based on 25 years of hydrographic observations, it has also been suggested that this section of the front has some interannual variability and moves up and down the slope of Spitzbergen Bank (near Bear Island and Hopen Trench on Figure 1.1) (Ingvaldsen, 2005).

The Polar Front in the eastern Barents Sea has been more roughly defined than in the west, Li and McClimans (1998) for example leaves it undefined in the east. It is proposed that it extends southwards from Great Bank to Murmansk Rise and into the Central Basin (Smedsrud et al., 2010; Våge et al., 2014). As mentioned by Loeng (1991) there is significant variability in the location of the Polar Front in the eastern Barents Sea. This front has also been observed at its most northeasterly location near Ludlov Saddle (located between Great Bank and Novaya Zemlya on Figure 1.1) (Årthun et al., 2011; Oziel et al., 2016) (Figure 1.4). This variability is partly related to the way the front is reported i.e. whether it is a temperature gradient or a salinity gradient. As reported by Oziel et al. (2016), past 32 °E the front splits into a northern branch and a southern branch (Figure 1.4). The southern branch is the temperature dominated front and the

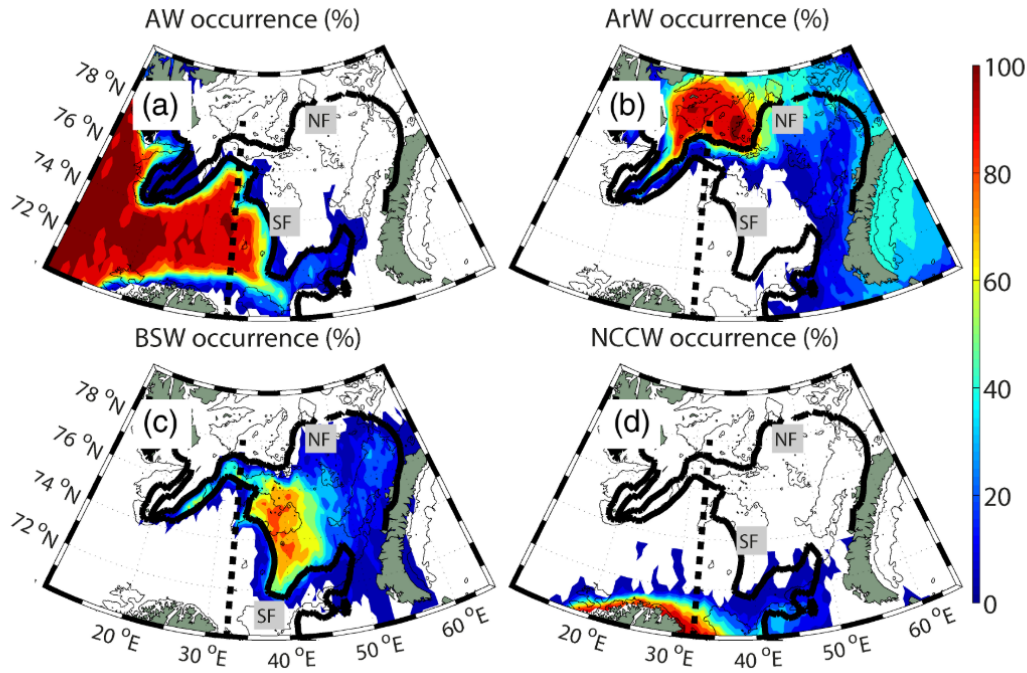


FIGURE 1.4 – Water Mass Occurrences (%) over the 1980-2011 period in August-September for the 50-100m layer. (a) Atlantic Water (AW), (b) Arctic Water (ArW) (c), Barents Sea Water (BSW), (d) Norwegian Current Coastal Water (NCCW). The Southern Front (SF) and Northern Front (NF) (bold black lines), the Vardø section (dashed line), and the 200m isobath (thin black line) are indicated. Figure from [Oziel et al. \(2016\)](#).

northern branch is the salinity dominated front. The interannual variability reported in these eastern fronts is related to changes in the temperature and volume of AW transported into the Barents Sea through the BSO ([Oziel et al., 2016](#)). These conclusions are based on isotherms and isohalines and require further investigation. The broad and rough location of the Polar Front in the eastern Barents Sea suggests it needs more work to understand it and constrain the surface area for atmospheric interaction of AW and BSW.

The bathymetric features of the Barents Sea strongly influence the currents. AW enters the Barents Sea through the BSO as a barotropic flow ([Loeng, 1991](#)). This AW follows several circulation pathways and is modified en route to St. Anna Trough where it enters the Arctic Ocean (Figure 1.3). These pathways include a recirculating branch in Hopen Trench and a Novaya Zemlya branch that crosses Murmansk Rise south of Central Bank (locations on Figure 1.1) ([Skagseth, 2008](#); [Ingvaldsen, 2005](#)). The Novaya Zemlya branch contours around the south-eastern side of Central Basin and stays west of Novaya Zemlya Bank producing cyclonic circulation in the Central Basin before flowing towards the BSX ([Ozhigin et al., 2000](#)). A few observation profiles and velocity from a survey suggest some BSW flows eastward between Central Bank and Great Bank ([Loeng, 1991](#); [Lind and Ingvaldsen, 2012](#); [Våge et al., 2014](#)) (Figure 1.4). There is also model and observational evidence that some BSW also flows from Hopen Trench into the northern Barents Sea forming a northern Franz-Josef Land branch ([Aksenov et al., 2010](#); [Lind and Ingvaldsen, 2012](#)). More evidence is required on the transport routes in the northern Barents Sea.

The Norwegian/Murman Coastal Current is a separate branch of warm CW entering the Barents Sea through the southern end of the BSO (Figure 1.3). This water mass is fresher than AW and contours the coast of Norway and Russia in transit through the Barents Sea ([Skagseth et al., 2011](#); [Schauer et al., 2002](#)). The destination of this current could be through the Kara Gate into the Kara Sea or along the coast of Novaya Zemlya but more observational evidence from current meters is required. A front should also exist between CW and AW but the location

of this Coastal Front and variability in the CW are poorly constrained.

This main volume transport route is from the BSO to the BSX and has been suggested to be subjected to strong bathymetric control by [Gawarkiewicz and Plueddemann \(1995\)](#). In their simplified two basin, H-shaped model of the Barents Sea system with a ridge in the middle, open boundaries and prescribed inflow on the western side, [Gawarkiewicz and Plueddemann \(1995\)](#) reproduced the observed barotropic transport pathways i.e. recirculation in the western basin and a portion of transport crossing the central ridge into the eastern basin. The minimum depth of the ridge sets the boundary for recirculation following Coriolis/Height (f/H) contours. In [Gawarkiewicz and Plueddemann \(1995\)](#)'s model, this flow structure conserves potential vorticity and produces a front across the ridge ([Gawarkiewicz and Plueddemann, 1995](#)). Conserving potential vorticity means the rotational tendency of the water stays proportional to the depth range it occupies. The BSW branch of AW has been suggested as a source of potential vorticity to the Arctic Basin using model analysis but the mechanism for its development requires further work ([Yang, 2005](#)).

In the northern Barents Sea, the upper water column is permanently stratified by relatively fresh and cold ArW ([Lind and Ingvaldsen, 2012](#)). The ArW enters the Barents Sea through the BSX but some also enters through the northern opening between Svalbard and Franz-Josef Land ([Loeng, 1991](#); [Gammelsrød et al., 2009](#)). ArW recirculates out through the BSX with net ArW transport close to zero ([Gammelsrød et al., 2009](#)). ArW is less dense than BSW and forms a stratified layer above it in the water column. Based on hydrographic profiles, water flows south-westward along the Persey Current south of Franz-Josef Land towards Spitsbergen Bank ([Loeng, 1991](#)) (Figure 1.4). Observations from a single velocity survey show the velocity of this current is 10 m s^{-1} ([Våge et al., 2014](#)). The addition of moored current meter observations would provide stronger evidence of the location and variability in this current.

In general, shelf seas have strong tidal dynamics compared to ocean basins because of their shallow bathymetry producing harmonic amplification of the various tidal constituents. Tides have been modelled in the Arctic with the Arctic Ocean Tidal Inverse Model (AOTIM-5) and the model suggests the western Barents Sea as one of the regions of the Arctic where mean tidal currents can reach 10 cm s^{-1} ([Padman and Erofeeva, 2004](#)). Observations show tidal currents up to 40 cm s^{-1} on the western slope of the BSO ([Skardhamar et al., 2015](#)), 20 cm s^{-1} on Great Bank ([Fer and Drinkwater, 2014](#)). The AOTIM-5 and observations suggest tidal currents up to 60 cm s^{-1} are present on Spitsbergen Bank ([Padman and Erofeeva, 2004](#); [Parsons et al., 1996](#)). Over the banks in the Barents Sea, the tides are important for mixing but do not alter the mean circulation or Polar Front location ([Fer and Drinkwater, 2014](#); [Våge et al., 2014](#)).

The water masses exhibit interannual variability within their defined classes (Table 1.1). There have been long term measurements of AW temperature (at the Kola Section), sea level pressure (SLP) and sea ice concentration within the Barents Sea which extend from the early 1900s ([Venegas and Mysak, 2000](#); [Levitus et al., 2009](#)). The SLP and sea ice concentration measurements show interannual variability with cycles of 6-7 years, 9-10 years, 16-20 years and 30-50 years ([Venegas and Mysak, 2000](#)) (Figure 1.5). The North Atlantic Oscillation (NAO) is large scale SLP pattern in the North Atlantic between the Icelandic Low and the Azores High, affecting westerly wind speeds ([van Loon and Rogers, 1978](#)). The 9-10 year cycle is suggested to be variability associated with the NAO's impact on the Norwegian Current. The 16-20 year cycle is suggested to be variability originating in the North Atlantic gyres. The Atlantic multi-decadal oscillation (AMO) index is a mode of natural variability in North Atlantic sea surface temperature (SST) ([Trenberth and Shea, 2006](#)). The 30 to 50 year cycle in sea ice concentration and SLP is also found in the Kola Section temperature timeseries and has been correlated with the AMO index ([Levitus et al., 2009](#); [Skagseth, 2008](#)) (Figure 1.5). However, the North Atlantic also shows a trend of increasing temperature throughout the observation time period from 1870-2005 which is removed from the AMO index ([Trenberth and Shea, 2006](#)). Between 1977 and 2004, the 3-year running mean of winter NAO index correlates with 3-year running mean AW temperature variability at the BSO, showing decadal variability in NAO is important for temperature ([Ingvaldsen, 2005](#)). Salinity has been recorded at the BSO section from 1965 to 2007 ([Skagseth, 2008](#)).

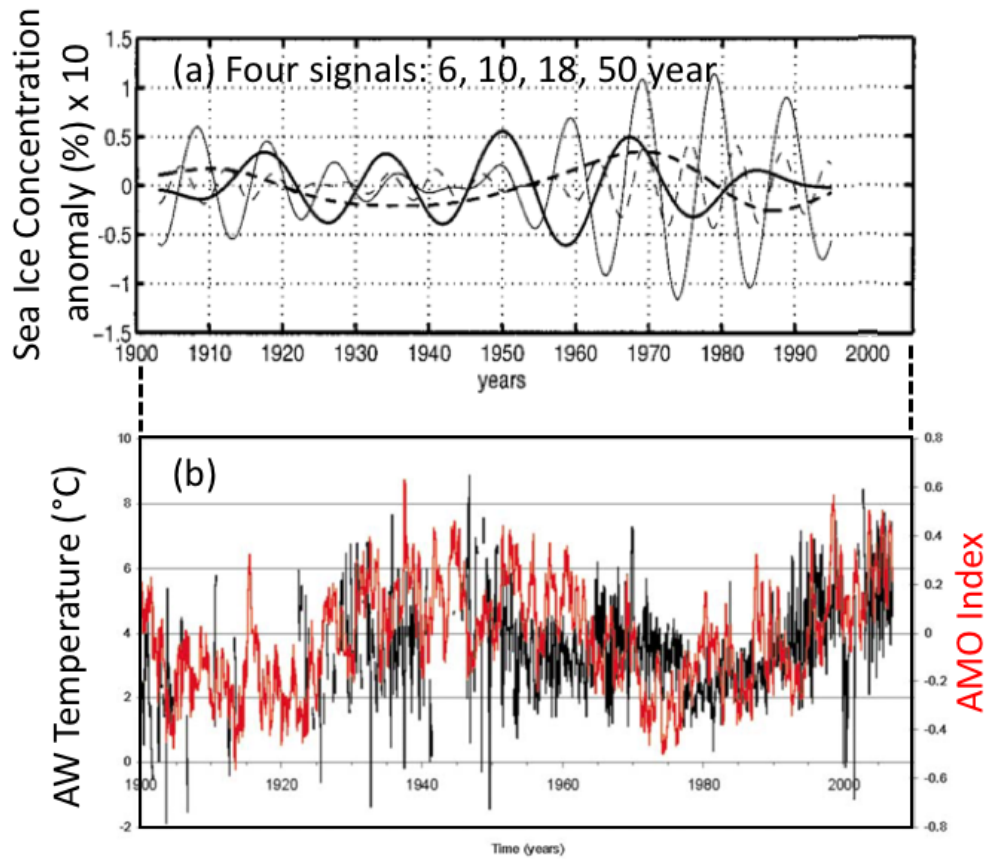


FIGURE 1.5 – Multi-decadal temporal variability in the Barents Sea : (a) the four dominant signals found the sea ice concentration in the Barents Sea between 35 °E and 75 °E. Each of the signals show a cycle with a different period that can be combined to reproduce the interannual variability (6-7 years, 9-10 years, 16-20 years and 30-50 years). (b) Atlantic Water (AW) temperature compiled from hydrographic profiles at 100-150 m for 11 - 57 °E, 69 - 78 °N. Atlantic Multi-decadal Oscillation (AMO) defined by detrended SST in the North Atlantic. The graphs are reproductions (a) sourced from [Venegas and Mysak \(2000\)](#), (b) sourced from [Levitus et al. \(2009\)](#).

(Figure 1.6). This salinity time series shows interannual variability at a similar time scale to the variability in temperature. This should be expected given the 9-10 year and 16-20 year cycles in temperature are advected ([Venegas and Mysak, 2000](#)). Multidecadal variability calculated with 4 to 6 year running mean in 25 years of salinity observations suggested this multidecadal variability is correlated with NAO ([Ingvaldsen, 2005](#)). The salinity timeseries also shows the Great Salinity Anomaly that was present in the 1970s Nordic Seas and produces a 0.2 salinity anomaly in the BSO ([Dickson et al., 1988](#)) (Figure 1.6).

Interannual variability in the temperature of ArW present in the Northern Barents Sea at 50 m depth shows correlation with BSW beneath it in the water column ([Lind and Ingvaldsen, 2012](#)). Salinity of the ArW is correlated with temperature of the underlying BSW ([Lind et al.,](#)

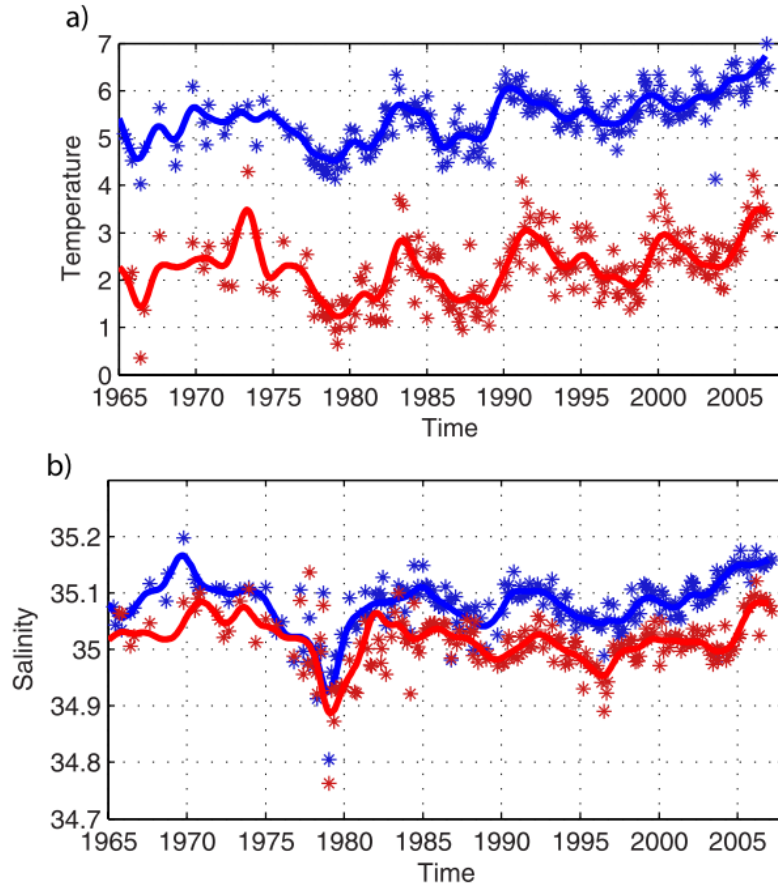


FIGURE 1.6 – Time series of (a) temperature and (b) salinity. The Atlantic water (blue) is defined as mean between 72-73 °N and 50-200 m and the outflow water in BSO (red) at 73.5 °N is defined as the mean from 300-450 m. The seasonality in the data is removed. The crosses are the raw data and the solid lines are low-pass filtered data applying a hamming window of 12 months. Figure from [Skagseth \(2008\)](#).

[2016](#)). This is because warm BSW mixes with ArW and melts more sea ice releasing freshwater. However, question remain about how BSW gets here and the variability in BSW properties. Between 2000 and 2015 there has also been a positive trend in the ArW temperature and salinity ([Lind et al., 2018](#)).

There are only a few publications that document BSW. [Ozhigin et al. \(2000\)](#) uses hydrographic profiles to characterise the "doming" pycnocline of BSW but variability at the Kola Section may be more representative of the unmodified AW rather than BSW ([Boitsov et al., 2012](#)). [Årthun et al. \(2011\)](#) uses 60 years of model output to indentify that some BSW forms over shallow banks and its transport is correlated with surface heat flux. [Årthun et al. \(2011\)](#) is limited by its focus primarily on the banks and its use of an unusual water mass definition only accounting for the densest part of the water mass, referred to as Cold Deep Water. BSW volume variability is expected to be closely tied to sea ice melt but these conclusions come for a 30 year model run with unrealistic temperature and salinity variability ([Oziel et al., 2016](#)). This shows more work is required to understand the location of BSW in the Barents Sea, how it varies seasonally and interannually.

1.2.3 Atmosphere

In the North Atlantic and Arctic the main atmospheric wind patterns are organised by the NAO and Arctic Oscillation (AO) sea level pressure (SLP) modes. NAO is the first mode of SLP variability in the North Atlantic and is defined by the pressure difference between the Azores

and Iceland (van Loon and Rogers, 1978). The AO is the leading mode of SLP in the Arctic but is highly correlated with NAO (Ambaum et al., 2001). The NAO affects the strength of the southwesterly winds in the Norwegian Sea and cyclone activity in the Barents Sea (Sorteberg and Kvingedal, 2006). As previously mentioned, NAO has been suggested as the cause of temperature and salinity variability at the BSO by modulating the width and strength of the Norwegian Atlantic Current (Ingvaldsen, 2005). The 9-10 year time scale in Barents Sea sea ice has been identified as closely related to NAO between 1900 and 1998 (Venegas and Mysak, 2000). This could have been caused by cyclone activity that was also linked to sea ice extent (Sorteberg and Kvingedal, 2006; Herbaut et al., 2015). These correlations with the NAO index were present but have broken down since around 1990-2000 as AW temperature continued to increase (and sea ice decline) regardless of a change in NAO index (Smedsrud et al., 2013). This suggests AW has taken over as the main forcing factor on sea ice extent. Herbaut et al. (2015) identified significant differences in the variability and mean sea ice concentration between 1979-2004 and 2005-2012. These differences also meant changes in the response of the sea ice to SLP after 2004 (Herbaut et al., 2015). This is an important distinction to make given it suggests the ocean variability is sometimes independent from large scale atmospheric variability.

The evidence suggests the NAO does not exert the dominant variability on the Barents Sea after ~ 2000 . At the daily time-scale, the variability in transport of AW into the Barents Sea has been found to be caused by the geostrophic response to the sea surface height gradient induced by local winds across the BSO (Ingvaldsen et al., 2004a; Skagseth et al., 2011; Smedsrud et al., 2013). At the interannual to multi-decadal timescale, model results suggest transport through the Barents Sea is mostly affected by the density of BSW leaving through the BSX but also to a lesser extent by the surface heat flux in the Barents Sea and the BSO to BSX sea surface height gradient (Smedsrud et al., 2013; Årthun et al., 2011). This has yet to be shown in observations.

Analysis of heat flux between the ocean and atmosphere shows strong seasonality. During spring and summer, the increase in short wave solar radiation results in net gain of heat by the ocean, warming the upper ocean mixed layer (Smedsrud et al., 2010). The input of heat at the surface stratifies the Barents Sea between April and October (Loeng, 1991). In autumn, the short wave radiation reduces, as do daylight hours. This means that net heat is lost from the ocean, and given that heat is also imported from AW, more heat is lost to the atmosphere during winter than is gained during summer (Smedsrud et al., 2010, 2013). The net heat loss means interannual variability in ocean to atmosphere heat flux is correlated with heat transport through the BSO (Sandø et al., 2010). The strong seasonal changes in heat flux is consistent with seasonal heat content variability, found in the first empirical mode of heat content for the Arctic Ocean (Lique and Steele, 2013). Surface air temperature (SAT) follows similar seasonal variability indicating the Barents Sea's importance in the Arctic Ocean atmospheric interactions (Jakowczyk and Stramska, 2014).

1.2.4 Arctic Ocean and Norwegian Sea

The ocean boundaries of the Barents Sea are passages to the Nordic Seas and the Arctic Ocean (Figure 1.1). The main transport of AW into the Barents Sea is along the Norwegian Atlantic Slope Current which splits into three branches (Figure 1.3). These branches enter the Lofoten Basin in the Norwegian Sea, the Barents Sea and the West Spitsbergen Current which passes through Fram Strait. Variability in the volume transport of the branches is dependant on sea surface height induced by SLP (Chafik et al., 2015; Muilwijk et al., 2018). The transport going through the Barents Sea counterbalances the transport in the West Spitsbergen Current suggesting the BSO transport has a partial dependence on remote processes (Lien et al., 2013). These transport paths are sensitive to storm tracks directing flow along one route or the other (Lien et al., 2013).

The temperature and salinity properties of AW in the Norwegian Atlantic Slope Current between the northern North Sea and the Barents Sea are affected by surface fluxes, and mixing with fresher neighbouring ArW and Coastal Current water (Yashayaev and Seidov, 2015). Yashayaev and Seidov (2015) also suggests the AW properties in the Norwegian Sea have variability

that lags NAO and AMO. The temperature anomalies are correlated between the West Spitsbergen Current and the Norwegian Atlantic Slope Current, with the addition of a 7 month lag for recirculation of AW in the western Barents Sea (Skagseth, 2008). This excursion into the western Barents Sea imprints temperature anomalies from winter surface heat flux onto water that becomes the West Spitsbergen Current (Schlichtholz and Houssais, 2011).

The West Spitsbergen Current has relevance to the Barents Sea because like AW passing through the Barents Sea, it subducts beneath ArW. Some of the AW has been suggested to re-enter the Barents Sea from the north forming a layer beneath ArW in the northwestern Barents Sea but the properties are similar to BSW so the source should not be decided from hydrographic profiles alone (Lind and Ingvaldsen, 2012). Fram Strait AW is less dense, warmer and saltier than BSW but rejoins BSW around St. Anna Trough (Figure 1.1).

When BSW exits St. Anna Trough into the Arctic it sinks below the Fram Strait AW branch to form a salinity minimum, which mixes with the warmer Fram Strait AW above as it circulates around the Arctic Basin (Rudels et al., 2000; Dmitrenko et al., 2015). In this way the Barents Sea branch produces most of the intermediate (50 – 80 %) water and contributes to deep water in the Arctic Ocean (Schauer et al., 1997; Maslowski et al., 2004). The transport of AW along the Eurasian Basin slope has shown warming, salinification and erosion of the ArW layer above referred to as "atlantification" (Polyakov et al., 2017) (Figure 1.8). These water masses ultimately exit through Fram Strait and leave the Greenland Sea through the Denmark Strait contributing to Atlantic Meridional Ocean Circulation (AMOC) (Karcher et al., 2011; Lique et al., 2010) (Figure 1.1 and 1.3)).

1.3 Motivation

1.3.1 Remote Influence of the Barents Sea Processes

The variability in the Barents Sea has remote impacts. AW brings relatively warm water to high latitudes, an important factor in making the net annual heat lost in this region greater than annual solar heat gained (Figure 1.3). Sea water brings heat to this region because the density of water normalised by the ocean mixed layer thickness and heat capacity ($3992 \text{ J k}^{-1} \text{ K}^{-1}$) is much greater than the air density normalised by the atmospheric boundary layer and smaller heat capacity of air ($1005 \text{ J k}^{-1} \text{ K}^{-1}$). This means that during winter, there is a strong temperature gradient between the ocean and the atmosphere. The net heat loss from the ocean has two direct results, ramifications of these can be addressed separately and give motivation for studying this region :

1. Air in the relatively cool atmosphere is warmed.
2. The water transported to the Barents Sea loses heat, and consequently buoyancy.

First, the ocean to atmosphere heat flux is correlated with sea ice variability (Årthun et al., 2012; Screen and Simmonds, 2010b). Anomalies in ocean to atmosphere heat flux during autumn and winter cause a sequence of disturbances that propagate upwards through the layers of the atmosphere into the stratosphere (Schlichtholz, 2014; Yang et al., 2016; Petoukhov and Semenov, 2010). The exact physical processes and complex atmospheric dynamics involved are under debate among atmospheric scientists (Yang et al., 2016; Vihma, 2014). However, the warm water and low sea ice anomalies in the Barents Sea are coincident with cold surface air temperature anomalies across Europe and Asia (Blackport et al., 2019; Hoshi et al., 2019; Mori et al., 2014) (Figure 1.7). It has recently been suggested that anomalies in turbulent heat flux in the Barents Sea are more causative of the cold Eurasian winters than the sea ice itself (Blackport et al., 2019). The cold surface air temperature patterns in Asia are similar to the negative phase of the large scale weather patterns, NAO and AO (Vihma, 2014; Yang et al., 2016). Positive NAO is specifically linked to extreme wind events in the North Atlantic and north-west Europe (Yiou and Nogaj, 2004; Donat et al., 2010) suggesting these are less common with less sea ice cover. The autumn sea ice concentration anomalies show correlation with regional winter precipitation patterns over Europe and Asia with strengthening correlation since 1980 (Li and Wang, 2013). Anomalously

low annual sea ice extent across the whole Arctic over recent years (Figure 1.2) has also been suggested as the cause of increased summer precipitation across northern Europe (Screen and Simmonds, 2010a). In addition, longer term changes in the summer precipitation climate could cause geopolitical tension in Asia due to water supply and usage (Bernauer and Siegfried, 2012; Zakhirova, 2013; White et al., 2014). These low sea ice years in the Barents Sea additionally push cyclonic storm tracks southward out of the Arctic Basin and further south over the Siberian coast (Inoue et al., 2012). Following the dramatic variability that may originate in the Barents Sea, this sea could be thought of as analogous to the Central Pacific for El Niño. In the case of El Niño, interannual variability causes warm sea surface temperature anomalies to spread across the Central Pacific causing atmospheric convection and anomalous weather patterns over the surrounding continents (Trenberth, 1997). Understanding the intensity and frequency of these anomalous weather events is important to improve prediction and mitigation against disruption caused by them. While the majority of the literature address this problem from an atmospheric perspective the work completed in this thesis will add analysis and discussion to this problem from an ocean perspective, a component of the dynamic system that should be better understood.

Second, the ocean to atmosphere heat flux from warm, salty AW transported into the Barents Sea means it becomes more dense than the upstream AW and the relatively fresh ArW (Table 1.1) present in the Arctic Ocean (Midttun, 1985; Årthun et al., 2011). This makes the Barents Sea a region where isopycnals are ventilated and convection is likely to occur (Carmack et al., 1997). When BSW leaves the Barents Sea it sits below the fresher ArW in the Arctic Ocean, isolating it from the atmosphere (Rudels et al., 2000) (Figure 1.8).

The ventilation of isopycnals and subsequent isolation of this water mass from the atmosphere means the Barents Sea has potential to absorb and sequester carbon dioxide (Terhaar et al., 2018). Barents Sea AW has been observed and simulated to be absorbing more carbon dioxide from the atmosphere than other Arctic regions (Kaltin et al., 2002; Yasunaka et al., 2016; Terhaar et al., 2018). While the carbon dioxide absorbed here is substantial, the quantity of carbon that is advected through the Barents Sea in AW is 27 times greater (Terhaar et al., 2018; Smedsrud et al., 2013). The formation of dense BSW in the Barents Sea pushes this carbon carrying water into the Arctic Basin. Given the quantity of carbon transported through the Barents Sea, variability in the transport could affect the rate of carbon dioxide sequestering. Therefore, improving our understanding of this system could help with future climate predictions. Transport in the Barents Sea will be discussed in Chapter 4.

Once BSW enters the Arctic Basin it settles below another branch of AW entering through Fram Strait (Rudels et al., 2000). These two branches make up Arctic Intermediate Water (AIW) (Figure 1.8). AIW is important for its storage of heat below the fresher ArW layer. Mixing and heat flux between these water masses has potential to change sea ice melt rates (Polyakov et al., 2017; Rippeth et al., 2015). After circulating around the Arctic Basin, AIW exits through Fram Strait and traverses the Greenland Sea before spilling over the Denmark Strait overflow to contribute to the North Atlantic Deep Water branch of AMOC (Figure 1.3). This means the variability in BSW properties are propagated along this transport route (Karcher et al., 2011; Lique et al., 2010). AMOC is an important part of the Earth's climate system and is dependant on the deep water formation regions to sustain the circulation. Long term (> 20 years) increases in the Arctic Ocean buoyancy through heat or freshwater fluxes could reduce AMOC transport by slowing the formation of deep water (Sévellec et al., 2017). This suggests a need to monitor and understand this transport route. How BSW density varies is a question that will be picked up in each of the results chapters of this thesis.

1.3.2 Local Influence of Barents Sea Processes

Studying the Barents Sea has importance for local economic activities within the Barents Sea as well as in the remote context. Sea ice extent prediction is a challenge for industries that operate in the Barents Sea (Eicken, 2013). The reduction in summer sea ice over the last few decades has opened up new possibilities for commercial shipping routes (Figure 1.2). These shipping routes are experiencing greater risk from any remaining summer sea ice that is becoming more mobile in

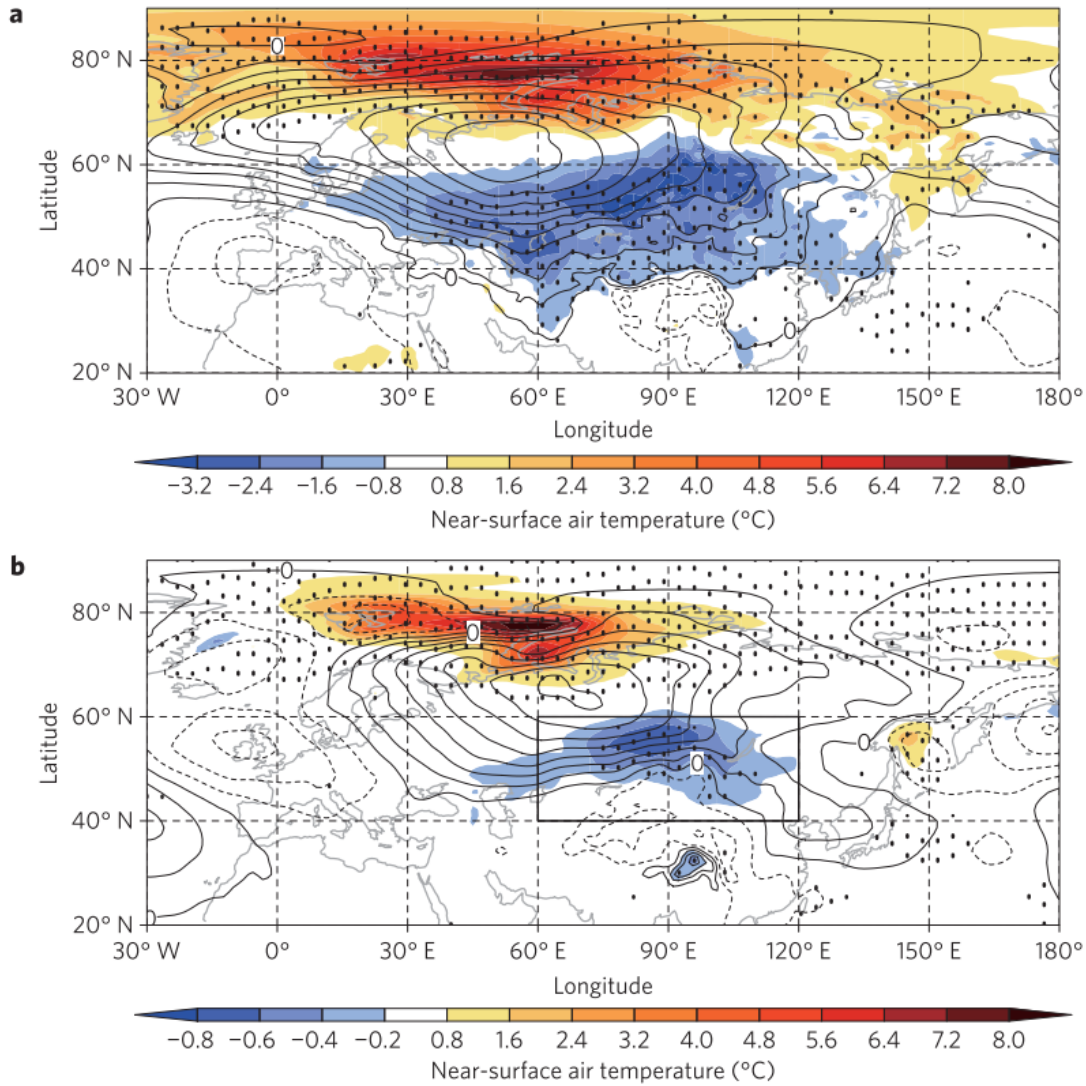


FIGURE 1.7 – Observed and simulated change in winter SAT and atmospheric circulation associated with sea-ice retreat in the Barents-Kara region. (a,b) Differences of composite fields between the low- and high-ice years (that is, the former minus the latter) for SAT (colour) and SLP (contours) in DJF, (a) taken from ERA-Interim and (b) the 100-member ensembles of the Low Sea Ice and High Sea Ice experiments. Contour interval is 0.8 hPa in a and 0.2 hPa in b, with negative contours dashed. Stippling indicates regions of significant difference exceeding 95% statistical confidence. Figure from [Mori et al. \(2014\)](#).

storms ([Simmonds and Keay, 2009](#)). The sea ice can make resource exploration more hazardous at best and economically inviable at worst. Improving both summer and winter predictions of sea ice extent in the Barents Sea would improve the safety and reduce the cost to industries operating in this sector ([Onarheim et al., 2015](#)). Correlation between sea ice extent and other properties in the Barents Sea will be looked at in Chapters 2 and 4.

Polar lows and cyclones are localised extreme wind events formed by a strong temperature gradient between cool air advected over relatively warm SST ([Stoll et al., 2018](#)). Polar lows often form in the Norwegian Sea and traverse into the Barents Sea. Following recent changes in sea ice, the formation region is expanding and polar lows are becoming more common in the Barents Sea ([Rojo et al., 2015](#); [Sorteberg and Kvingedal, 2006](#)) (Figure 1.9). There is conflicting evidence about whether this trend will continue under future climate projections from Intergovernmental Panel of Climate Change ([Long and Perrie, 2017](#); [Zahn and Von Storch, 2010](#)). These extreme

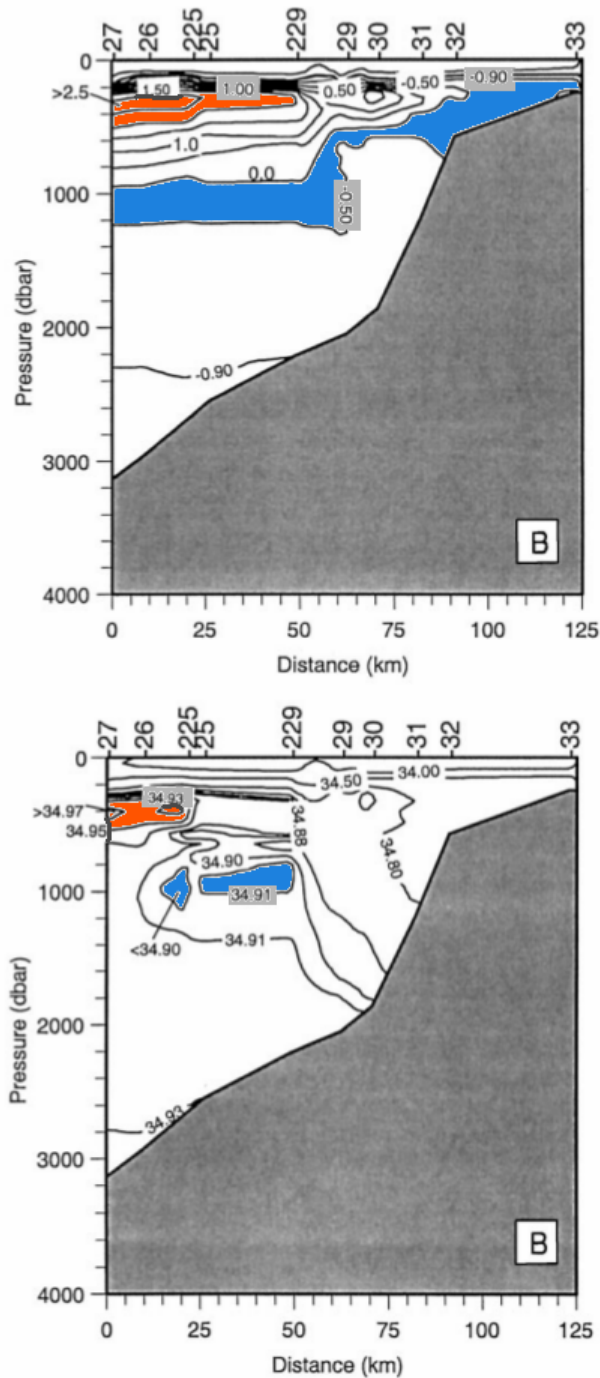


FIGURE 1.8 – Potential temperature and salinity distributions from a hydrographic profile section north of the Kara Sea on the Eurasian Slope. The orange areas mark the temperature and salinity maximum associated with Fram Strait Atlantic Water. The blue area mark the core temperature and salinity associated with the Barents Sea Water branch. Figure from [Rudels et al. \(2000\)](#).

wind events are dangerous for ships and planes ([Samuelsen et al., 2015](#)). Improving our understanding of the sea surface temperature variability in the Barents Sea could improve polar low forecasting. While this topic will not be addressed directly in this thesis, analysis of SST in Chapter 2 and heat flux in Chapters 3 and 4 could be valuable to this field.

The waters of the Barents Sea are very productive, making up 36 – 47 % of total primary productivity in the Arctic ([Arrigo and Van Dijken, 2011](#); [Ardyna et al., 2013](#); [Oziel et al., 2017](#)). In general, Arctic primary productivity has been increasing as sea ice area declines and the Barents Sea is not an exception ([Arrigo and Van Dijken, 2011](#)) (Figure 1.10). This is caused by

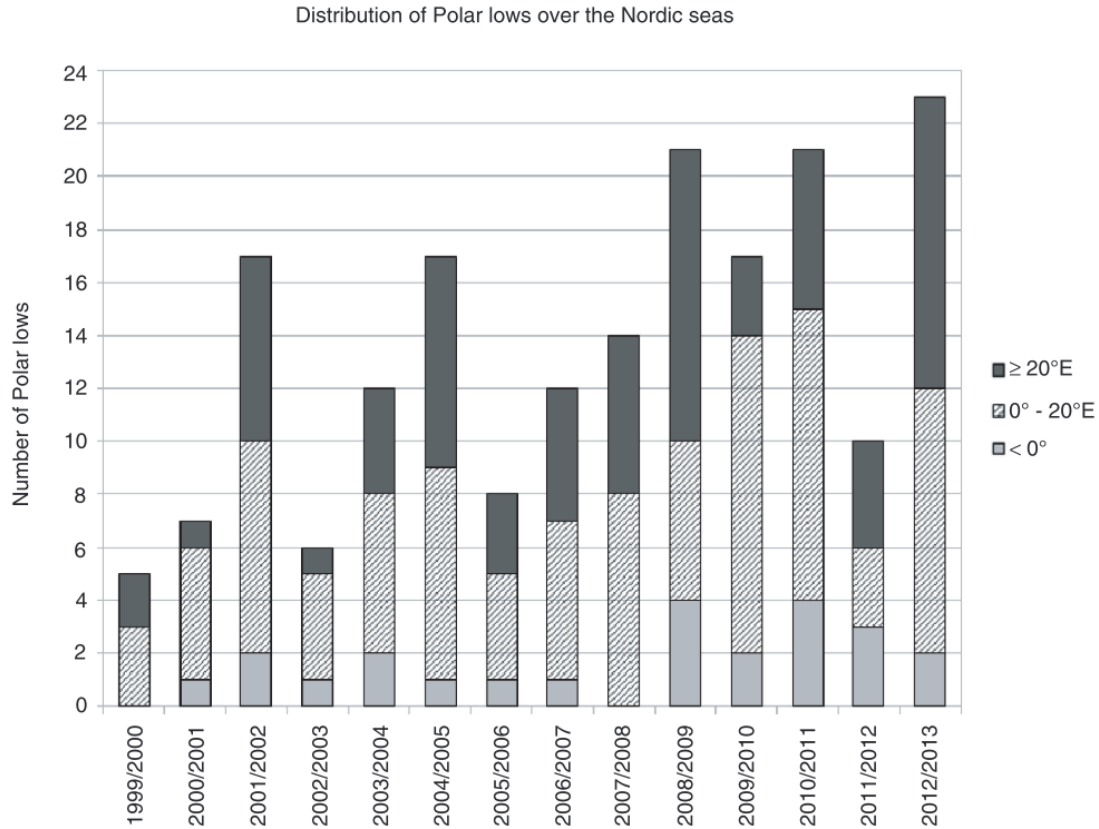


FIGURE 1.9 – Interannual variability of Polar Lows over the Nordic Seas from winter 1999/2000 to winter 2012/2013. Polar lows that form over the Greenland Sea (west of 0 °) are represented in light grey, those that form over the Norwegian Sea (between 0 ° and 20 °E) are represented in striped black and white and those that form over the Barents Sea (east of 20 °E) are represented in dark grey. Figure from Rojo et al. (2015).

the increase in light available to phytoplankton. Within the Barents Sea productivity increases seasonally when stratification stabilises the water column (Strass and Nöthig, 1996). Overall, the Barents Sea has peak chlorophyll-a in May and BSW has the largest seasonal peak in chlorophyll-a of the Barents Sea water masses (Oziel et al., 2017) (Figure 1.10). Productivity tends to be sustained around fronts in this region, where nutrients are mixed across vertical and horizontal density boundaries (Våge et al., 2014; Oziel et al., 2017). The importance of this productivity comes from the fish stocks it supports (Svendsen et al., 2007). The western Barents Sea has the optimum combination of primary productivity and warmer water that mean it accounts for 50 – 80 % of the total annual fish biomass in the combined Barents Sea and northern Norwegian Sea (Eriksen et al., 2011). At interannual time scales, variability in fish stocks can be attributed to variability in AW temperature due to the changes in productivity and sea ice cover it causes (Årthun et al., 2018). A main theme throughout this thesis will cover variability in BSW and Barents Sea frontal regions that are important for productivity.

1.4 Aims and Objectives

The motivations for this thesis are :

1. The Barents Sea is changing rapidly.
2. The dynamics of stratification is complex with competing temperature and salinity factors.
3. The sea ice extent and heat flux variability are associated with the intensity and frequency of northern hemisphere weather events.

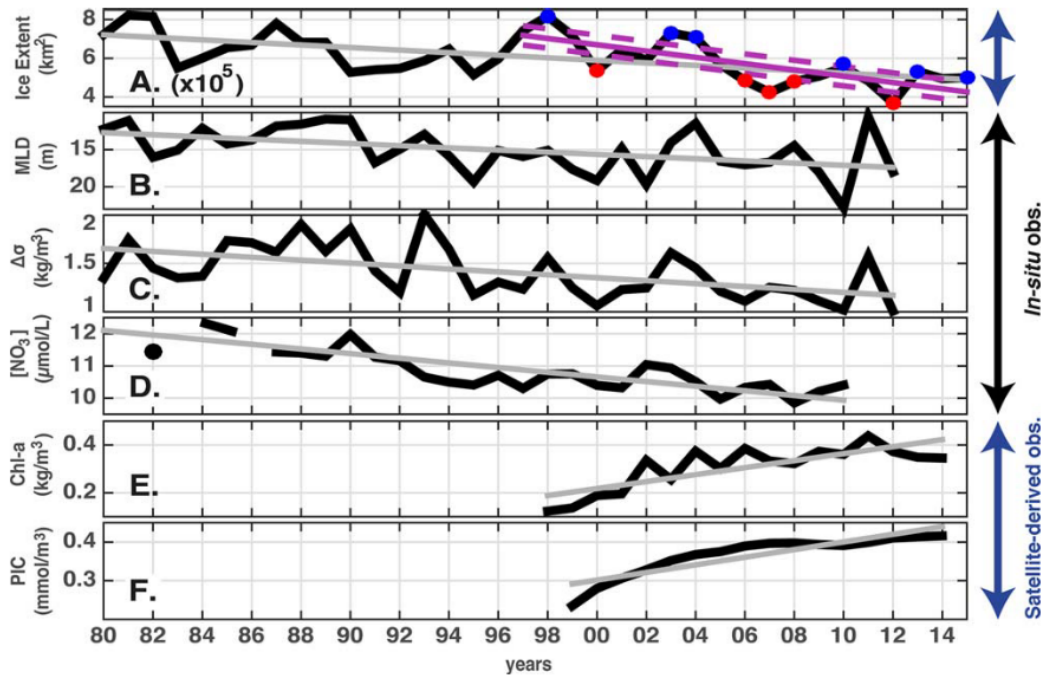


FIGURE 1.10 – Time series of (a) winter maximal Sea Ice extent, (b) summer Mixed Layer Depth (MLD), (c) stratification, $\Delta\sigma$ ($\rho_0 - \rho_{100m}$), (d) winter (January-March) nitrate concentration at the BSO section integrated over the depth interval 0-200 m, (e) annual mean satellite Chl a, and (f) annual mean satellite Particulate Inorganic Carbon (PIC). Data in (e) and (f) are normalized by the amount of available pixels. Lines denote trend over their temporal domain. Magenta-dashed lines correspond to a deviation of $\pm 50,000 \text{ km}^2$ from the trend line shown in magenta. PIC value in 1998 is missing. Nitrate values for 1980, 1983, and 1986 are missing. Figure from [Oziel et al. \(2017\)](#).

4. The variability in sea ice is linked to AW temperature variability.
5. The Barents Sea acts as a precursor for Arctic climate change.

Throughout this thesis the Barents Sea will be the focus under the expectation that conclusions draw from the physics in this region may be applicable in other regions of the Arctic. The main theme underpinning this thesis is BSW variability. The overall question of this study is : how does the seasonal sea ice impact ocean stratification and mean flow ? This will be addressed with the specific objectives :

- To investigate the variability of SST in order to characterise the PF's location in the eastern Barents Sea, determine how this compares to the seasonal sea ice edge and what the implications for BSW formation are given the documented sea ice loss and atlantification of the Barents Sea ?
- How can satellite data can be used to obtain information on the heat and freshwater content variations within the water column and in particular to measure BSW variability.
- What causes seasonal to interannual variability in AW and BSW volume and properties in the central Barents Sea ? Following the regime change in 2005, can the ocean dynamics help predict if a similar or opposing regime change could happen again ?

In order to answer the overall question and address the aims, there are several data types that will be used as the tools in this pursuit.

The Barents Sea is a location that has received regular ship based surveys that make a catalogue of profiles that cover the 1920 to present ([Levitus et al., 2009](#)). Although recent years have seen developments in automation of hydrographic profiling such as Argo floats, the Barents Sea is too shallow and seasonally ice covered to make deployment here possible. The hydrographic profiles are collected into datasets such as EN4 ([Gouretski and Reseghetti, 2010](#)) and MIMOC

(Schmidtke et al., 2013). There are also long term observation sections, with moorings in the case of the BSO and regular ship measurements in the case of the Kola Section in the central Barents Sea.

The satellite observation time period covers 1979 to present. Satellites have the advantage over *in situ* observations in being able to make repeat measurements over global spatial scales. The satellite data still needs *in situ* observations to corroborate findings. Satellite data types such as OSTIA SST (Donlon et al., 2012) are only able to measure the ocean surface so additional *in situ* measurements are often needed to build a 3-dimensional picture. Satellite parameters such as sea surface height and ocean bottom pressure can give bulk properties adding to the repertoire of satellite data (Armitage et al., 2016; Chambers and Bonin, 2012).

A regional ocean model of the North Atlantic and Arctic Ocean has been developed with regional NEMO (Dupont et al., 2015) coupled to the LIM3 sea ice model (Vancoppenolle et al., 2009).

1.4.1 Thesis Structure

This thesis is organised as a series of stand alone articles that have either been published, under peer review or in preparation for publication. This means instead of having methods and results chapters, Chapters 2, 3 and 4 are self contained publication manuscripts each with respective introduction, methods, results, discussion and conclusion. References are in the Bibliography after the conclusions in Chapter 5 and 6. Supporting information is included at the back of the thesis. Chapter 2 identifies the location of the Barents Sea Polar Front using observation data and investigates how trends in temperature over the satellite time period have changed the ocean climate in the Barents Sea. Chapter 3 utilises a combination of satellite and *in situ* data to derive new satellite based estimates of BSW heat and freshwater content. Chapter 4 uses model output to return to the changes that took place in the Barents Sea identified in Chapter 2 observations. This chapter uses the synoptic nature of the high resolution model to determine interannual variability and sequencing of events around the mid-2000s regime change. Chapter 5 provides a summary and synthesis of the complete work. Chapter 6 is a french translation of Chapter 5.

Chapitre 2

Observed atlantification of the Barents Sea causes the Polar Front to limit the expansion of winter sea ice

This is a reproduction of the published paper : B. I. Barton, Y.-D. Lenn, and C. Lique. Observed atlantification of the Barents Sea Polar Front limits the expansion of winter sea ice. *Journal of Physical Oceanography*, 48 :1849–1866, 2018. ISSN 0022-3670. doi : 10.1175/JPO-D-18-0003.1. URL <http://journals.ametsoc.org/doi/10.1175/JPO-D-18-0003.1>.

2.1 Introduction

The Arctic has been predicted to be sea-ice-free in summer by the middle of the twenty-first century (Wang and Overland, 2012; Snape, 2013; Notz and Stroeve, 2016). This follows an Arctic-wide decline in sea ice extent over recent decades (Screen and Simmonds, 2010a). The Barents Sea alone has seen a 50% reduction in annual sea ice area between 1998 and 2008 (Årthun et al., 2012), associated with a strong sea ice decline in all seasons including winter (Onarheim and Årthun, 2017). Seasonal sea ice extent variations are very predictable in the Barents Sea compared with other parts of the Arctic (Sigmond et al., 2016). For instance, Day et al. (2014) found significant correlations between Arctic sea ice extent in May, and Barents Sea sea surface temperature (SST) for the same month, as well as with SST in the preceding December. The variability of the Barents Sea ice edge location has also been associated with atmospheric circulation (Sorteberg and Kvingedal, 2006), and ice exported from the Arctic to the Barents Sea due to local winds (Koenigk et al., 2009; Kwok, 2009). On longer time scales, the reduction in annual and winter Barents Sea sea ice area is thought to be driven by an increase in the heat transport into the Barents Sea due to the combined increase in advection and temperature of Atlantic Water (AW) (Årthun et al., 2012; Onarheim et al., 2015). AW temperature and salinity in the Barents Sea are also varying on multidecadal timescales (Levitus et al., 2009; Smedsrud et al., 2013), making it challenging to distinguish between long term trend and natural variability.

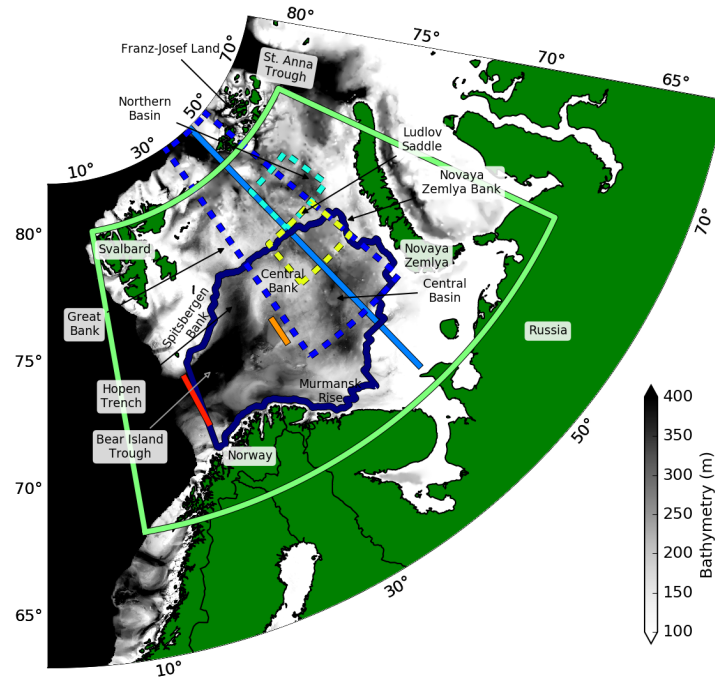


FIGURE 2.1 – Bathymetry of the Barents Sea. The different lines and box indicate the area used for EOF analysis of SST (green box), the region used for Hovmoller analysis (blue-dashed box), the cross-front transect (light-blue line), the area selected for calculating the contribution of sea ice to AW/BSW (dark-blue box), the area selected for 100 – 300 m BSW properties from EN4 data and 0 – 100 m ArW properties from EN4 data (cyan-dashed box), the area selected for 0 – 100 m surface BSW properties from EN4 data south of the PF (yellow-dashed line), the the Kola section (orange line) and the Fugløy–Bear Island section (red line).

Along with Fram Strait, the Barents Sea Opening (BSO) is a gateway for the warm and salty

AW (defined in Table 1.1) entering the Arctic Ocean and its marginal seas (Figure 2.1). The branch of AW entering through the BSO transits the Barents Sea, where it is modified en route, forming Barents Sea Water (BSW, Table 1.1) (Schauer et al., 2002; Harris et al., 1998). This transformation into BSW is driven mainly by surface interactions with the atmosphere resulting in winter convection and entrainment of freshwater. Heat is lost from the ocean through turbulent heat flux and longwave radiation (Long and Perrie, 2017), while freshwater input mostly comes from seasonal sea ice import and rivers (Ellingsen et al., 2009). Thus the length and location of the pathway along which AW flows determines to what extent its properties are modified by surface fluxes, sea ice and rivers before it enters the Arctic Basin. The Barents Sea bathymetry is known to strongly influence the path of AW inflow (Loeng, 1991) (Figure 2.1). Part of the AW inflow crosses Murmansk Rise, south of Central Bank, into the Central Basin (Skagseth, 2008; Ingvaldsen, 2005). The Central Basin acts as a reservoir for AW until it loses enough buoyancy to propagate northwards below ArW as BSW. As a result, the water column is stratified in the northern Barents Sea, with the upper 100 m occupied by relatively fresh and cold Arctic Water (ArW, Table 1.1) and the lower layer occupied by BSW (Harris et al., 1998; Lind and Ingvaldsen, 2012).

In situ observations in the western Barents Sea have revealed that the surface expression of the front separating AW from ArW follows isobaths in the range 150 - 275 m (Gawarkiewicz and Plueddemann, 1995; Harris et al., 1998; Våge et al., 2014; Fer and Drinkwater, 2014). In the eastern Barents Sea, the northern front (referred to as the Polar Front - PF hereafter) is defined as the location where BSW meets ArW but its geographic position is poorly defined (Oziel et al., 2016). The PF is a water mass boundary and therefore should have an SST signature. This PF should be distinguished from another nearby SST front (hereafter thermal-surface front) that is also expected to be present in the surface layer of the northern Barents Sea following the sea ice edge, due to the transition from freezing-point water to ice-free water. In the range of temperatures and salinities of BSW and ArW, salinity and temperature tend to contribute equally to the determination of density (Parsons et al., 1996; Våge et al., 2014). Thus, both surface temperature and surface salinity contribute to the PF's surface density gradient, suggesting that the variability of the PF position can be influenced by other processes than just the position of the sea ice edge.

BSW exits the Barents Sea, entering the Arctic Ocean mainly through St. Anna Trough (Rudels et al., 2000; Smedsrud et al., 2013). In the Arctic Ocean, BSW is entrained into Arctic Intermediate Water (AIW), accounting for 50 - 80% of the volume of AIW (Schauer et al., 1997; Maslowski et al., 2004). AIW is ultimately exported to the North Atlantic through Fram Strait and in turn contributes to the deeper branch of the Atlantic Meridional Overturning Circulation (AMOC) (Aagaard et al., 1985; Fahrbach et al., 2001). There is some debate in the literature about the extent to which BSW properties at the exit of the Barents Sea are preserved into the Arctic Ocean and beyond. Observations have revealed that some mixing of BSW occurs on continental slopes and within the Arctic Ocean (Shapiro, 2003; Rudels et al., 2015) but model results of Lique et al. (2010) show modifications to BSW properties within the Arctic Ocean are small compared to the modification within the Barents Sea. In either case, the properties with which BSW exits the Barents Sea are important as they pre-condition it for the target depth at which it may settle and mix with ambient water masses within the Arctic Basin. Anomalies in BSW density have been traced to Denmark Strait suggesting far-reaching impacts from processes occurring in the Barents Sea (Karcher et al., 2011).

It has been hypothesised by Aagaard and Woodgate (2001) that a prolonged reduction in the fresh, melt water input from seasonal sea ice into BSW could cause a modification of the BSW properties, and in turn induce a warming and salinification of AIW. This hypothesis overlooks the role the PF could play in determining whether the meltwater is entrained into BSW or ArW and discounts the influence of changes in other water masses in the Barents Sea. Indeed, both the transport and the temperature of AW circulating in the Barents Sea have increased in recent decades (Årthun et al., 2012), resulting in a reduction in winter sea ice area through a decrease in wind-driven sea ice advection and delayed winter refreezing (Lien et al., 2017). Thus, winter

sea ice extent trends are consistent with the emerging evidence of ongoing atlantification (i.e. the increased influence of AW resulting in a warming and salinification) of the Barents Sea (Reigstad et al., 2002; Oziel et al., 2017) and Arctic Ocean (Polyakov et al., 2017). This makes it important to quantify the role that Barents Sea ice trends play on BSW properties.

The goal of this study is to investigate the variability of SST in order to characterise the PF's location in the eastern Barents Sea, determine how this compares to the seasonal sea ice edge and what the implications for BSW formation are given the documented sea ice loss and atlantification of the Barents Sea? To that aim, we use a combination of the new high-resolution, 32-year OSTIA SST dataset, satellite observations of sea ice concentration and 3D optimally interpolated temperature and salinity products.

The methods and tools are presented in Section 2.2. In order to identify forcings on the formation of BSW, in Section 2.3, the mechanisms that cause variability in SST on seasonal and to multidecadal time-scales in the Barents Sea are explored. In Section 2.4, SST is used to pinpoint the surface expression of the PF, and determine whether the winter sea ice edge has become bound by it. In Section 2.5, the results of Section 2.3 and Section 2.4 are brought together and the consequences of a regime shift for BSW properties are discussed. Conclusions are presented in Section 2.6.

2.2 Data and Methods

2.2.1 Datasets

This study makes use of satellite SST and sea ice concentration data from the OSTIA project spanning January 1985 to December 2016 (Donlon et al. (2012); downloaded from marine.copernicus.eu portal). This dataset is optimally interpolated from multiple satellite sensors together with *in situ* observations onto a 0.05° grid (1.5×5.6 km for Barents Sea) at a daily frequency. The feature resolution is 10 km and the accuracy of the daily data is ~ 0.57 K (Donlon et al., 2012). At the current spatial and temporal resolution, the satellite SST data used in this study can not yet resolve mesoscale variability (with a characteristic scale of only a few kilometers) in the Barents Sea. Sea ice extent in the Barents Sea is computed from the OSTIA sea ice concentration. The sea ice edge is defined as the 15% contour the sea ice concentration.

Bathymetry is taken from the GEBCO 2014 30 arcsecond resolution dataset (Weatherall et al. (2015); GEBCO_2014 Grid, version 20150318, www.gebco.net). In the Barents Sea, it corresponds to a resolution of 0.2 km in longitude and 0.9 km in latitude. We also use fields of surface air temperature (SAT; corresponding to temperature at 2 m above surface) and sea level pressure (SLP) from the ECMWF ERA-Interim reanalysis (Berrisford et al. (2011); www.ecmwf.int). This dataset is provided on a 0.75° grid (84×16 km for Barents Sea) with 3-hourly temporal resolution, averaged into monthly means.

Observations from the Fugløy-Bear Island section along 20.0° E in the BSO (red line, Figure 2.1) are used to characterize the variations of the AW inflow temperature and salinity (Larsen et al., 2016). This dataset is available through the ICES portal (ocean.ices.dk/iroc) and corresponds to hydrographic profiles, collected six times a year, used for the period January 1985 to October 2015. The time series presented here is averaged over the 50 - 200 m depth range and between 71.5° N and 73.5° N (Ingvaldsen et al., 2003), and is thus representative of the subsurface temperature and salinity variability. We also use observations from the Kola section (available through www.pinro.ru), extending from 73.0° N to 74.0° N along 33.5° E (orange line, Figure 2.1), as a proxy for the AW temperature in the central Barents Sea. Along the section, Conductivity Temperature Depth (CTD) profiles have been collected between 7 to 9 times per year and we use the subset from January 1985 to December 2015 (Bochkov, 1982; Ingvaldsen et al., 2003). We consider again the depth range between 50 and 200 m (i.e the sub-surface), which is below the depth of the summer mixed layer and is the depth range over which the core of AW enters the Barents Sea (Ingvaldsen, 2005).

In order to examine the variability and long-term trends over the wider region than just these two sections, temperature and salinity fields from the EN4 dataset are analysed (EN4.2.0,

www.metoffice.gov.uk/hadobs/en4). EN4 comprises *in situ* ship CTD profile data and Argo float data optimal-interpolated on a 1° , monthly z-grid with 42 levels (Gouretski and Reseghetti, 2010). Data used in this analysis are from the January 1985 to December 2016 period. Between 1985 and 2015, there is a minimum of 2 profiles of temperature and salinity per year in the northeastern Barents Sea. It should be noted that there is a summer bias in this dataset based on when most of ship based profiles were collected. To accommodate the variability in profile sampling the uncertainty values provided in EN4 are considered throughout this study (Good et al., 2013).

Additional temperature and salinity fields are retrieved from the MIMOC ocean climatology project (www.pmel.noaa.gov/mimoc), which optimally interpolates *in situ* ship CTD profiles and Argo float data onto a 0.5° σ -grid followed by an 81 level z-grid (Schmidt et al., 2013). The monthly climatology is weighted to be representative of 2007 to 2011. MIMOC data was included in this study as its higher spatial resolution allows a better description of the 3D structure of the front than EN4 data, although it does not provide information on the interannual variations of the fields.

2.2.2 Methods

The Barents Sea SST seasonal climatology is calculated from the OSTIA data. To resolve the PF, the magnitude of the gradient in SST for both the latitude and longitude directions are calculated using the equation : $|\nabla T_{(x,y)}| = \sqrt{(\partial T/\partial x)^2 + (\partial T/\partial y)^2}$.

In order to characterise the temporal and spatial variability in SST over the Barents Sea, empirical orthogonal functions (EOF) are calculated using the singular value decomposition (SVD) method (Thomson and Emery, 2014). EOF analysis extracts the main mode of SST interannual variability, providing us with a spatial pattern and an associated time-varying index referred to as the principal component (PC). The area selected for EOF analysis covers the Barents Sea (10° E – 65° E and 68° N – 80° N, see green box, Figure 2.1). Prior to the EOF decomposition several steps were taken. These are : (1) data points within 28 km (5 grid cells) of land were removed as well as the Kara Sea and any isolated inlets with restricted connectivity to the Barents Sea that would be unrepresentative of the variability in the Barents Sea; (2) the seasonal cycle was then removed from the SST monthly means in each grid cell by applying a 12-month running mean to the data; (3) the mean SST at each grid cell was then removed, (4) finally SST in each grid cell was divided by its respective standard deviation. We also compute correlations between the PC and other fields which were also subject to a 12-month running mean.

A 2-tailed Welch’s t-test is used to estimate the significance of a difference between two given time periods, while a 2-tailed Student’s t-test is used for the significance of linear trends in monthly SST. For estimating the 95%-level significance of correlations, a 2-tailed Student’s t-test is used and an appropriate reduction in degrees of freedom associated with a 12-month running mean is accounted for.

In this study, the criteria used to define the different water masses mostly follows previous definitions found in the literature (e.g. Loeng (1991); Table 1.1). The main adjustment made to existing definitions is the minimum density set for the BSW definition ($\sigma > 27.85 \text{ kg m}^{-3}$); it ensures that we reject the warm and fresh surface water that is not dense enough to sink into the Arctic Ocean. Note that our results are mostly insensitive to the exact definition of the different water masses. For the EN4 and MIMOC datasets, potential density is determined using TEOS-10 (McDougall et al., 2012). Practical salinity and potential temperature are also estimated and presented throughout to allow direct comparison to results found in the literature.

In order to quantify the changes of the BSW properties over time, we estimate the mean BSW temperature and salinity from EN4 data within a domain in the north eastern Barents Sea (Northern Basin, 44° E – 54° E and 76.5° N – 78.5° N, see cyan-dashed box, Figure 2.1). We only consider the depth range 100 – 300 m, as in this region, BSW is isolated from the atmosphere by the ArW layer, inhibiting further modification before BSW reaches the Arctic Basin. ArW properties are defined in the 0 – 100 m layer within the same region from EN4. Surface BSW properties south of the PF are defined from EN4 in the Central Basin (40° E – 50° E and 74.5° N

– 76.5° N, see yellow-dashed box, Figure 2.1)

2.3 Seasonal and Interannual Variability of Sea Surface Temperature in the Barents Sea

In this section, we characterize the temporal and spatial variations of SST over the Barents Sea. SST, by which the surface expression of PF is defined in Section 2.4, is representative of air-sea interactions that are key to the formation of BSW. We first examine the seasonal cycle because this has been suggested, from model analysis, to play an important role in BSW formation (Årthun et al., 2011; Dmitrenko et al., 2014). When averaged over the Barents Sea domain (see green box in Figure 2.1), the amplitude of the SST seasonal cycle amounts to 1.69 °C, with minimum and maximum occurring in April and July, respectively. This value is large when compared to the standard deviation of the mean SST once the seasonal cycle is removed, which amounts to 0.41 °C. Clearly, SST is dominated by seasonal variability. The annual winter reduction in SST is key to the formation of BSW through heat loss and given this is an annual event suggests a link between BSW and the 1 – 2.5 year residence time of AW within the Barents Sea (Smedsrud et al., 2010; Årthun et al., 2011).

Maps of seasonal mean SST, over the period 2005 – 2016 are shown in Figure 2.2a-d. It reveals a pool of warm AW in the southwestern Barents Sea with a tongue of AW in Central Basin. This warm AW tongue is intensified in winter and spring but present throughout the year. In the southwestern Barents Sea, SST increases from 4 °C in spring to 8 °C in summer. In the remainder of the Barents Sea, the SST also increases by 4 °C between spring and summer but approaches -1.8 °C in the spring due to the presence of sea ice (Figure 2.3a-d). The sea ice edge also shows strong seasonality, retreating to the northern margins of the Barents Sea in summer, while advancing towards Central Bank from the north and the south-east in winter. As discussed later in this section, the long term trend in SST changes in 2005, posing the question of a possible change of SST seasonal cycle across the full period considered. The most striking difference between the 1985 – 2005 (Figure 2.3) and the 2005 – 2016 (Figure 2.2) time periods is the location of the sea ice edge, with appreciably larger areas of open water post-2005 in all the seasons. This is accompanied by changes in SST where the seasonal sea ice has retreated.

This seasonality is primarily driven by the seasonal cycle of the net surface heat flux with a contribution from AW heat transport (Ding et al., 2016; Smedsrud et al., 2010). In the northern Barents Sea, seasonal surface heat fluxes roughly balance over a year. In contrast there is a net heat flux from ocean to atmosphere in the southern Barents Sea, suggesting the importance of heat brought here by AW for the formation of BSW (Smedsrud et al., 2010).

To examine SST variability on interannual and longer time-scales, the seasonal cycle is first removed and EOF analysis is performed (see Section 2.2 for methodology). The trend is not removed as this could be related to multidecadal variability discussed later in this section. The first mode (EOF 1) of variability in SST explains 72.9% of the variance. As the second mode explains less than 10% of the variance, we only discuss EOF 1. The spatial pattern of EOF 1 is a positive anomaly across the full Barents Sea (Figure 2.4a). PC 1 has a periodicity of 6 to 10 years but also exhibits multidecadal variability (Figure 2.4c). PC 1 is strongly correlated with the interannual variations of SAT over the Barents Sea where SAT leads by 2 months (Figure 2.4b). Regressing PC 1 on the SAT fields reveals an area of significant positive correlation over the Arctic Ocean, eastern Arctic shelf seas and northern Russia. Lag correlations with AW temperature show AW leads SST by 2 to 4 months. PC 1 is significantly correlated with the variation of AW temperature at the Kola section ($r = 0.89$, lag = -2 months, Figure 2.4d) and the Fugløy–Bear Island section ($r = 0.80$, lag = -4 months, Figure 2.4d). PC 1 is also anti-correlated with the variations of the sea ice extent in the Barents Sea ($r = -0.93$, lag = 1 month, Figure 2.4e).

These correlations suggest that, when mode 1 is in positive phase, SST is warm in the Barents Sea, the sub-surface AW temperature is warmer than average, sea ice extent is low and SAT is warmer than average. A mechanism that could explain this mode is an increase in the temperature of the AW inflow to the Barents Sea, which would in turn reduce sea ice extent in

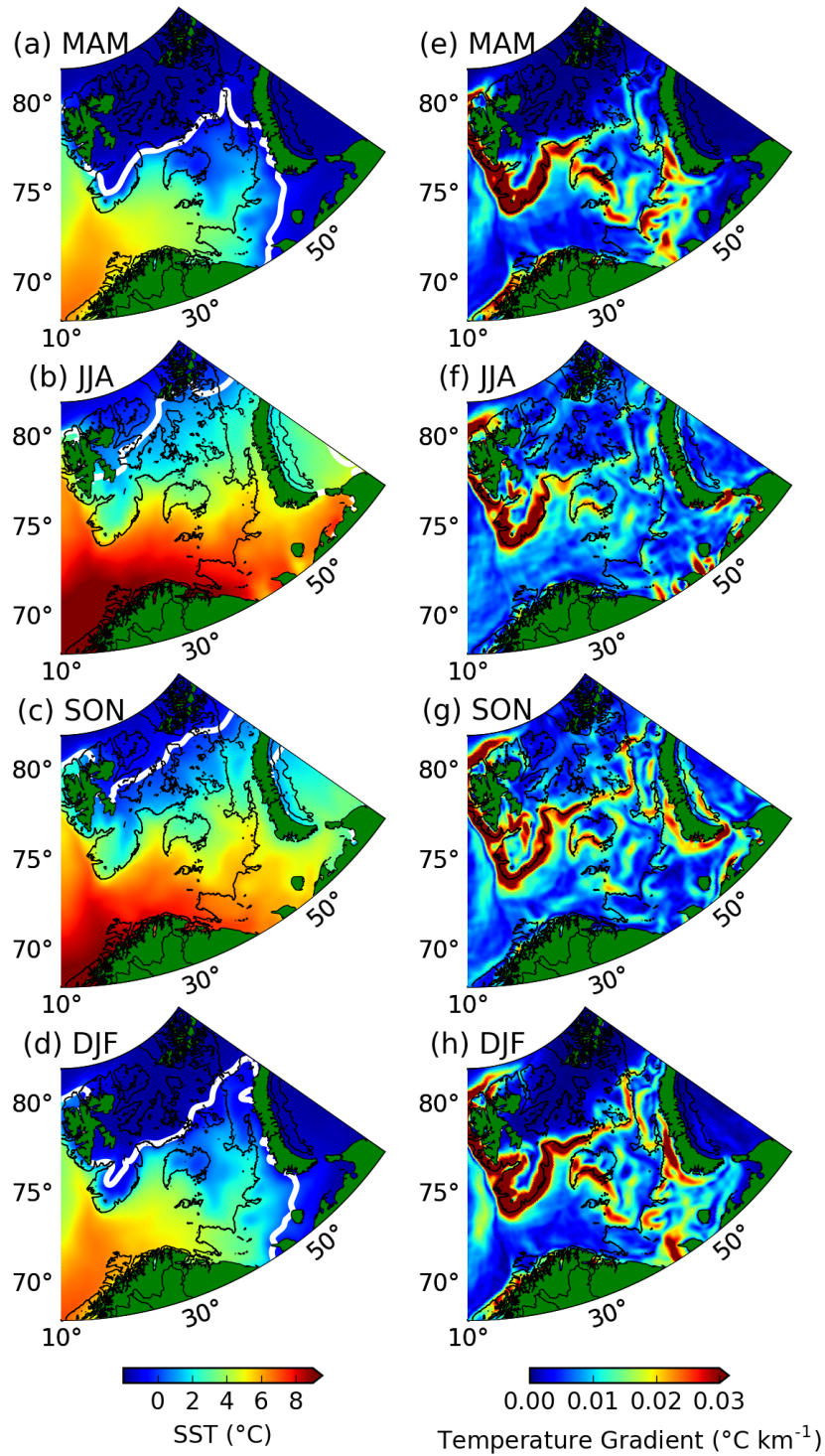


FIGURE 2.2 – SST seasonal climatology from 2005 to 2016 for (a) spring (March, April and May), (b) summer (June, July and August), (c) autumn (September, October and November) and (d) winter (December, January and February), respectively. Gradient in SST seasonal climatology from 2005 to 2016 for (e) spring, (f) summer, (g) autumn and (h) winter, respectively. The sea ice edge is defined by 15% sea ice concentration (white line) and the black line indicates the 220 m isobath.

the Barents Sea, both acting to increase AW heat loss to the atmosphere (Smedsrud et al., 2010) and resulting in warmer SAT. During a positive phase of this mode, both the increase of oceanic heat lost and the decrease of the sea ice extent will most likely affect the formation of BSW, as discussed in more detail in Section 2.5.

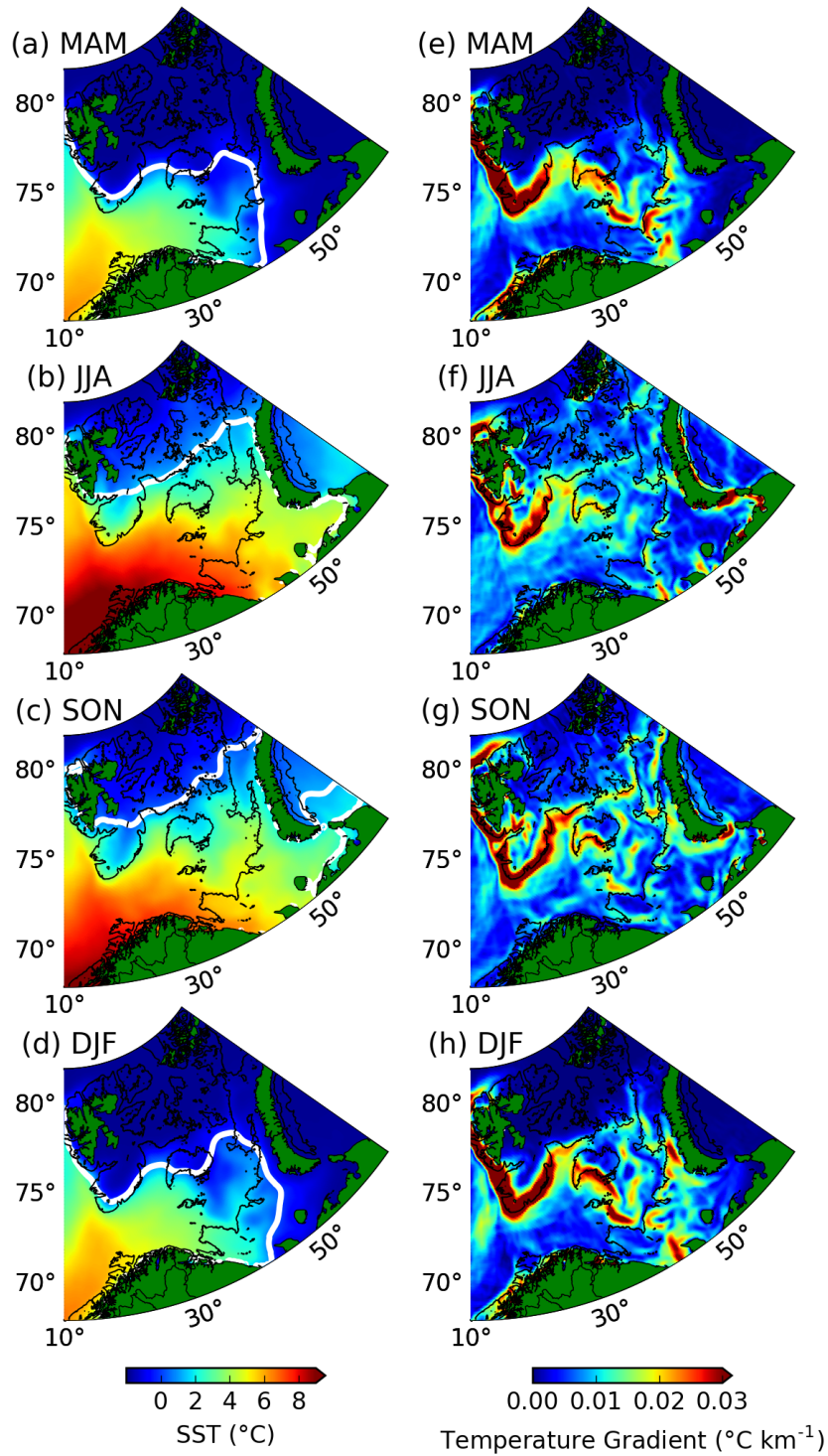


FIGURE 2.3 – As Figure 2.2 but for the seasonal climatology from 1985 to 2004.

We could not find a significant correlation between PC 1 and SLP variations across the Barents Sea. This is at odds with the results of [Herbaut et al. \(2015\)](#), which suggested a link between the variations in sea ice (and thus SST) and SLP. The different results could be due to the different periods considered as they only considered the variations up to 2004.

In summary, our lagged correlation analysis is consistent with heat carried in the AW inflow gradually influencing both SAT and BSW SST as it propagates from Fugloya-Bear Island section to the Kola section and onwards to the interior Barents Sea where SAT can feed heat back to SST. Our results suggest AW inflow temperature may be at least as important as SAT in setting

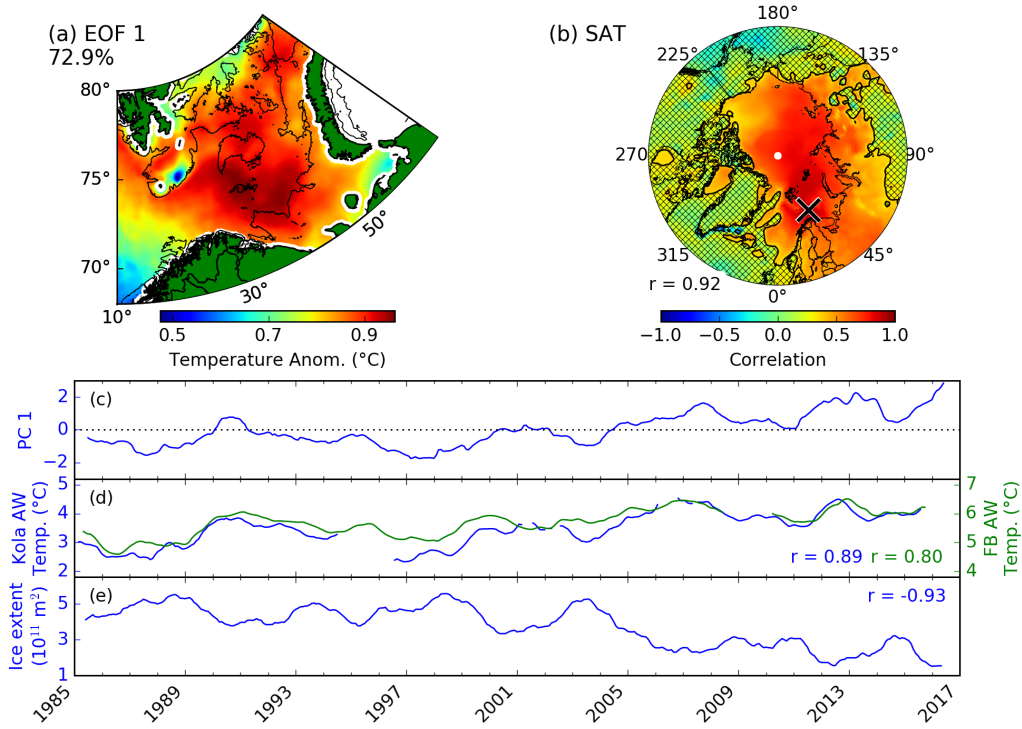


FIGURE 2.4 – (a) Spatial pattern of first EOF mode of SST variability. The black line indicates the 220 m isobath. (b) Regression of PC 1 with SAT. Maximum correlation (r-value) is shown in the bottom left hand corner and the location of the maximum correlation is shown by a black cross. Hatched areas are not significant at the 95%-level. (c) Time series of PC 1. (d) Time series of AW temperature at the Kola section (blue line, 12-month running mean applied) and Fugløy-Bear Island (FB) section (green line, 12-month running mean applied). (e) Time series of sea ice extent in the Barents Sea (12-month running mean applied). Correlations between each variable and PC 1 are indicated.

the Barents Sea SST. Indeed, this BSW-SST-forcing mechanism is supported by the conclusions of [Smedsrud et al. \(2010\)](#) who found that AW heat input has a bigger impact on SST variability than SAT forcing. The mechanism proposed here is also consistent with the results of [Schlichtholz and Houssais \(2011\)](#) who found that the temperature of recirculating AW exiting the Barents Sea through the BSO was driven by SAT within the Barents Sea.

We now examine the SST multidecadal variability. We find a significant positive linear trend of up to $0.05\text{ }^{\circ}\text{C year}^{-1}$ in the western Barents Sea for the period from 1985 to 2004 (pre-2005; Figure 2.5b). Post-2005 (2005 to 2016) however, the SST in the western Barents Sea stabilises, such that the trend becomes insignificant here while a positive trend of roughly $0.10\text{ }^{\circ}\text{C year}^{-1}$ arises in most of the eastern Barents Sea (Figure 2.5c). A positive trend is also found in the analysis of [Singh et al. \(2013\)](#) for the time period 2002 to 2010. The shift in SST trend since 2005 is consistent with the results of [Herbaut et al. \(2015\)](#), who found a significant reduction of both the mean and variance of the winter sea ice concentration after 2005. The positive trend in the eastern Barents Sea coincides with an increase in AW temperatures observed at the Kola section (Figure 2.4e). As AW temperature at the Kola section is correlated with PC 1, this suggests mode 1 also captured part of the variability at multidecadal or longer time scales. As suggested by [Smedsrud et al. \(2010\)](#), an increase in AW heat transport would manifest in an expansion of a warm heat anomaly in the Barents Sea basin resulting in an increase in the surface area in which heat loss takes place. The change in trend across the eastern Barents Sea could represent the expansion of this surface area.

Although the SST dataset is limited to 1985 onwards, there are other datasets which have been used to address longer term variability in the Barents Sea. A 16–20 year and 30–50 year timescale fluctuation was found in ~ 100 year observational datasets of both sea ice concentration

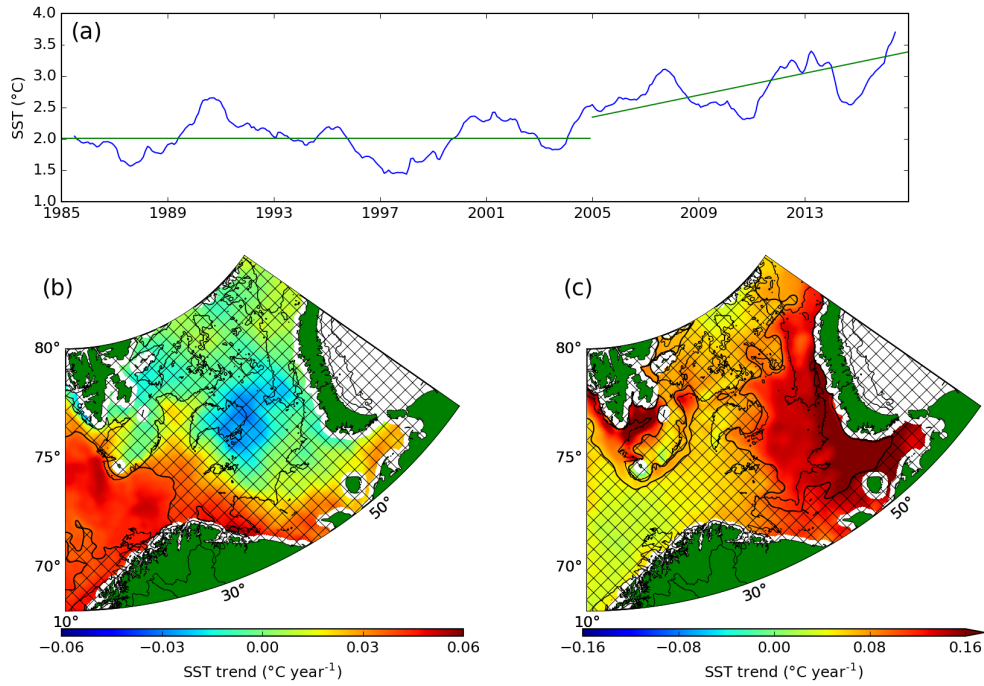


FIGURE 2.5 – (a) Mean SST across the Barents Sea with a 12-month running mean (blue line). The linear trend for the periods 1985 to 2004 and 2005 to 2016 are shown (green lines). Trend in SST for the periods (b) 1985 to 2004 and (c) 2005 to 2016. Note that a different colour scale is used in the two panels. Trends are significant at a level of 95% in un-hatched areas. The black line indicates the 220 m isobath.

and SLP (Venegas and Mysak, 2000). These timescales are too long to be fully resolved in our analysis period, so we can not fully distinguish between long term trend and natural variations occurring on these timescales. Yet, the results of Venegas and Mysak (2000) suggest that the sea ice extent variations on the 16–20 year timescale are likely linked with SLP anomalies. Our time period of 32 years should capture some variability at the 16–20 year time period which could be manifested as the change in temperature occurring in 2005. However, as our EOF 1 is not driven by SLP variations, we hypothesis that the change occurring in 2005 is likely the manifestation of a regime shift rather than natural variability causing SLP to become decoupled across this time period. This hypothesis is also supported by the analysis of the observed sea ice extent from 1850 onward by Onarheim and Årthun (2017), who found that the winter sea ice extent is at its lowest level since 1990. This is discussed in relation to long-term trends in Section 2.5.

2.4 The Polar Front’s Constraint on the Sea Ice Edge

The magnitude of the 2D gradient in SST shows the surface manifestation of fronts in the Barents Sea (Figure 2.2e-h). Starting in the west, a front follows Spitsbergen Bank but then bifurcates at Central Bank and splits into two branches (Figure 2.2e), in agreement with the results of Oziel et al. (2016). The southern branch of this front (referred to hereafter as the Barents Sea Front) follows the western side of Central Bank southward, dividing the Barents Sea into an AW-influenced western region and a BSW-influenced eastern region. The Barents Sea Front is most prominent during winter and spring (Figure 2.2e,h) and has been discussed in greater detail by Oziel et al. (2016, 2017).

Further to the north, the PF divides the eastern Barents Sea into an ArW-influenced northern region and a BSW-influenced southern region. Our results show the PF to be a persistent feature following the ~220 m isobath throughout the year, although Oziel et al. (2016) found that the PF was positioned further north than the present analysis with no fixed position. Their analysis

was limited by the dataset used, comprising temperature and salinity *in situ* profiles collected in the Barents Sea, which captures only the sub-surface expression of the front in the 50 to 100 m depth range. SST observations reveal that the PF pathway on the east side of the Barents Sea follows the southern sides of Great Bank and Ludlov Saddle eastward to Novaya Zemlya Bank (Figure 2.2e-h, see Figure 2.1 for locations). At Novaya Zemlya Bank, the PF extends northward along Novaya Zemlya Bank to 78° N. It should be noted that a second, weaker thermal-surface front exists in the SST data due to the transition from freezing ice-covered water to warmer ice-free water. The thermal-surface front does move with the sea ice edge and sometimes coincides with the more permanent PF.

Previous studies have investigated several aspects of the PF (Våge et al., 2014; Oziel et al., 2016) but the dynamics controlling it are still poorly pinned down. Here we present some evidences that the PF is controlled by potential vorticity constraints. Within the Barents Sea, the PF is closely tied to the 220 m isobath (Figures 2.2 and 2.3), which is located on a steep slope separating the northern and southern Barents Sea (Figure 2.1). Potential vorticity constraints usually force currents to flow along topographic contours rather than across them (Taylor, 1917; Proudman, 1916). Planetary potential vorticity (q) can be estimated by the equation $q = f/h$, where f is the coriolis parameter and h is the depth. The planetary potential vorticity contours in the Barents Sea follow closely the bathymetry contours as f is roughly constant in the region. In the case of a basin with a shallower northern outflow depth than inflow i.e. a ridge, an idealised model with potential vorticity constraints drives anticyclonic/clockwise circulation around the basin and eastward along the ridge in the northern hemisphere (Yang and Price, 2000). This is consistent with the path of the PF we resolved by the OSTIA SST (Figure 2.2), as well as the eastward flow found in velocity observations on the southwestern slope of Great Bank (Våge et al., 2014) and simulations showing eastward flow along the southern slope of Great Bank (Slagstad and McClimans, 2005; Lind and Ingvaldsen, 2012).

Following Pratt (2004), additional evidence that the PF is constrained by potential vorticity can be provided by estimating the Froude number associated with the flow across the ridge towards the eastern boundary (i.e Novaya Zemlya Bank in our case). The Froude number is given by $F = u/(g'd)^{1/2}$, where u is current speed, g' is reduced gravity and d is depth of the layer at the ridge. Here we take $u = 0.2 \text{ m s}^{-1}$ (based on observations by Våge et al. (2014), assuming current speed is constant along the ridge), and values for g' and d are calculated from MIMOC data (Figure 2.6), obtaining a Froude number of 0.3. Following the argument developed by Pratt (2004) and given that in our case the height of the ridge occupies roughly $1/3$ of the water column, a Froude number greater than 0.2 suggests that the Great Bank–Ludlov Saddle ridge imposes a hydraulic control on the flow associated with the PF, providing further evidence that the PF is constrained by potential vorticity.

We next examine time variations of the PF, in relation to the position of the sea ice edge over time. According to Smedsrud et al. (2010), the PF sets the limit on surface area available for winter heat loss over the Barents Sea. Logically, the PF may also play a role in determining the volume of summer freshwater input from sea ice melt water. Thus the interplay between the eastern Barents Sea PF and mobile sea ice edge mediates the properties of BSW that will be carried into the Arctic as AIW. A comparison of SST gradients and sea ice concentration shows that the sea ice edge follows the inner edge of the PF in both the eastern and western Barents Sea during winter and spring from 2005 to 2016 (Figure 2.2a-d, white line) but this was not the case before 2005 (Figure 2.3, white line). Steele and Ermold (2015) suggest that during the expansion and retreat of seasonal sea ice, the edge loiters at fronts where there is a gradient in temperature inhibiting further expansion. This then implies that the expansion of sea ice south of the PF before 2005 could be consistent with cooler SST or stronger northerly winds enabling greater transport of the mobile sea ice pack across the PF enabling it to loiter closer to the Barents Sea Front.

We then focus on the interannual variability of the PF and its relationship with the sea ice edge (Figures 2.7). To perform this analysis, the SST gradient is calculated meridionally and these gradients are averaged zonally within the box shown as a blue-dashed line on Figure 2.1.

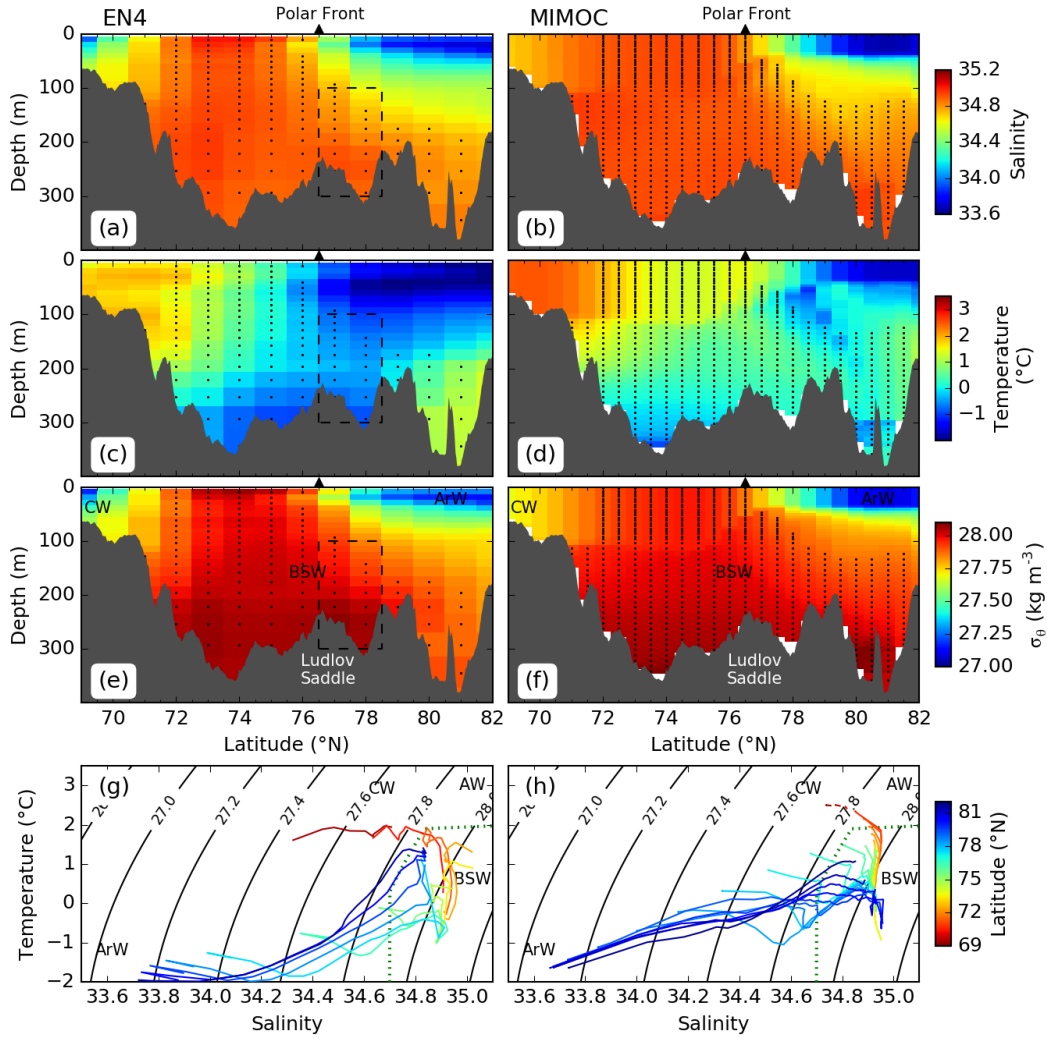


FIGURE 2.6 – Eastern Barents Sea transect at 44° E (shown in Figure 2.1) from the MIMOC and EN4 climatology during winter (December, January, February), EN4 is averaged over 1985 – 2016. The Polar Front is marked by the black triangle. (a,b) Salinity, (c,d) temperature and (e,f) potential density. White areas in (a-f) indicate grid cell with no data, black points show the grid cells containing BSW, and the EN4 sub-section (black dashed area) used to produce the BSW temperature and salinities (Figure 2.7). (g,h) T-S diagrams showing the different water masses present in (a-f). The color indicates the latitude of the profile. The green dotted area in (g,h) shows the limits of the BSW definitions, and AW, ArW and CW water masses are indicated (see Table 1.1 for their definitions)

Zonally-averaged SST gradients on a given day are normalized by the daily standard deviation of the gradient in the same analysis box (Figure 2.1), in order to remove to potential large effect of the strong seasonality and interannual variability in the intensity of the SST gradient and sea ice extent. Figures 2.7(a) shows that the PF is persistent in its location throughout the majority of the year. Between 1985 and 2004, the PF was covered by sea ice for parts of winter and spring but held position at 76.5° N, rather than moving south with the advancing winter sea ice edge as previously thought (Smedsrud et al., 2010). As expected, there is also a thermal-surface front at the position of the sea ice edge to the north of the PF in summer, but the PF is always present as a stronger and more persistent front at 76.5° N along the 220 m bathymetry contour.

A change in the location of the winter sea ice edge relative to the position of the PF is also evident on decadal timescales (Figure 2.7). Unlike in the pre-2005 period, since 2005, the winter sea ice edge has been unable to sustain a southwards breach of the PF for more than a few days (Figure 2.7b). We define a region in the Barents Sea between the PF to the north and the Coastal

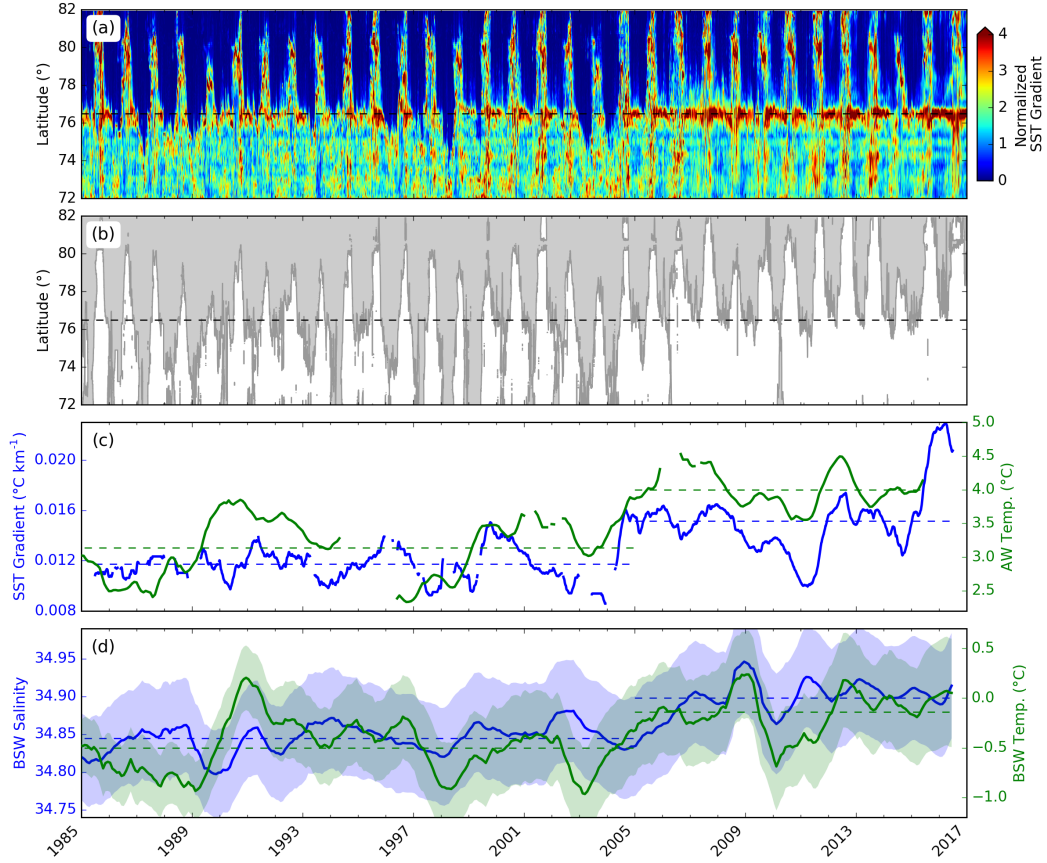


FIGURE 2.7 – (a) Magnitude of the meridional gradient in zonally-averaged SST between 35° E and 50° E (blue-dashed box on Figure 2.1) and Polar Front location (dashed line). The magnitude is normalized on a daily basis by its standard deviation to show the changes in the position of the front over time. Note that changes in intensity over time cannot be deduced from (a). (b) Latitude of the sea ice edge for the same region. (c) mean SST gradient between 76.3° N and 76.7° N before normalization (blue line, 12-month running mean applied) and AW temperature from the Kola section (green line, 12-month running mean applied, section marked in Figure 2.1). Gaps indicate missing data and sea ice coverage for AW and the SST gradient respectively. (d) BSW salinity (blue line) and temperature (green line) between 100 and 300 m from the EN4 data, averaged in the cyan-dashed box on Figure 2.1. Uncertainty values for EN4 data are shown by the shaded areas. Dashed green and blue lines in (c) and (d) show the respective means for 1985 – 2004 and 2005 – 2016.

Water front to the south shown by the dark-blue box in Figure 2.1, within which sea ice melt can be entrained into BSW. The change in 2005 has reduced the mean seasonal change in sea ice area in this region, from 77 000 km² between 1985 and 2004 to 8 700 km² between 2005 and 2016. This provides useful information in efforts to predict the location of the winter sea ice in the Barents Sea (examples of predictions include [Onarheim and Årthun \(2017\)](#); [Sigmond et al. \(2016\)](#); [Nakanowatari et al. \(2014\)](#)). This is important because changes in sea ice conditions in the Barents Sea have been linked to widespread, anomalous atmospheric conditions over northern continents ([Petoukhov and Semenov, 2010](#); [Yang et al., 2016](#)).

At the same time, while remaining fixed to topography, the mean SST gradient across the PF increases significantly from $0.011 \pm 10^{-4} \text{ °C km}^{-1}$ pre-2005 to $0.015 \pm 10^{-4} \text{ °C km}^{-1}$ in post-2005 (Figure 2.7c). This steepening in the PF SST gradient coincides with a significant increase in AW temperature at the Kola section from $3.1 \pm 0.05 \text{ °C}$ in the pre-2005 period to $4.0 \pm 0.05 \text{ °C}$ in the post-2005 period. Given that the SST north of the PF is changing at a slower rate than south of the PF (Figure 2.5), the intensification of the PF can then be mainly attributed to the increase in AW temperature in the Barents Sea. One important consequence of the increase in

AW temperature is that the heat content on the southern side of the front prevents sea ice from accumulating. A link between changes in sea ice and AW temperature has been discussed by [Smedsrud et al. \(2013\)](#) but not in relation to the PF. We assess this result in relation to trend and long-term variability in Section 2.5.

In addition to the changes found in the southern side of the front, discussed above, changes in the properties of the ArW north of the PF could also occur. To the northeast of Svalbard where the AW lies close to the surface, [Ivanov et al. \(2016\)](#) have suggested that a positive feedback could exist between entrainment of warm AW and reduced midwinter sea ice thickness, due to a dilution of the freshwater stratification driven by change in salinity allowing more heat into the upper layer in contact with the sea ice. The mean ArW properties from EN4 pre-2005 were $T = -1.15 \pm 0.04$ °C, $S = 34.463 \pm 0.014$; while post-2005 they were $T = -0.76 \pm 0.06$ °C, $S = 34.569 \pm 0.022$ (Figure 2.1 shows the cyan-dashed box selected for ArW properties north of the PF). This significant increase in temperature and salinity could be caused by a similar process to the one described by [Ivanov et al. \(2016\)](#) where the reduced density gradient allows further heat to mix into the layer in contact with sea ice.

The mean surface BSW properties pre-2005 were $T = -0.22 \pm 0.03$ °C, $S = 34.828 \pm 0.009$; while post-2005 they significantly increased to $T = 0.50 \pm 0.05$ °C $S = 34.943 \pm 0.013$ (Figure 2.1 shows the yellow-dashed box selected for surface BSW properties south of the PF). The salinity increase is comparable for the surface BSW and ArW within the error bounds, but the increase in the temperature of surface BSW is almost double the change in ArW temperature over the same period. The result on ArW density and surface BSW density is an increase of 0.071 ± 0.017 kg m⁻³ and 0.054 ± 0.009 kg m⁻³, respectively, indicating a decrease in the density gradient across the PF after 2005. This suggests that the steepening of the temperature gradient and weakening of the density gradient across the PF in the eastern Barents Sea are primarily driven by changes occurring in the southern side of the PF.

Transect data through the eastern Barents Sea (Figure 2.6) show the SST gradient across the PF is the surface expression of a vertically-coherent front. In both the EN4 and MIMOC climatologies, the PF is present near 76.5° N as a negative south-north temperature gradient over the depth range 0 – 100 m, and a similar sub-surface salinity gradient. The PF is a transition between the southern region that is temperature-stratified (α -ocean) and the northern region that is salinity-stratified (β -ocean) ([Carmack, 2007](#)). Here, α is the coefficient of thermal expansion and β is the coefficient of haline contraction. This makes the PF an important transition zone where the contribution to density from temperature and salinity can be in balance. Note the presence of water that is too fresh to fit the BSW definition and too warm to fit the ArW definition between 77° N and 78° N over 0-50 m (Figure 2.6b,d). This water mass sits on the mixing line between BSW and ArW (Figure 2.6h), suggesting that mixing between BSW and ArW occurs at the front. Previous studies based on observations in the western Barents Sea have revealed the presence of interleaving between BSW and ArW along the PF that could enhance mixing ([Parsons et al., 1996](#); [Våge et al., 2014](#); [Fer and Drinkwater, 2014](#)).

On the northern side of the transect, the ArW layer (Table 1.1) is present in the MIMOC data over the depth range 0 – 100 m at 80° N and extends down to 50 m at 77° N. In EN4, the ArW layer extends to a deeper depth of 150 m at 80° N and 100 m at 77° N. The main difference between the EN4 climatology and the MIMOC climatology is the 1 °C cooler temperature of BSW in the EN4 than in MIMOC (Figure 2.6c,d). This may represent a change in BSW temperature over time given that the MIMOC climatology is weighted to be characteristic of 2007 – 2011 whereas the EN4 climatology is an average over the period 1985 – 2016. Regardless of the difference in temperature between the two datasets, BSW occupies roughly the same area (black dots in Figure 2.6e,f). As BSW is denser than ArW (Figure 2.6g,h), it sits below ArW north of the PF at 76.5° N. From Ludlov Saddle, BSW flows eastward and exits the Barents Sea through St. Anna Trough in a layer below ArW ([Schauer et al., 2002](#)). As the Central Basin is the source of BSW ([Oziel et al., 2016](#)), this suggests BSW propagates northwards of the PF either by subducting below ArW or by undergoing modification at the surface due to fast-mixing processes in the the upper portion of BSW that [Rudels et al. \(1996\)](#) has hypothesized occurs

during winter heat loss.

2.5 Atlantification of the Barents Sea and Implications for Barents Sea Water

As a consequence of the intensification of the PF since 2005, it now forms a persistent barrier to the formation and export of sea ice south of the PF (Figure 2.7). Having identified the forcing on BSW in Section 2.3, here we discuss the possible implications of the barrier imposed by the PF on the properties of the BSW exiting the Barents Sea :

1. The northern limit of the surface area available for AW winter heat loss has become fixed to the location of the PF. The sub-surface EN4-averaged BSW temperature has warmed from -0.51 ± 0.03 °C to -0.13 ± 0.03 °C when comparing the pre-2005 and post-2005 periods (Figure 2.7c, averaged over 100 – 300 m in the cyan-dashed box in Figure 2.1). The increase of the temperature at the Kola section between the same two periods is more than twice as large (0.9 °C). The observed reduction in Barents Sea ice extent has resulted in an increase of the surface heat flux from the ocean to the atmosphere (Long and Perrie, 2017; Årthun et al., 2012), likely explaining the different rate of temperature increase between the BSW and the Kola section.

Before 2005, the expansion and retreat of sea ice in the eastern Barents Sea buffered BSW properties against changes in AW temperatures (Smedsrud et al., 2010), but our analysis suggests that this buffering capacity has reduced since 2005, enabling the temperature increase of BSW in recent years visible on Figure 2.7d. Such a temperature change requires that most of the AW heat is lost to the atmosphere in the ice-free southern Barents Sea (which is consistent with the results of Smedsrud et al. (2010)) and that the heat lost by BSW through mixing with ArW north of the PF is small. While Lind et al. (2016) have pointed out that mixing between ArW and BSW can exist, in particular during years with lower sea ice cover, the heat lost through that process is most likely much smaller than the heat lost to the atmosphere south of the PF.

2. Given that most of the sea ice is imported to the Barents Sea (Ellingsen et al., 2009), the reduction of sea ice south of the PF reduces the seasonal freshwater input to BSW associated with local sea ice melt. Based on their model simulations, Ellingsen et al. (2009) found that between 1979 and 2007, melt water from imported sea ice contributed 0.02 Sv of freshwater on average. This is enough to decrease the mean salinity of their simulated 1.1 Sv AW inflow (salinity 35.1) to salinity of 34.4. However, in their study, Ellingsen et al. (2009) does not account for the PF's role in partitioning sea ice meltwater between BSW and ArW, and considers that the input of sea ice meltwater takes place entirely south of the PF, and thus can convert AW into ArW. Here we revisit their calculation, taking into account the partitioning of meltwater at the PF.

To calculate the meltwater input south of the PF before 2005, we assume that the sea ice found south of the front was 1 m thick, which is a typical thickness for first-year ice in the Barents Sea (Ellingsen et al., 2009; Smedsrud et al., 2010). In contrast to Ellingsen et al. (2009), we only consider the box that contains the area south of the PF and north of the Coastal Water front shown by the dark-blue box on Figure 2.1, and assume that the AW is not modified before it enters that box. Within this box, the reduction in sea ice area south of the PF by 68 300 km² between the pre and post-2005 periods (Figure 2.7) corresponds to a 0.0022 Sv reduction in the freshwater input south of the PF after 2005 when the sea-ice is no longer present. This is assumed to mix ubiquitously into BSW.

To calculate the dilution of AW by sea ice melt, we estimate the volume to be diluted by comparing the AW inflow to the BSW outflow. Following Gammelsrød et al. (2009), we assume a BSW transport leaving the Barents Sea between Novaya Zemlya and Franz-Josef Land of 1.25 Sv (observed transport scaled up by the difference between virtual current meters and modeled, whole-section transport). For comparison the net annual

observed AW inflow through the BSO is 1.1 – 1.2 Sv (Skagseth, 2008; Ingvaldsen et al., 2004b) (excluding transport associated with Norwegian Coastal Current). This implies that there is no net storage of BSW in the Barents Sea, such that the volume of AW to be diluted is $V_{AW} = 1.1$ Sv (note, a change of AW volume transport across our time period cannot be estimated from the available observations).

The salinity of inflowing AW should also be taken into account when calculating a change in BSW salinity. As shown on Figure 2.4d, the mean properties of AW at the Fugløy–Bear Island section for 1985 to 2005 were $T = 5.44 \pm 0.06$ °C, $S = 35.067 \pm 0.003$ and for 2005 to 2016 they were $T = 6.08 \pm 0.07$ °C, $S = 35.120 \pm 0.005$ (the changes between the two periods are significant). Using these different salinity values and considering that the input of freshwater south of the PF vanishes after 2005, we perform a simple dilution calculation, following the equation : $C = [M_{AW} + M_{FW}] / [V_{AW} + V_{FW}]$, where C is the concentration of salt, M is the mass of salt and V is the volume, AW is Atlantic Water and FW is fresh sea ice meltwater. We also assume a constant salinity value of 3 for first-year sea ice (Ellingsen et al., 2009), and constant net AW inflow (BSW outflow) of 1.1 Sv (1.25 Sv) (Skagseth, 2008; Gammelsrød et al., 2009). Based on this framework, pre-2005 the mean input of 0.0022 Sv of freshwater results in a reduction of -0.063 (-0.056) of the BSW salinity, while post-2005, the BSW salinity would equal the AW salinity which additionally increased by 0.053 across this time period. Our dilution calculation predicts a change of BSW salinity by ~ 0.11 , which is in broad agreement with the significant increase of BSW salinity estimated from the EN4 dataset (from 34.844 ± 0.003 to 34.900 ± 0.002 , Figure 2.7c). This suggests that the increase in BSW salinity is likely a combination of the change in sea ice area and the change in inflowing AW salinity.

When comparing the mean BSW temperature over the two periods in EN4, it increases by 0.38 °C, which is about a half of the 0.8 °C required to compensate density changes arising from the 0.056 mean salinity increase observed. These changes in temperature and salinity have led to a significant increase of BSW density from 1029.092 ± 0.002 kg m⁻³ pre-2005 to 1029.116 ± 0.002 kg m⁻³ post-2005.

The 0.024 kg m⁻³ increase in BSW density between the two periods has to be compared against the gain in density resulting from the transformation of AW to BSW. Pre-2005, the density transformation amounted to ~ 0.33 kg m⁻³, a combination of 5.9 °C decrease and 0.23 salinity decrease (based on AW properties at the BSO). This means a further 8% density change in BSW relative to the pre-2005 era.

Our comparison of the two periods (pre and post 2005) suggests that a regime shift occurred in 2005. Yet, one needs to remember that there is well-known multidecadal variability affecting SLP, sea ice concentration, SAT and AW temperature (Venegas and Mysak, 2000; Smedsrud et al., 2013; Levitus et al., 2009; Ingvaldsen et al., 2003). Variability at a 30–50 year frequency is thought to be driven by the Atlantic Multidecadal Oscillation, suggesting that long-term variations in the Barents Sea are driven by large-scale fluctuations (Levitus et al., 2009). These variations are also affecting the formation, properties and volume of BSW on similar timescales (Årthun et al., 2011). Analysis by Onarheim and Årthun (2017) of an observed time-series of winter sea ice extent from 1850 to 2017 in the Barents Sea complemented by analysis of climate simulations also emphasises the existence of variations with a 50 year periodicity. However, their results show winter sea ice extent in the Barents Sea has been lower since the 1990 than in the the rest of the time period and that there is an unprecedented negative trend in the last 30 years that has less than 5% probability of occurring in all preindustrial simulations. This suggests that winter sea ice in the Barents Sea has most likely not been inhibited by the PF during 1850 to 2005. Further evidence comes from the observations by Smedsrud et al. (2013), suggesting that Arctic SAT and AW temperature at the Kola section were both greater after ~ 2000 than at any time from the last century.

2.6 Conclusion

The goal of this study was to investigate how changes and feedbacks between sea ice and the PF in the Barents Sea may have affected BSW properties over the past decades. We have identified and located the PF in the eastern Barents Sea using satellite SST observations, a feature that has been obscured by seasonal sea ice between 1985 and 2004. While a summer mixed layer and seasonal front does form in association with the melt of seasonal sea ice, as is the case in other regions (Dewey et al., 2017), the PF persists throughout the year as a front with steeper gradients in salinity and temperature in the eastern Barents Sea at 76.5° N, running parallel to the 220 m isobath (Figure 2.2). The PF is a potential vorticity-constrained, shelf slope current at the steep ridge formed by Great Bank and Ludlov Saddle. Since 2005, the sea ice is inhibited in its winter southward extent by the increase in temperature gradients across the PF, a change most likely driven by an increase in AW temperature.

Our results provide new evidence that, in addition to the natural multidecadal variability, the Barents Sea is currently undergoing atlantification, with the corresponding temperature and salinity increases catalysed by the observed PF constraint on the sea ice edge. The loss of winter sea ice south of the front represents a loss of freshwater input to BSW, a water mass which makes up 50 – 80% of AIW. As the stationary PF, rather than the mobile sea ice edge, has become the limiting factor controlling the northern boundary of the surface area available for AW cooling in winter, the buffering effect to BSW temperature from the variations of sea ice conditions has decreased. Observations show a change in BSW properties over the same time period resulting in denser BSW, which could in turn result in a deeper settling depth of BSW once exported to the Arctic Basin through St. Anna Trough (Dmitrenko et al., 2015), with potential far-reaching impacts for the dense water outflow through Fram Strait (Lique et al., 2010; Moat et al., 2014) or the density of the Denmark Strait overflow (Karcher et al., 2011), both of which are important for the deeper branch of the AMOC.

Chapitre 3

Water mass properties derived from satellite observations in the Barents Sea

This is a reproduction of the paper under review in 2019-2020 : B. I. Barton, C. Lique and Y.-D. Lenn. Water mass properties derived from satellite observations in the Barents Sea. Journal of Geophysical Research : Oceans. Under review 2020.

3.1 Introduction

The Barents Sea acts as a gateway for Atlantic Water (AW) entering the Arctic Ocean, and has become both warmer and saltier between 1980 and 2016, a phenomenon referred to as "atlantification" ([Årthun et al., 2012](#); [Oziel et al., 2016](#); [Lind et al., 2018](#); [Barton et al., 2018](#)). Approximately 2 Sv of AW enters the Barents Sea through the Barents Sea Opening between Norway and Bear Island ([Skagseth, 2008](#)). As AW flows through the eastern Barents Sea it loses heat to the atmosphere and gains freshwater from net sea ice melt and precipitation, transforming into cooler, fresher Barents Sea Water (BSW) ([Schauer et al., 2002](#); [Ellingsen et al., 2009](#); [Long and Perrie, 2017](#)). Once formed, BSW sinks below the fresher Arctic Water (ArW) and flows into the Arctic Basin through St Anna Trough making up 50 to 80 % of Arctic Intermediate Water (AIW) ([Schauer et al., 1997](#); [Maslowski et al., 2004](#); [Aksenov et al., 2010](#)). It has been shown that variability in BSW density impacts the density of AIW exiting the Arctic Basin through Fram Strait, a contributor to the deeper branch of the Atlantic Meridional Overturning Circulation (AMOC) ([Lique et al., 2010](#); [Moat et al., 2014](#)). Warmer AW entering the Barents Sea caused a sea ice regime shift in the mid-2000's, limiting the southward extent of winter sea ice and resulting in warmer and saltier BSW ([Barton et al., 2018](#); [Lind et al., 2018](#)). The sea ice loss and the increased ocean to atmospheric heat flux have been linked to anomalous weather conditions in northern Europe, Russia and Asia ([Petoukhov and Semenov, 2010](#); [Hoshi et al., 2019](#)). Monitoring the variations and changes in the properties of BSW is thus relevant for understanding the atmospheric and ocean changes, locally in the Barents Sea and beyond.

The Barents Sea is occupied by several water masses, with different properties and water column structures (for water mass properties see Table 1 in ([Barton et al., 2018](#))). The heat and freshwater contents corresponding to these different water masses can be estimated from *in situ* measurements. In general, heat content decreases poleward as oceanic heat (gained at lower latitudes) is progressively lost to the atmosphere ([Carmack, 2007](#)). This spatial gradient in heat content reaches a threshold within the Barents Sea where density and stratification becomes more dependant on salinity than temperature as water approaches temperatures close to the freezing point. The stratification resulting from temperature and salinity variations can be quantified in terms of alpha α (the coefficient of thermal expansion) and beta β (the coefficient of haline contraction) contribution to the density, respectively ([McDougall, 1987](#); [Carmack, 2007](#)). The weakly-stratified $\alpha - \beta$ transition zones between regions where stratification is dominated by α or β can be classed as "spice-stratified" regions ([Stewart and Haine, 2016](#)). The classification between α or β regions is important when trying to investigate the variations of steric height (the depth-integrated inverse density resulting in expansion and contraction of the water resulting from both temperature and salinity changes), a key parameter to understand the ocean dynamics ([Giglio et al., 2013](#)). In the salinity-stratified deep basins of the central Arctic Ocean, freshwater content variability thus accounts for most of the variability in steric height ([Armitage et al., 2016](#)), and ArW in the northern Barents Sea is also known to be salinity stratified ([Loeng, 1991](#)). Along the coast of Norway where AW influence is stronger, heat content is more important than freshwater content for steric height variability ([Richter et al., 2012](#)). In the case of BSW, due to the seasonality of heating-cooling and freshwater addition from freeze-thaw, it is possible that BSW is temperature stratified in summer and salinity stratified in winter ([Loeng, 1991](#)). As an $\alpha - \beta$ transition zone resides within the Barents Sea, it is equally important to quantify heat and freshwater content here in order to accurately resolve water mass properties. This close balance between heat and freshwater content in the Barents Sea means pioneering work has attempted to use satellite data to calculate the heat and freshwater components of steric height but with limited *in situ* validation ([Volkov et al., 2013](#)). This study focuses on the formation region of BSW in the Barents Sea Central Basin (purple box Figure 3.1) ([Schauer et al., 2002](#); [Oziel et al., 2016](#)).

Winter in the Barents Sea can be hostile for *in situ* ship measurements and Argo floats are generally not deployed here. While the Barents Sea is reasonably well-sampled by *in situ* observations during the ice-free season, these observations remain overall sparse in time and space, in contrast to satellite observations that provide us with continuous measurements regardless of

the season. Satellite measurements of the ocean surface have been obstructed by sea ice, however, recent advances enable sea surface height (SSH) observations in ice-covered areas (Armitage et al., 2016). The presence of sea ice has previously been identified as a problem causing unresolved high frequency signals in comparison of satellite and tide gauge SSH (Volkov and Pujol, 2012). These under ice satellite altimetry data can be combined with satellite observations of ocean bottom pressure (OBP) to obtain steric height (Swart et al., 2010; Armitage et al., 2016; Volkov et al., 2013). Satellites are also able to measure the sea surface temperature (SST) and sea surface salinity (SSS). At the interannual time-scales, SST has been linked to depth-integrated heat content in the Barents Sea (Lique and Steele, 2013; Chepurin and Carton, 2012).

This analysis addresses the question of whether satellite data can be used to obtain information on the heat and freshwater content variations within the water column and in particular to measure BSW variability. We also examine the interannual variability in BSW heat and freshwater content in a reconstructed time-series from satellite data. We choose the Barents Sea as a test site for this study due to the relatively large collection of historic hydrographic profiles, and its importance to atmospheric circulation and BSW properties in the wider Arctic Ocean.

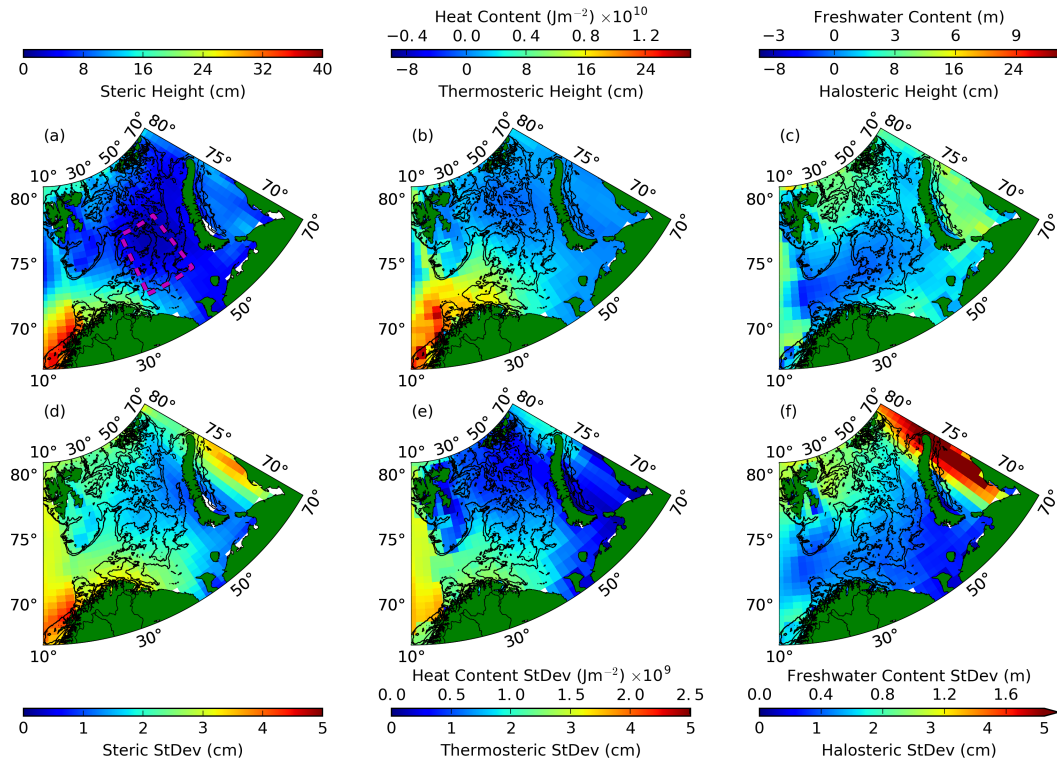


FIGURE 3.1 – Average over 2003–2013 (a) *in situ* steric height, (b) *in situ* heat content and *in situ* thermosteric height, (c) *in situ* freshwater content and *in situ* halosteric height estimated from EN4. (d), (e) and (f) show the standard deviation of *in situ* steric height, heat content, thermosteric height, freshwater content and halosteric height, estimated from the monthly means. The purple box in (a) shows the Central Box, covering the Central Basin and Central Bank, where the time series are averaged over for investigations of BSW variability (see Section 3.4). Black lines shows the 220 and 300 m isobaths.

3.2 Data and Methods

3.2.1 Data

SSH data is provided by the Centre for Polar Observation and Modelling (CPOM) (Armitage et al., 2016). In order to obtain SSH everywhere in the Barents Sea, including under sea ice, a processing technique has been applied to satellite altimeter data that takes into account the

difference in character of satellite echo-return signals from a specular surface (ocean between leads) and non-specular surfaces (snow, sea ice etc.) (Laxon, 1994; Giles et al., 2012). The product has previously been used to examine Arctic Ocean circulation (Armitage et al., 2017; Regan et al., 2019). The data are monthly from January 2003 to December 2013 with resolution of 2° longitude by 0.5° latitude (58 km by 56 km in the Barents Sea) and an estimated uncertainty of 1.1 cm (Armitage et al., 2016).

The twin Gravity Recovery and Climate Experiment (GRACE) satellites measure time varying OBP through changes in Earth’s gravity anomalies (Wahr et al., 1998). OBP is the sum of atmospheric mass and ocean mass (eustatic height). Therefore, ocean mass can be determined by removing the local inverted barometer effect and the global-spatially-averaged sea level pressure, following (Peralta-Ferriz et al., 2014). We use gridded equivalent water column height (corrected for atmospheric pressure and tides) from the GRCtellus Ocean monthly dataset available from August 2002 to December 2016 (version RL05.DSTvDPC1401, downloaded from ftp://podaac-ftp.jpl.nasa.gov/allData/tellus/L3/ocean_mass/RL05). This dataset is the ensemble mean of the results from Center for Space Research (CSR), Jet Propulsion Laboratory (JPL) and Geoforschungs Zentrum Potsdam (GFZ). Data are provided at 1° resolution with 500 km Gaussian smoothing applied (for comparison Novaya Zemlya is ~ 800 km long). The root mean square error (RMSE) estimate for one of the ensemble members is 1.5 – 2 cm at high latitudes (Chambers and Bonin, 2012; Peralta-Ferriz et al., 2016) but using the ensemble mean decreases the RMSE by at least 0.3 cm, resulting in a RMSE of 1.2 cm in the Barents Sea (Sakumura et al., 2014). This dataset has been validated with both altimetry and Argo floats globally (Chambers and Willis, 2010) and with *in situ* ocean bottom pressure sensors in the Arctic Ocean, the Barents Sea and Kara Sea (Peralta-Ferriz et al., 2016).

We also make use of satellite SST data from the OSTIA project spanning 1985 to present (Donlon et al. (2012); downloaded from marine.copernicus.eu portal). This dataset is optimally interpolated from multiple satellite sensors together with *in situ* observations onto a 0.05° grid (1.5×5.6 km for Barents Sea) at a daily frequency. The feature resolution is 10 km and the accuracy of the daily data is ~ 0.57 K (Donlon et al., 2012). At the current spatial and temporal resolution, this dataset can not resolve mesoscale variability (with a characteristic scale of only a few kilometers) in the Barents Sea, but has been shown to be able to capture fronts in the region (Barton et al., 2018).

Temperature and salinity fields from the EN4 dataset are analysed for comparison with satellite data (EN4.2.0, www.metoffice.gov.uk/hadobs/en4). EN4 comprises *in situ* ship CTD profile data and Argo float data optimal-interpolated on a 1° , monthly z-grid with 42 levels (Gouretski and Reseghetti, 2010). Data are available from January 1980 to December 2016. Within the Barents Sea (10°E to 65°E and 68°N to 80°N) over this time frame, every three-month period has more than 117 profiles. These profiles are biased towards September, October, November when there are usually more than 400 profiles.

We also make use of the fields of surface heat flux, evaporation and precipitation from the ECMWF ERA-Interim reanalysis (Berrisford et al. (2011); www.ecmwf.int). This dataset is provided on a 0.75° grid (84×16 km for Barents Sea) with 3-hourly temporal resolution, averaged into monthly means. Data are available from January 1979 to December 2018.

Bathymetry is taken from the GEBCO 2014 30 arcsecond resolution dataset (Weatherall et al. (2015); GEBCO_2014 Grid, version 20150318, www.gebco.net). In the Barents Sea, it corresponds to a resolution of 0.2 km in longitude and 0.9 km in latitude.

In the following analysis, we focus on the period when all the observational datasets are available, that is January 2003 to December 2013. EN4, GRACE, OSTIA and ECMWF data are linearly interpolated on the same grid as the CPOM SSH. By default GRACE data is masked around land; before interpolation onto the CPOM SSH grid we extrapolate GRACE data spatially towards the coastal areas by one grid cell using weighted averaging of the nearest neighbours. This is reasonable given that GRACE data has a 500 km filter.

3.2.2 Methods

In this section we explain the methods developed in order to estimate heat and freshwater content from satellite observations. We know that steric height can be calculated via three methods : (i) from SSH and eustatic height (Armitage et al., 2016), (ii) from halosteric and thermosteric heights (Gill and Niiler, 1973; Volkov et al., 2013) and (iii) through the integration of *in situ* density (Roquet et al., 2015). Here, we regard steric height derived from integrating EN4 data as the ground-truth data for validating the satellite-inferred estimates. Thermosteric and halosteric heights can also be derived from temperature and salinity profiles and are statistically proportional to heat and freshwater content (Steele and Ermold, 2007). We convert heat and freshwater content to halosteric and thermosteric heights, giving us parameters with the same units as steric height (in m). Our methods for estimating the various components of sea surface height are as follows :

1. Obtaining steric height from satellite data is done using the following equation (Armitage et al., 2016) :

$$\eta_{st} = \eta_H - \eta_m \quad (3.1)$$

with η_{st} the steric height, η_H the SSH and η_m the eustatic height.

Steric height can also be obtained from *in situ* profiles using the integral of specific volume anomaly from a reference pressure (i.e. the dynamic height anomaly) (Roquet et al., 2015).

$$\eta_{st}(t) = \frac{1}{g} \int_{p_2}^{p_1} \frac{1}{\rho(z, t)} - \frac{1}{\rho_{ref}(z)} dp \quad (3.2)$$

with g the gravity taken as 9.7963 m s^{-2} , p_1 and p_2 the ocean surface and bottom pressures in Pa, $\rho(z, t)$ the density as a function of depth and time and $\rho_{ref}(z)$ a reference density calculated for $T = 0 \text{ }^\circ\text{C}$ and $S = 35$ with variable pressure.

2. Steric height can be defined as a function of thermosteric (η_T) and halosteric (η_S) heights, each of which can be calculated directly from integration of *in situ* profiles (Gill and Niiler, 1973). In the following equations, overhat (e.g. $\hat{\rho}$) indicates averaging over depth while overbar (e.g. \bar{T}) indicates averaging in time, so both overhat and overbar together indicates a depth and time mean (e.g. $\hat{\bar{\alpha}}$) :

$$\eta_{st} = \eta_T + \eta_S + \bar{\eta}_{st} \quad (3.3)$$

Heat content can be defined as :

$$H(t) = \rho_0 C_p \int_{h_2}^{h_1} T(z, t) dz \quad (3.4)$$

with H as heat content, ρ_0 as reference density (here taken as the spatio-temporal mean), C_p as heat capacity of seawater (here taken as $3985 \text{ J kg}^{-1} \text{ K}^{-1}$), h_1 and h_2 the ocean surface and bottom depth in m, $T(z, t)$ as temperature as a function of depth and time. Here we derive thermosteric height from heat content using the following equation :

$$\eta_T(t) = \hat{\bar{\alpha}} \left(\frac{H(t)}{\rho_0 C_p} - \int_{h_2}^{h_1} \bar{T}(z) dz \right) \quad (3.5)$$

with α representing the coefficient of thermal expansion. Overhat and overbar ($\hat{\bar{\alpha}}$) again indicate averaging in depth and time.

Freshwater content can be defined as :

$$F(t) = \int_{h_2}^{h_1} \frac{S_r - S(z, t)}{S_r} dz \quad (3.6)$$

with F as freshwater content, $S(z, t)$ as salinity as a function of depth and time. As we estimate steric height relative to $T = 0$ °C and $S = 35$, freshwater content is also estimated relative to reference salinity $S_r = 35$. Similar to thermosteric height, we show halosteric height can be determined from freshwater content :

$$\eta_S(t) = \hat{\beta} \left(-F(t)S_r + \int_{h_2}^{h_1} S_r - \bar{S}(z)dz \right) \quad (3.7)$$

with β representing the coefficient of haline contraction. Overhat and overbar ($\hat{\beta}$) again indicate averaging in depth and time.

Applying these equations allows us to compare satellite steric height calculated using Eq.3.1, with *in situ* steric height calculated from EN4 data using Eq.3.2. Thus to avoid confusion, hereafter, quantities will be prefixed by satellite or *in situ* respective to the source of data they are derived from e.g. satellite steric height and *in situ* steric height. Note that, as the satellite steric height is noisier than the *in situ* steric height, a 3-month running mean is used to smooth the data. Consequently, our methods are able to account for seasonal variability but will not resolve higher frequency variability.

To account for the spatial variability in the Barents Sea, the equations are applied point-wise on the grid of the interpolated datasets. The *in situ* steric height is calculated from the surface downwards to each depth layer. *In situ* steric height at each depth layer is then regressed temporally against satellite steric height, and the optimum integration depth (OID, where the regression with satellite steric height was maximised) are first identified (Figure 3.2). The temporal regression at OID is calculated at each grid point. The OID have a strong seasonal dependence that can be divided into a "strong-stratification" season when optimum heat content integration shallows, and "weak-stratification" season when optimum integration depth deepens. A fuller discussion of the roots of this seasonal bias follows in Section 3.3. For validation purposes, the OID is then selected at each grid point with the greatest regression value for each of the two seasons.

As the main study aim is to ascertain whether the satellite data sets are sufficient to monitor BSW heat and freshwater content, we compared estimates of EN4-based heat content, integrated over the seasonally-dependent optimum integration depth, with SST (Figure 3.3). We found very strong correlations between SST and heat content in the Barents that had clear difference between the strong and weak stratification season, and which provided the justification for developing a satellite-based estimate of heat and freshwater content. Our methods are as follows :

3. A statistical model to determine heat content from SST for each of the "strong-stratification" and "weak-stratification" seasons is derived. Linear regressions are calculated using least-squares regression of monthly data with significance estimated at the 99%-level using a 2-tailed Student's t-test.

In summary, to model heat content from SST, regressions are calculated between heat content and SST for the strong and weak-stratification seasons at each grid point. The OSTIA SST and EN4 heat content datasets are split into the same seasonal groups as the steric height regression models. The heat content is calculated over the season-specific upper layer depth ranges found from the steric height regression. The SST-derived heat content for the two seasons can then be recombined for full temporal coverage. The sea-ice-covered season is not treated separately because this is accounted for in the dataset where SST is set to -1.8 under sea ice. For comparison, we perform the same method with seasonally-varying integration depth to produce a SSS-to-freshwater-content model using EN4 freshwater content and SSS from the top layer (0 to 10 m depth) in EN4.

In the following section, we evaluate these methods of using satellite parameters to estimate water column properties, with the aim of providing a way to monitoring the water masses in the Barents Sea.

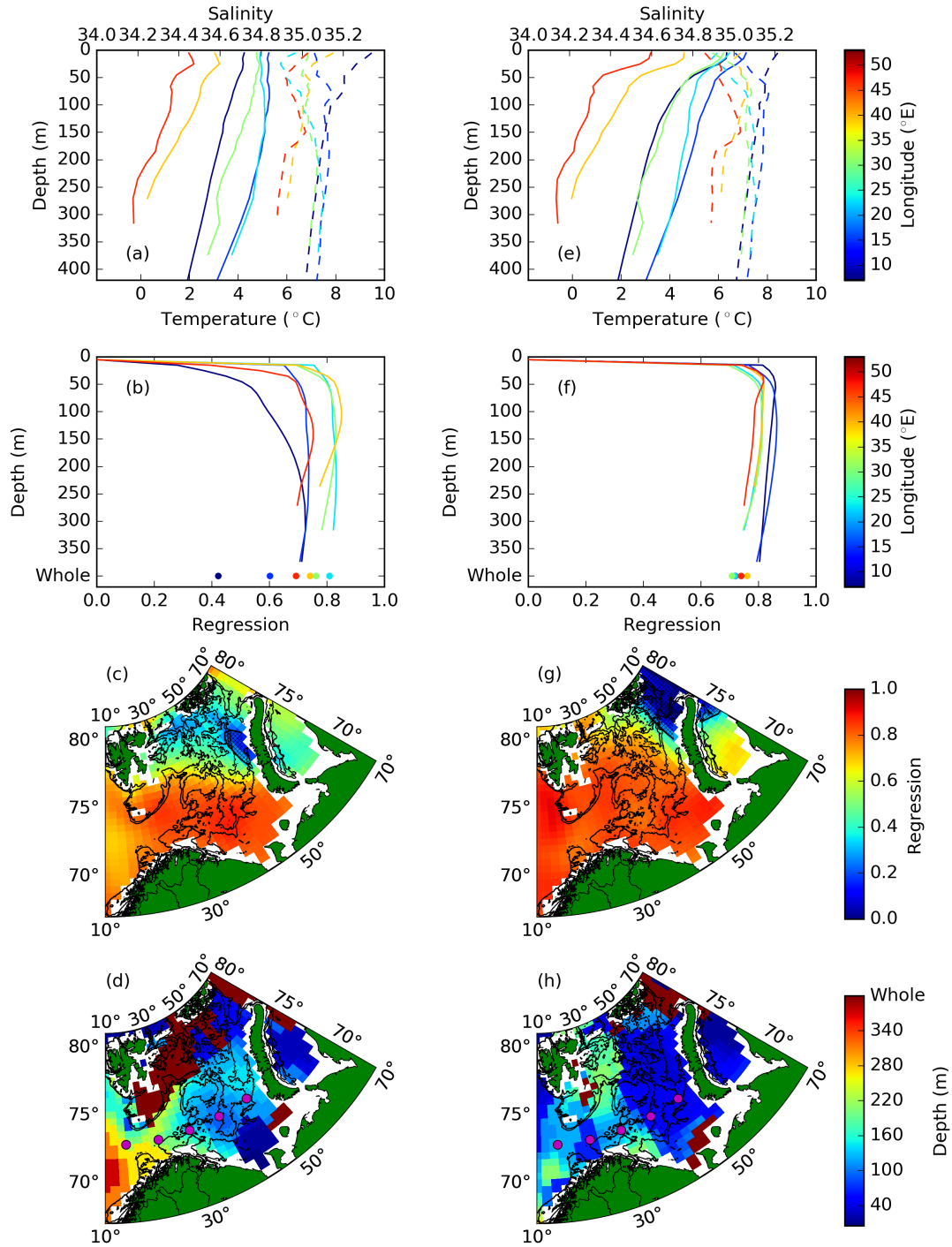


FIGURE 3.2 – (a) Climatology T-S profiles from EN4 for winter (October to March). Solid line is temperature, dashed line is salinity. The colour shows the location of the profile along the purple dots at 72.5° N shown in (d). The 72.5° N profiles are an example of the transition from AW to BSW. (b) Regression of satellite steric height with EN4 steric height between various integration depths to the surface for winter (October to March). The colour shows the location of the profile along the purple dots at 72.5° N shown in (d). (c) Regression of satellite steric height with EN4 *in situ* steric height between optimum integration depth (OID) to the surface for winter. Hatching shows areas with significance < 99%. (d) Spatially varying OID used in (c). The depth 'Whole' on axes refers to integration over the whole water column. White, coastal areas show where data is not available. (e), (f), (g) and (h) are the same as (a), (b), (c) and (d) but for summer (April to September). Black lines show the 220 and 300 m isobaths.

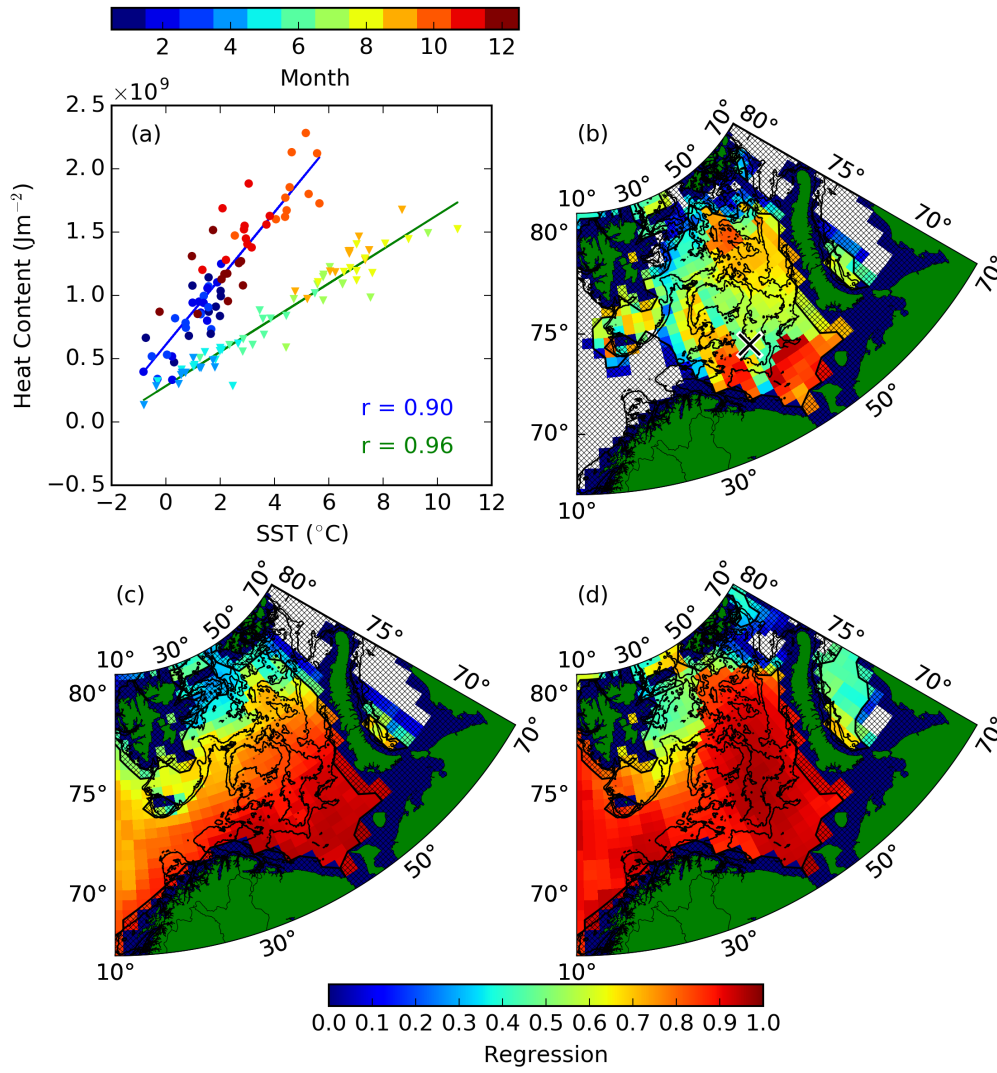


FIGURE 3.3 – (a) Regression of satellite SST with EN4 *in situ* heat content at a single point in the Barents Sea, marked with a black cross in (b). Satellite SST is regressed against EN4 *in situ* heat content calculated to the optimum integration depths (OID) shown in Figure 3.2c,f. Blue line and circles show winter season, green line and triangles show strong stratification season. Regression of satellite SST with EN4 *in situ* OID heat content using (b) a one model system, (c) the winter model (October to March) and (d) the summer model (April to September). Hatching on maps shows areas with significance $< 99\%$. Black lines shows the 220 and 300 m isobaths.

3.3 Estimation of the BSW properties from satellite datasets

In this section we begin our discussion by reviewing the distribution of steric height, freshwater and heat content in the Barents Sea. We then discuss the nuances of applying the methods outlined in the previous section to calculate satellite steric height, and show how these methods perform by comparing them with ground-truthed estimates. This analysis focuses on the Central Basin where BSW is formed but we maintain a contextual view of the wider Barents Sea.

Several water masses exist in the Barents Sea, with temperature and salinity decreasing from south west to north east, each with variable impact on steric height. To quantify these spatial changes we calculate *in situ* EN4 steric height using Eq.3.2 integrated over the whole water column (Figure 3.1). At the entrance of the Barents Sea at 19° E where the water column is entirely composed of AW, steric height is on average 0.2 m, heat content is $0.9 \times 10^{10} \text{ J m}^{-2}$ and freshwater content is 0 m because the salinity of AW is around the reference salinity of 35 (Figure 3.1a-c). Within the south western Barents Sea mean heat content and steric height

decrease to minima of 0.03 m and $0.2 \times 10^{10} \text{ J m}^{-2}$ at 40° E in the Central Basin. Mean heat content remains around $0.2 \times 10^{10} \text{ J m}^{-2}$ both northward and eastward of the Central Basin but mean freshwater content increases from 0 m in the Central Basin to 3 m in the northern Barents Sea.

The temporal standard deviation of monthly mean *in situ* steric height in the Barents Sea varies spatially between 0.01 and 0.03 m (Figure 3.1). This is smaller than the annual cycle amplitude of satellite steric height identified as varying between 0.06 m and 0.01 m by Volkov et al. (2013). Both the lowest standard deviation and the smallest mean steric height are found in the eastern Barents Sea. In the south western Barents Sea, the standard deviation in both *in situ* steric and thermosteric height is ~ 0.025 m, while the standard deviation in the *in situ* halosteric contribution to steric height is ~ 0.01 m. These are comparable to the results of Volkov et al. (2013), who found the amplitude of thermosteric height as 0.012 m and halosteric height as 0.006 m in the Barents Sea for 1980 to 1995. In the Central Basin, the standard deviation in *in situ* thermosteric height decreases to 0.02 m while the standard deviation in *in situ* halosteric height increases to 0.015 m, showing that the standard deviation in *in situ* steric height arises almost equally from variability in *in situ* freshwater and heat content. These results agree with Volkov et al. (2013). In the northern Barents Sea, the standard deviation in *in situ* thermosteric height is 0.01 m but both the *in situ* steric and halosteric standard deviations are ~ 0.02 m, confirming that the variability in *in situ* freshwater content contributes more to the variability in *in situ* steric height, than variations in *in situ* heat content, as expected for the salinity-stratified northern Barents Sea. These results are consistent with Figure 3.1e,f and the results of Stewart and Haine (2016) who showed the Barents Sea as a region where vertical instability could occur in transition from temperature to salinity stratification.

Satellite-based estimates of steric height, thermosteric height and halosteric height are computed by applying the methods of Section 3.2.2. For conciseness of presentation, we use a single location in the Central Basin (shown by the black cross in Figure 3.3b, where variations of the steric height at that location are highly correlated within the wider Central Basin (not shown)) as an example for illustrating model skill. The satellite SSH and eustatic height data at this location show high frequency variability (Figure 3.4a). Integrating from surface to bottom should theoretically produce the satellite observed steric height but our analysis shows this is not always the case, and our initial calculation of satellite steric height produces a result that overestimates the *in situ* steric height (red lines Figure 3.4b). Part of this overestimation arises from a seasonal bias. Indeed, the climatologies of satellite and *in situ* steric height have different timing in their seasonal cycle. The difference is caused by the October peak in *in situ* steric height which occurs when the surface mixed layer peak is eroding and the steric height of the deeper water column is increasing (not shown). The satellite steric height seasonal cycle peaks in September and decreases in October (Figure 3.5). Part of this bias could also come from a time lag artefact in EN4 introduced during reconstructing the fields.

Thus, in order to account for the difference in steric height climatology, we split the dataset into two seasons : a strong-stratification season (summer, April to September) and a weak-stratification one (winter, October to March). According to Loeng (1991), summer mixed layer depth in the AW region of the Barents Sea reaches 60 m and mixes downward in winter, homogenizing to 200-300 m depth, while mixed layers influenced by ArW reach 20 m in summer and mixes down to 150 m in winter. EN4 data shows similar seasonally-varying depths for stratification. In addition, the mixed layer in the Central Basin (where BSW is found) estimated from EN4 is ~ 50 m in summer and ~ 150 m in winter. This means that the variability in steric height is expected to be representative of a larger depth range of the water column during the weak-stratification season than during the strong-stratification season, when the deeper part of the water column is isolated from direct surface interaction. Splitting the datasets between these two seasons is an appropriate compromise between improving the model with known physical processes and not biasing the satellite data to the scarce *in situ* winter data which is regularly based on < 3 profiles in the Central Basin.

Having split the data according to season, the satellite steric height is regressed against *in situ*

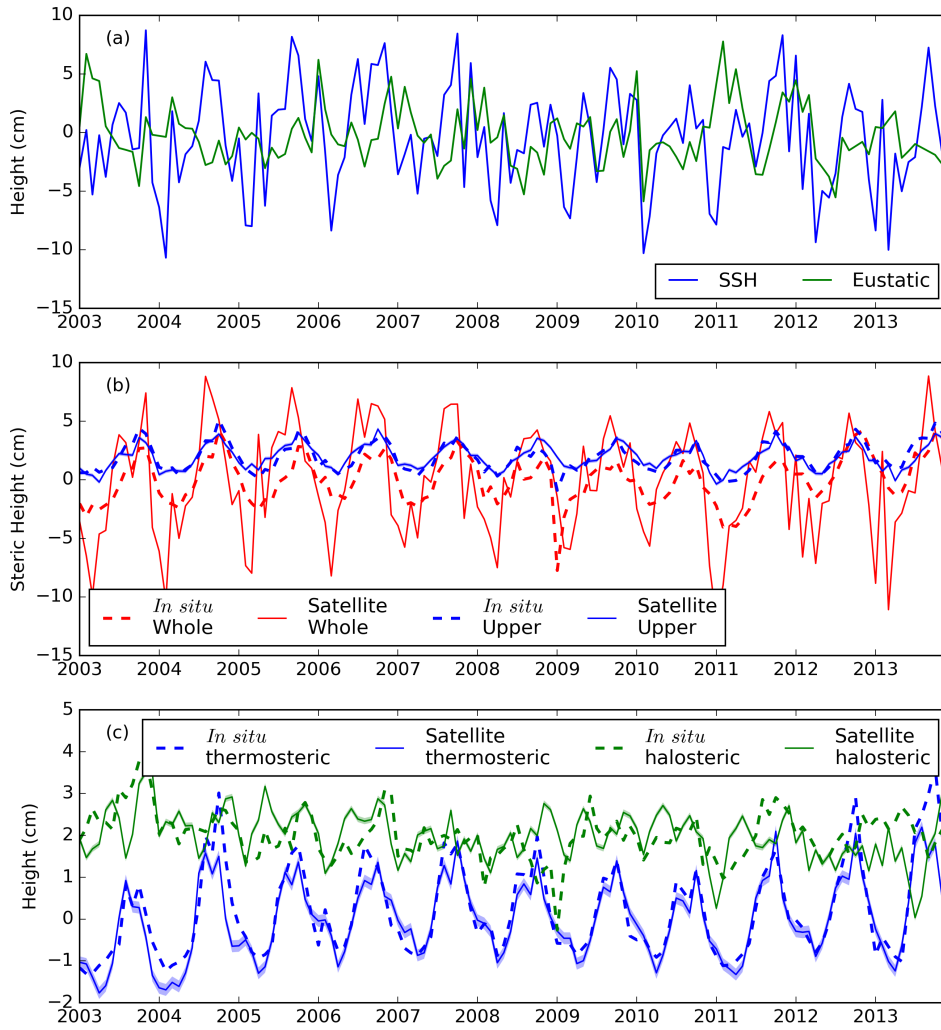


FIGURE 3.4 – Time series at the point marked with a black cross on Figure 3.3b of SSH and GRACE eustatic height (a), EN4 *in situ* steric height integrated between the surface and bottom (b, thick red line), EN4 *in situ* steric height for the upper water column indicated by the integration depths in Figure 3.2d,h (b, thick blue line), satellite steric height for the whole water column (b, thin red line) and satellite OID steric height smoothed with a 3-month running mean (b, thin blue line). *In situ* OID thermosteric and halosteric heights estimated for the upper water column, and satellite OID thermosteric and halosteric heights for the same depth range (c, note that the halosteric height has been offset by 0.02 m). Standard error bars are shown by shading.

steric height calculated between the surface and a range of integration depths (Figure 3.2a,d). The regression of satellite and *in situ* steric height changes from West to East depending on depth range over which *in situ* steric height is integrated. The depth with largest r -value referred to here as the optimum integration depth (OID) and is significant because this probably represents the depth over which water mass transformation is occurring within each season. However, the OID and mixed layer depths are not the same given the mixed layer depth evolves over the summer and winter seasons while we only use one integration depth per season. The OID during weak-stratification shoals eastwards from >250 m in the western Barents Sea to 120 m in the Central Basin (Figure 3.2c). The shallower OID in the Central Basin is similar to the depth where "doming" of pycnoclines were observed by Ozhigin et al. (2000); Schauer et al. (2002), which is likely a signature of the ventilation of isopycnals and the formation of deep water. These OID are similar to the mixed layer depths found in the model analysis by Aksenov et al. (2010). During the strong-stratification season, OID ranges between 50 and 150 m across the south and

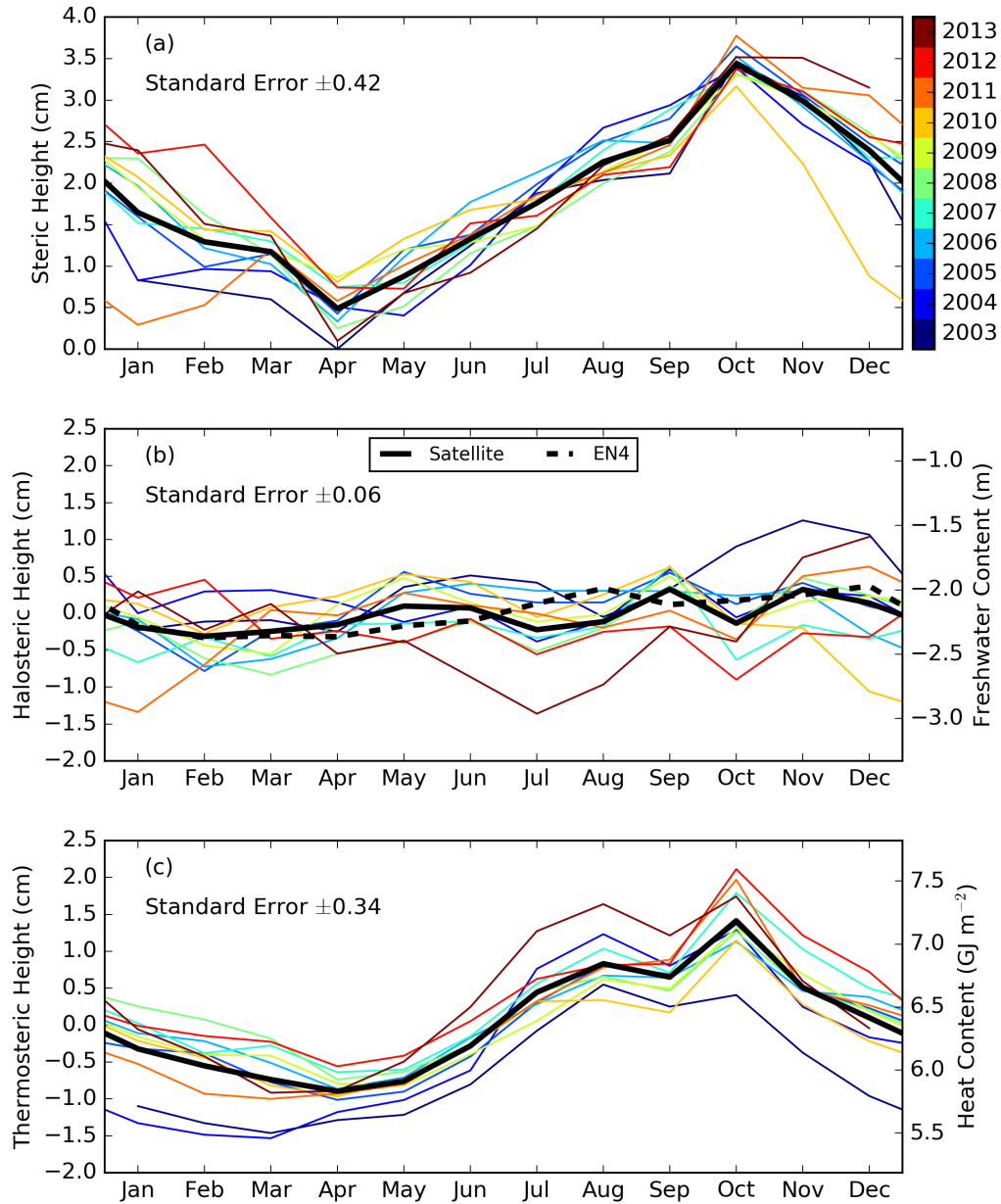


FIGURE 3.5 – Mean seasonal cycle (thick line) and interannual variability (colours indicate individual years) of satellite OID steric height (a), satellite OID halosteric height (b) and satellite OID thermosteric height (c) averaged over the Central Box (purple box in Figure 3.1). (b) Dashed line shows *in situ* OID halosteric height climatology. Standard error for the interannual variability in the seasonal cycle is shown.

eastern Barents Sea (Figure 3.2e). Across the southern Barents Sea, both seasonal regressions between *in situ* OID and satellite OID steric height are around 0.8, while in the northern Barents Sea the regression drops to around 0.4 during the weak stratification season (Figure 3.2b,e). The seasonal sea ice cover in the north results in a very limited number of profiles during winter and spring, so that EN4 only reflects the long term seasonal climatology in this region during winter and spring. This explains the lower regression values between *in situ* OID and satellite OID steric height measurements found in this region. It is possible that the regression could be improved further but in this study we have stuck with our bi-seasonal approach to avoid over-fitting to imperfections in EN4.

It is important to estimate the uncertainty of the satellite OID steric height to determine the quality of the measurement and how far they may deviate from the true value. The uncertainty of satellite OID steric height can be estimated using the uncertainties of the component datasets, OPB and SSH. The formula for quadrature propagation applied to Eq. 3.1 means the uncertainty can be estimated as $\Delta_{\eta_{st}} = \sqrt{\Delta_{\eta_H}^2 + \Delta_{\eta_m}^2}$ where Δ is the respective uncertainty. The uncertainty of our satellite OID steric height is 1.6 cm, comparable to the 1.9 cm uncertainty of [Armitage et al. \(2016\)](#). The 1.6 cm uncertainty is then propagated with the regression model for the mixed layer satellite OID steric height as $\Delta_{mixed\eta_{st}} = \sqrt{m\Delta_{\eta_{st}}^2}$ where m is the regression model gradient. This gives a final conservative estimate of 1 cm uncertainty in satellite OID steric height across the Barents Sea.

The determination to the water column properties from surface satellite observations requires a robust statistical relationship between SST and heat content, similar to that proposed from model analysis by [Lique and Steele \(2013\)](#). In order to infer heat content from SST, we combine two statistical models corresponding to our strong-stratification and weak-stratification seasons, determined by regressing *in situ* OID heat content against SST for each grid point. Figure 3.3a show how the SST and OID heat content gradually increase through the summer, from April to September. This is caused by a net gain in ocean heat from radiation and heat advection ([Smedsrud et al., 2010](#)). At our illustrative location, SST decreases between September and October, but the OID heat content increases (Figure 3.3a). In October, the net surface heat flux is out of the ocean ([Ding et al., 2016](#); [Smedsrud et al., 2010](#)) and SST is reduced while the surface mixed layer is expected to deepen ([Kantha and Clayson, 1994](#); [Loeng, 1991](#)). The extent of this deepening will be dependant on many factors including whether the underlying stratification is temperature or salinity driven. In our example location, the increase in OID heat content between September and October cannot be driven by local surface fluxes because the total surface heat flux is out of the ocean over this time ([Smedsrud et al., 2010](#)), suggesting that advection of warmer water explains this increase (Figure 3.3a). From October to March, SST declines linearly with OID heat content. Given the 0.57 K uncertainty associated with the OSTIA SST product, we estimate that the associated uncertainty for the OID heat content resulting from our statistical model with satellite SST. The SST uncertainty is propagated with the regression gradient for OID heat content (similar to the satellite OID steric height uncertainty) to give an uncertainty in heat content of $4 \times 10^8 \text{ Jm}^{-2}$.

Figure 3.3b-d shows how effective the regression models are in a spatial context. Both the strong and weak-stratification models have greater regression values than a single regression model. The strong and weak-stratification regression models shows r-values greater than 0.8 throughout the southern Barents Sea and greater than 0.9 in the Central Basin. In the northern Barents Sea the weak-stratification model is less effective, with regression values closer to 0.6 (Figure 3.3c). The SST-to-heat-content model differs from the steric height regression in regions with seasonal sea ice. The northern Barents Sea is seasonally sea ice covered during which SST is relatively constant at -1.8°C (although the date of the onset of freeze and melt may vary from year to year), making SST less representative of the heat content here.

The same method can be applied to derive a statistical model estimating freshwater content from SSS. Here, we consider SSS as the first depth bin (0 to 10 m depth) of the EN4 salinity field. Ideally this analysis would have been carried out with satellite SSS instead of EN4 data but there is only a short period of overlap with our observation period. Indeed, the Soil Moisture and Ocean Salinity (SMOS) satellite was launched in late 2009 and the Aquarius mission (later continued to the Soil Moisture Active Passive (SMAP) mission) making SSS measurements was launched in August 2011. Moreover, retrieving SSS from L-band measurements at high latitudes (i.e. in cold water) is known to be particularly challenging ([Olmedo et al., 2018](#)). A quick comparison between the EN4 SSS and the different satellite SSS products during their respective overlapping periods indeed reveals that while the mean spatial patterns are similar in sea ice-free regions, satellite SSS products are unable to reproduce the temporal variability found in EN4 SSS (not shown). The SSS-to-freshwater-content model at our illustrative location shows a smaller difference between the strong and weak-stratification seasons and less dependence on the

month considered than the SST-to-heat content model (Figure 3.6a). SSS is a good predictor of the EN4 OID freshwater content, with regression values around -0.9 at the 99% significance-level across the northern and eastern Barents Sea in the strong-stratification season (Figure 3.6b-d). The weak-stratification season has regression values between 0.5 and 0.9, with the greater values found in the western Barents Sea. We acknowledge that a better SSS-to-freshwater content fit is expected as we consider here only comparison within one dataset (EN4) in contrast to the SST-to-heat content model for which data from independent sources were considered. Yet, assuming future improvements in the SMOS and SMAP SSS retrieval in the Barents Sea, our analysis could be used to expand the satellite SSS record over a longer period. In addition, by inverting the equations for *in situ* thermosteric and halosteric height we calculate a satellite based T-S profile (detailed in the Supplement A).

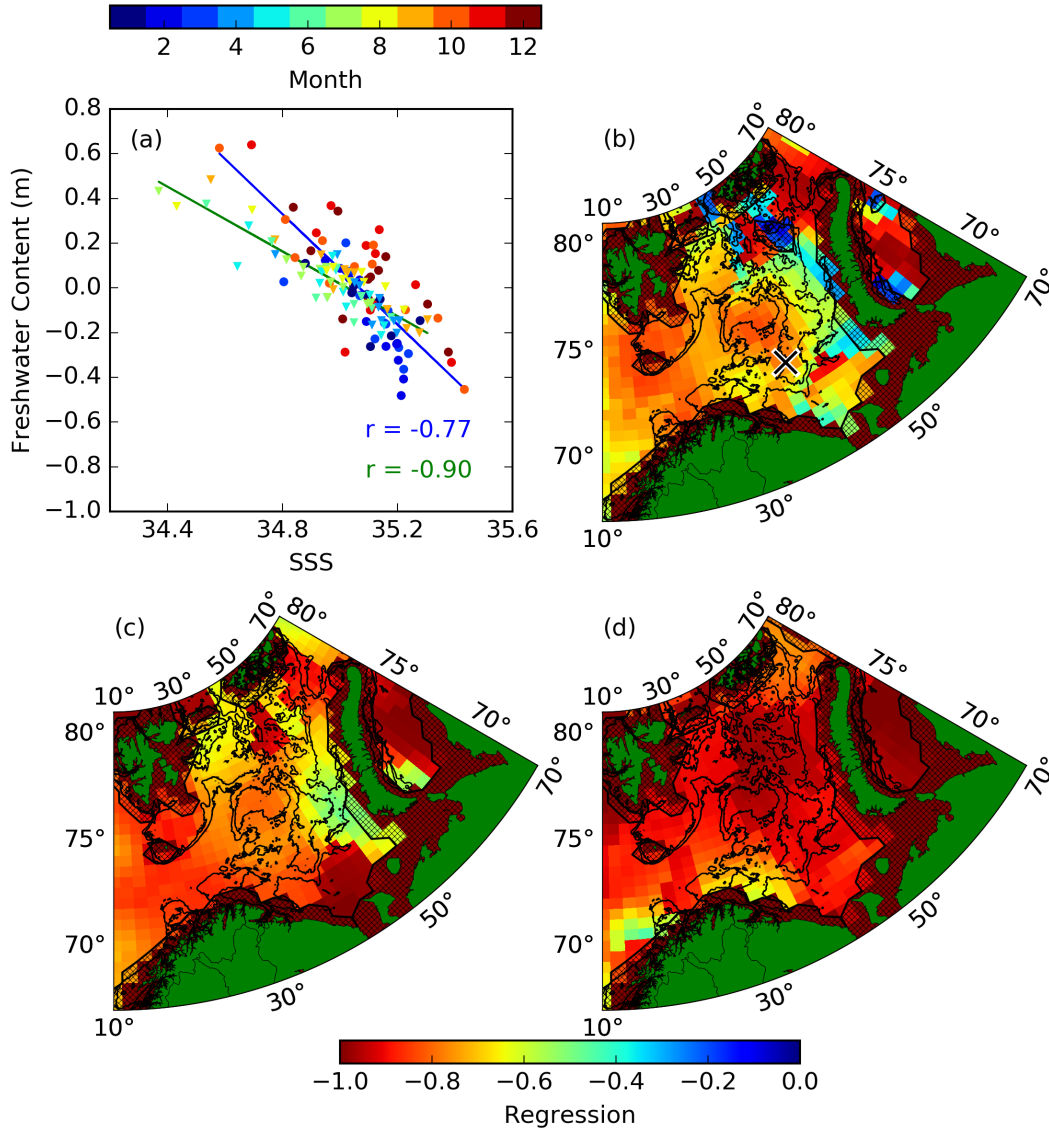


FIGURE 3.6 – Same as Figure 3.3 but for *in situ* SSS and *in situ* OID freshwater content.

The satellite OID steric height is representative of an upper fraction of the water column (Figure 3.4b). Using satellite OID steric height and satellite OID thermosteric height estimated heat content with Eq. 3.5, we use Eq. 3.3 to calculate the halosteric height (the reconstruction for our example location is shown in Figure 3.4c). The ability of the satellite OID model to retrieve an accurate halosteric height time series is significant, with regression values with the EN4 halosteric height between 0.4 and 0.55 in the Barents Sea (significant at the 99%-level) (Figure 3.7). It should be noted that there are only a few EN4 profiles in the Kara Sea so regression values

here only represent the climatology. When heat content is converted to thermosteric height, thermosteric height has an uncertainty of 1.1 cm. Using quadrature uncertainty propagation of the satellite OID steric height and thermosteric height, the uncertainty of the estimated satellite OID halosteric height is 1.5 cm and the uncertainty of satellite OID freshwater content is 0.6 m. For this study we consider that the gridded EN4 dataset does capture the variations of the water mass properties, but it is worth noting that the irregular sampling, particularly during winter and spring, means temporal inaccuracies are inevitable. Individual T - S profile used in producing the gridded EN4 product can also be biased by mesoscale features that are not resolved in the satellite OID data. Figure 3.7 suggests no significant regression between satellite OID and *in situ* OID halosteric height in the Norwegian Sea. We speculate that this was caused by a larger thermosteric contribution inducing a weak correspondence between steric height and the halosteric contribution, as shown by the standard deviation in Figure 3.1c,f.

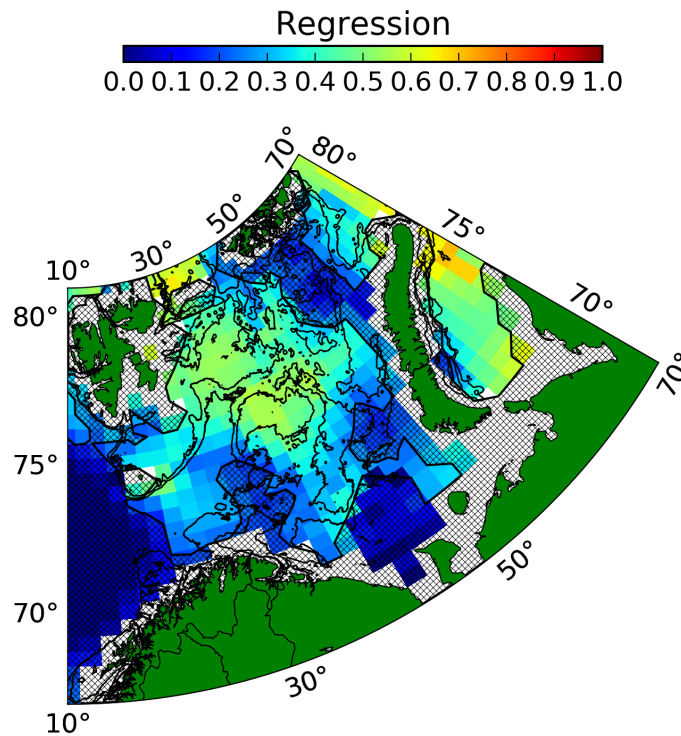


FIGURE 3.7 – Regression of satellite optimum integration depths (OID) halosteric height with EN4 *in situ* OID halosteric height. Hatching shows areas with significance < 99%. White, coastal areas show where data is not available due to limitations of GRACE data. Black lines shows the 220 and 300 m isobaths.

The satellite OID steric, thermosteric and halosteric heights produced in this Section following our first aim, comes with some inherent limitations. The satellite OID thermosteric high has fewer limitations than satellite OID steric and halosteric since it is based on SST alone. The feature resolution of the satellite OID thermosteric height is expected to be of similar spatial scale to the EN4, the temporal scale is seasonal. The steric height and halosteric height are both limited but the spatial feature resolution of GRACE which has 500 km low pass filter. The feature resolution of these two products is therefore 500 km and temporal resolution is monthly. The EN4 profiles necessarily have irregular spatial and temporal resolution and, once ground-truthed, the satellite-based analysis allow us to fill in the gaps. The satellite data has lower accuracy than EN4 and does not offer information on vertical structure. The satellite datasets give information on the OID and assumes a seasonally dependant OID depth for each location, depth range experiencing seasonal water mass transformation. These data should be used as complementary to EN4 or other profile datasets. Results show the potential for freshwater content derivation in this region

from future improvements in satellite SSS.

3.4 Understanding the variability of BSW

Now that we have demonstrated skill in retrieving satellite-based OID steric, thermosteric and halosteric heights, in this section we address the second aim of our study by exploring the seasonal and interannual variability in these quantities in detail. The Central Basin, which has been suggested as the BSW formation region (Oziel et al., 2016; Loeng, 1991), now becomes our focus.

Given that both the satellite OID thermosteric and halosteric height are auto-correlated within the Central Basin, all values are averaged within a representative box defined by 35 °E to 47 °E and 71 °N to 76 °N (~400 by 550 km box, see box on Figure 3.7). This box lies between the Polar Front at 76.5 °N, the Barents Sea Front at ~35 °E and the Coastal Water Front that roughly runs along 71 °N between 33 and 50 °E and along 50 °E between 72 and 76 °N (Barton et al., 2018; Oziel et al., 2016). Given that the Central Basin has previously been identified as a convective BSW formation site in model analysis (Aksenov et al., 2010), we consider that the quantities averaged within this box are indicative of the BSW properties. Note that all ERA-Interim atmospheric fluxes presented here are also averaged within this box, but the sea-ice cover refers to the whole Barents Sea as our box was ice-free from 2005 onwards (Barton et al., 2018). Even though sea ice is not present, the melt water can still be advected into the box so this provides useful context to the observed properties.

There is a pronounced seasonal cycle in the satellite OID steric height, with a maximum in October and a minimum in April (Figure 3.5). In our Central Basin box, the timing of the summer and winter extrema of the satellite OID steric height corresponds to the seasonal variability in thermosteric height (see Section 3.3, Figure 3.3).

An examination of the interannual variability in satellite OID steric height reveals a shift in the seasonal cycle over time (Figure 3.5). August and September steric height declines over time, while November to March steric height increases over time. The reduction in summer steric height also appears in the halosteric height suggesting this could be the main cause. The winter increase in satellite OID steric height is likely due to a combination of interannual variability in thermosteric and halosteric heights. These contribute the interannual trend of increasing satellite OID steric height significant at the 99% level. The trend in winter satellite OID thermosteric is consistent with increasing winter SST (Jakowczyk and Stramska, 2014). An increase in winter satellite OID steric height suggests a decrease in BSW density during the same period. This is inconsistent with the increase in density of the BSW found in the subsurface documented by Barton et al. (2018), however, the satellite OID steric height signal found here only represents part of the BSW volume that is found in the surface layer in the central Barents Sea unlike Barton et al. (2018) who quantified changes in the BSW outflow to the north.

The variability in satellite OID halosteric height in the central Barents Sea is dominated by interannual variability, with only a weak seasonal cycle and an overall trend of decreasing freshwater content (Figure 3.5, 3.8). The range of the weak seasonal cycle in satellite OID halosteric height is comparable to the estimated uncertainty value. Interannual variability is stronger so we focus on this.

The surface freshwater flux includes evaporation, precipitation and sea ice melt-freeze. In the ice-free central Barents Sea, winter evaporation outweighs precipitation, and the net precipitation in summer is due to reduced evaporation (Figure 3.9b). Although counterintuitive at first glance, the seasonal cycle in Barents Sea evaporation is consistent with evaporation being greatest during the winter when the air-sea temperature difference is greatest. Our estimates of atmospheric freshwater flux are similar to the 0.9 mm day⁻¹ found by Walsh et al. (1998) when averaged over a year, although these are larger than the ± 0.6 mm day⁻¹ estimated by Segtnan et al. (2011). Over this short timeseries there is an increasing trend in precipitation significant at 99% level. This may be decadal variability but future climate models predict increasing rainfall over the Arctic (Bintanja and Andry, 2017). Although, between 1951 and 1992 precipitation appeared to

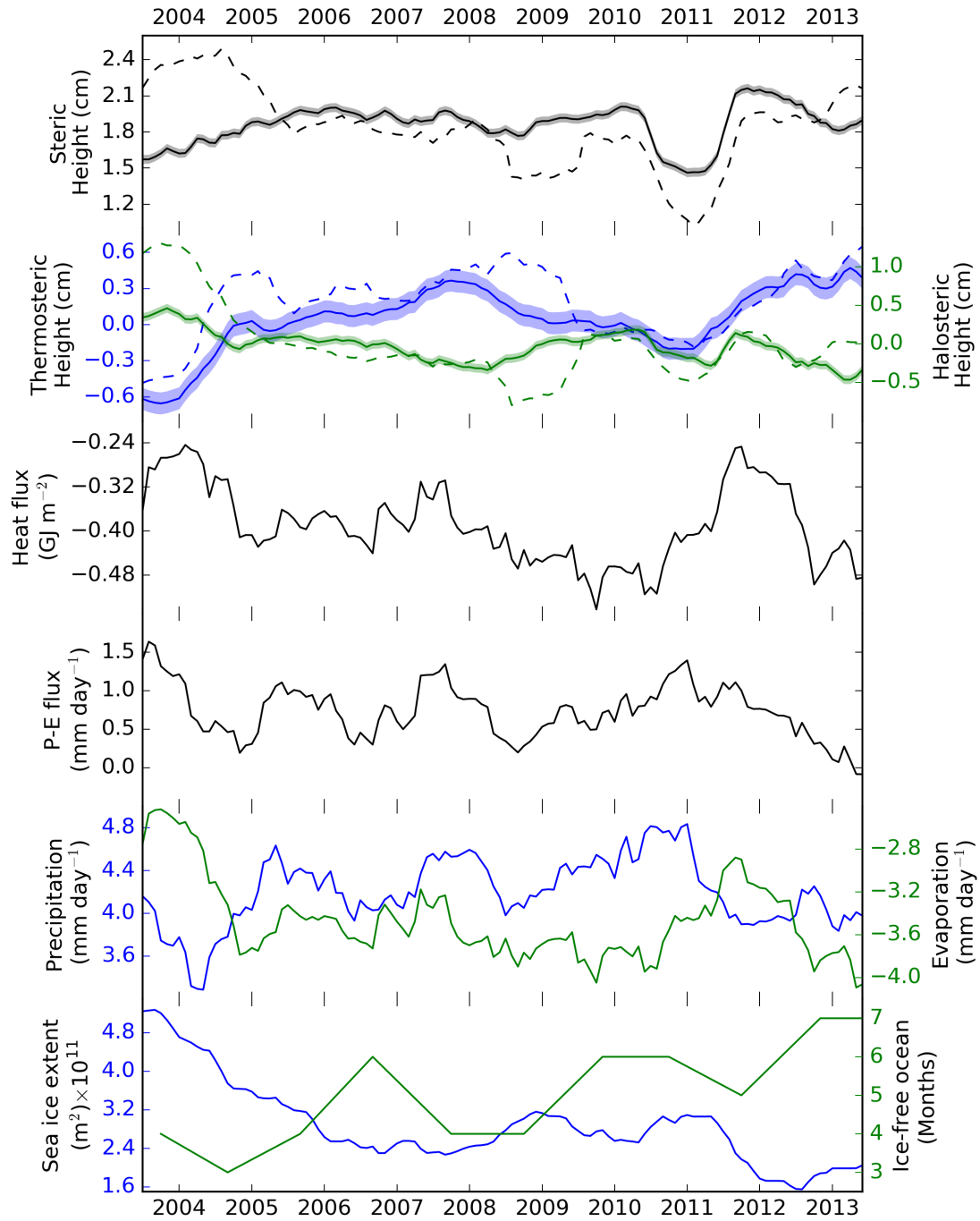


FIGURE 3.8 – Time series of the OID properties used to infer BSW property variability from satellite (solid line) and *in situ* observations (dashed line), heat flux, precipitation, evaporation and precipitation minus evaporation (P-E), averaged over the Central Basin and calculated with 12-month running mean. The time series are averaged over the Central Box (purple box in Figure 3.1). Standard error bars on the satellite OID data are shown by shading. The time series of the sea ice extent is averaged over the whole Barents Sea (68 °N to 80 °N and 10 °E to 65 °E), and is shown along with months of ice-free ocean defined by the time difference between the month with maximum melt (decrease in sea ice extent) and the month with maximum freeze (increase in sea ice extent).

be in decline around the north eastern Barents and Kara Seas (Aleksandrov et al., 2005). The trend in precipitation is more than compensated by the negative trend in evaporation resulting in

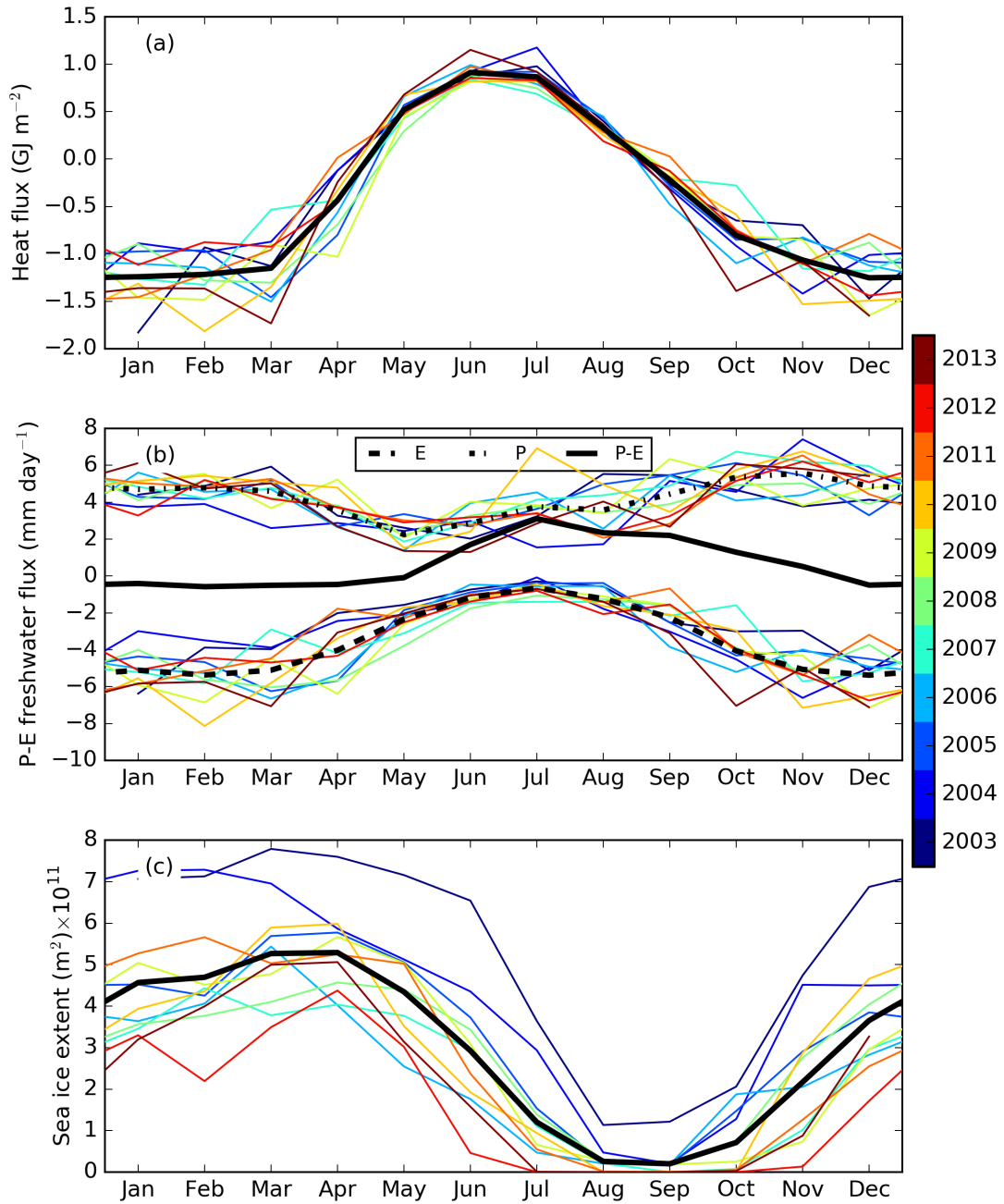


FIGURE 3.9 – Same as Figure 3.5 but for heat flux (a). Precipitation (P), evaporation (E) and precipitation minus evaporation (P-E) are presented on (b) where positive is into the ocean. Sea ice extent is shown on (c). Note that sea ice extent is integrated over the whole Barents Sea (68°N to 80°N and 10°E to 65°E).

an overall negative trend in freshwater flux significant at 99% level. At the interannual time scale atmospheric freshwater flux is not strong enough to cause interannual variability in halosteric height.

The satellite OID halosteric interannual variability mirrors the satellite OID thermosteric interannual variability (Figure 3.8). Similar variability between temperature and salinity is noted between 1970 and 2000 at the Kharlov and Kanin sections in the Central Basin (Ozhigin et al., 2000). This is a feature observed northward from 59°N along the coast of Norway, and may

reflect the variability in mixing between relatively cool and fresh Norwegian Coastal Current water and relatively warm and salty AW (Yashayaev and Seidov, 2015). It may also reflect the influence of greater heat content reducing sea ice extent which would reduce freshwater input from melting. Satellite OID halosteric height exhibits a significant (at 99% level) decline over the study period (Figure 3.8). This trend may be part of decadal variability but is consistent with changes in sea ice. While the winter maximum sea ice extent is stable after 2005, the sea ice melt season begins earlier over our time period, concluding in July 2012/13 instead of August and increasing the sea-ice-free time from 3 months to 7 months (Figure 3.8). The resulting long-term trend in decreasing sea-ice extent is significant at 99% level and clearly seen in the annual means (Figure 3.8). This is consistent with the atlantification of the Barents Sea, which is believed to be driven by increasing salinity of the AW inflow and decreased freshwater from sea ice (Barton et al., 2018), that may also be abetted by a significant at 99% level downwards trend in atmospheric heat flux (Figure 3.8 Aleksandrov et al. (2005)). Lind et al. (2018) showed that part of the atlantification process is declining sea ice imports to the Barents Sea, which drives a major freshwater loss and weakened ocean stratification in the salinity-stratified northern Barents Sea. The ability to make observations of freshwater content from satellite is timely given the wider observations of changing sea ice and freshwater content in the Arctic Ocean and its importance for maintaining halocline stratification (Morison et al., 2012; Polyakov et al., 2017, 2018; Onarheim and Årthun, 2017).

Satellite OID thermosteric height is key to determining the seasonal cycle in satellite OID steric height, and exhibits a trend towards overall higher OID heat content significant at 99% level, in the central Barents Sea during the study period (Figure 3.5, 3.8). The interannual variability in satellite OID thermosteric height between 2003 and 2009 is consistent with the variability found in temperature observations by Boitsov et al. (2012). Satellite OID thermosteric height is expected to respond to atmospheric heat flux into the ocean, which shows a clear seasonal cycle peaking in June but with low interannual variability (Figure 3.9). The offset in peak satellite OID thermosteric height in autumn (Figure 3.5c) relative to the peak mid-summer atmospheric heat flux (Figure 3.9a) is entirely consistent with the ocean accumulation of heat throughout the summer. This is caused by a net gain in ocean heat from radiation and heat advection (Smedsrud et al., 2010). In our example location in Figure 3.3a, the increase in *in situ* OID heat content between September and October cannot be driven by local surface fluxes because the total surface heat flux is from the ocean to the atmosphere over this time (Smedsrud et al., 2010) (Figure 3.9a). Between September and October, SST is decreasing (Figure 3.3a) and the surface mixed layer is expected to deepen (Kantha and Clayson, 1994; Loeng, 1991), suggesting that advection of warmer water explains the increase in heat content (Figure 3.3a). The range in seasonal atmospheric heat flux is -1.25 to 1 GJ m^{-2} . This is larger than the 5.75 to 7.25 GJ m^{-2} range in satellite OID heat content (Figure 3.5c). The slightly larger atmospheric heat budget is likely a result of our heat content in the summer season being calculated over a smaller depth range than in the winter season. The atmospheric heat flux also shows more heat is lost in the winter than is gained in the summer and must therefore be balanced by the heat transport, as suggested by Smedsrud et al. (2010).

3.5 Conclusion

Heat content variability in the Barents Sea is a useful predictor for sea ice extent (Lind et al., 2018; Onarheim et al., 2015; Årthun and Eldevik, 2016), and thus an important quantity to accurately monitor but difficult to achieve with high temporal and spatial resolution *in situ*. Our analysis suggests that it is possible to combine OBP, SSH and SST satellite data to determine monthly time series of satellite upper-ocean OID steric height, heat and freshwater content for major parts of the southern Barents Sea. This builds on Volkov et al. (2013)’s analysis of steric height, thermosteric and helosteric height using satellite data. These satellite measurements are regressed with *in situ* OID data but ultimately have independent variability. In addition, the satellite data offers regular, higher spatio-temporal coverage that would be costly to obtain with

in *in situ* profiles. The satellite derived data products provide information complementary to the *in situ* data, but cannot give information on the vertical structure of the water column or variability in heat and freshwater content below the upper ocean OID.

The satellite-derived OID steric height and heat content of the Central Basin OID have been used to examine variability indicative of BSW, a water mass that makes up more than 50 % of AIW (Maslowski et al., 2004). The results show the main driver of the seasonal cycle in BSW steric height is variations of the heat content, which arises from a combination of advected heat and atmospheric heat flux. The interannual variability in steric height comes from both heat content and freshwater content. Interannual variability in freshwater content is not found to reflect variability in local E-P fluxes. Instead, the variability, which is small, may be related to variations in AW inflow through the BSO.

While the analysis time period considered here is limited between 2003 and 2013, the datasets could be extended to present day with the recent launch of GRACE-FO. Our method also provides a way to continuously monitoring the freshwater content and salinity in this region. This could help weather prediction due to the Barents Sea influence on atmospheric circulation (Hoshi et al., 2019). Variability in freshwater content in BSW is transported through the Arctic Ocean in AIW (Lique et al., 2010), meaning measurements in the Barents Sea could be used to anticipate variability along this transport pathway. It may be possible to apply these methods in other cold regions where deep water and mode water are formed.

Chapitre 4

Understanding the variability of the Barents Sea Water : a high resolution model study

4.1 Introduction

The Barents Sea experienced a 50% reduction in annual sea ice extent between 1998 and 2008 (Årthun et al., 2012). Over the satellite record from 1979 to present, the summer minimum in sea ice extent has receded, leaving the Barents Sea mostly ice free in summer (Onarheim et al., 2018). The winter maximum in sea ice extent has also declined (Onarheim and Årthun, 2017), following a 2005 distinct regime change in the sea ice and ocean where the sea ice became unable to cross the polar front due to significantly warmer water in the south (Barton et al., 2018). Temperature in the Barents Sea varies on multidecadal timescales with periodicity at 6, 10, 18 and 40 years (Levitus et al., 2009; Venegas and Mysak, 2000; Skagseth, 2008). A long term time series of salinity suggests frequency of variability at 5 and 10 years (Yashayaev and Seidov, 2015; Skagseth, 2008). An ensemble of models show there is a 40 % possibility that this natural variability will cause re-expansion of the lost sea ice cover by 2040 (Arthun et al., 2019). The changes in sea ice here are important because they have been associated with extreme weather patterns in Europe and Asia (Luo et al., 2016; Petoukhov and Semenov, 2010). Although the physics of sea ice induced weather patterns is still an area of active research, on short time scales (days to months) the atmosphere forces the sea ice extent (Gong and Luo, 2017) but longer term variability in sea ice extent comes from the ocean (Hoshi et al., 2019).

TABLE 4.1 – Table of water mass properties used for the observation data and the model output. Observations use standard definition but the model uses updated definitions to account for the 0.1 fresh salinity bias in the model.

Water Mass	Temperature	Salinity	Density
AW Observations	$T > 3^{\circ}C$	$S > 34.8$	
AW Model	$T > 3^{\circ}C$	$S > 34.7$	
BSW Observations	$T < 2^{\circ}C$	$S > 34.7$	$\sigma > 27.85$
BSW Model	$T < 2^{\circ}C$	$S > 34.6$	$\sigma > 27.77$
ArW Observations	$T < 0^{\circ}C$	$S < 34.7$	
ArW Model	$T < 0^{\circ}C$	$S < 34.6$	
CW Observations	$T > 2^{\circ}C$	$S < 34.7$	
CW Model	$T > 2^{\circ}C$	$S < 34.6$	

The Barents Sea has four main water masses present during winter, when the seasonal stratification is eroded, they are Atlantic Water (AW), Barents Sea Water (BSW), and Arctic Water (ArW) and Coastal Water (CW) (see Table 4.1 and Figure 4.1 for the property definitions) (Oziel et al., 2016; Loeng, 1991; Barton et al., 2018). The mean locations of AW, BSW and ArW are shown on Figure 4.2. The AW is advected into the Barents Sea through the southern end of Barents Sea Opening (BSO) between Fugløy, Norway and Bear Island (Ingvaldsen et al., 2004a). Some of this AW recirculates within the western Barents Sea and exits through the northern end of the BSO. The remaining AW is advected eastward into the Central Basin where modified AW is found, known as BSW. BSW is found in observations of the water properties but the formation of BSW from AW is not quantified (Schauer et al., 2002; Loeng, 1991), while in models the transformation is more easily quantified (Årthun et al., 2011; Aksenov et al., 2010). As indicated by the water mass properties, the transformation involves slight freshening from various freshwater sources and cooling through atmospheric heat loss during winter. ArW enters the Barents Sea from the north between Svalbard and Novaya Zemlya forming a salinity stratified layer of relatively fresh water that is present throughout the year in the Northern Barents Sea (Lind et al., 2016). After the BSW (sometimes referred to as Modified AW) has cooled, it flows northward below the ArW exiting the Barents Sea through the Barents Sea Exit (BSX) between Franz-Josef Land and Novaya Zemlya (Gammelsrød et al., 2009). CW is limited to the edges of the southern and eastern Barents Sea, fed by the Norwegian/Murmansk Coastal Current (Skagseth et al., 2011; Harris et al., 1998) and mixing with outflow from the river input along the coasts of Norway and Russia (Dankers and Middelkoop, 2008).

BSW was identified by Loeng (1991) in the Central Basin of the Barents Sea and is a denser

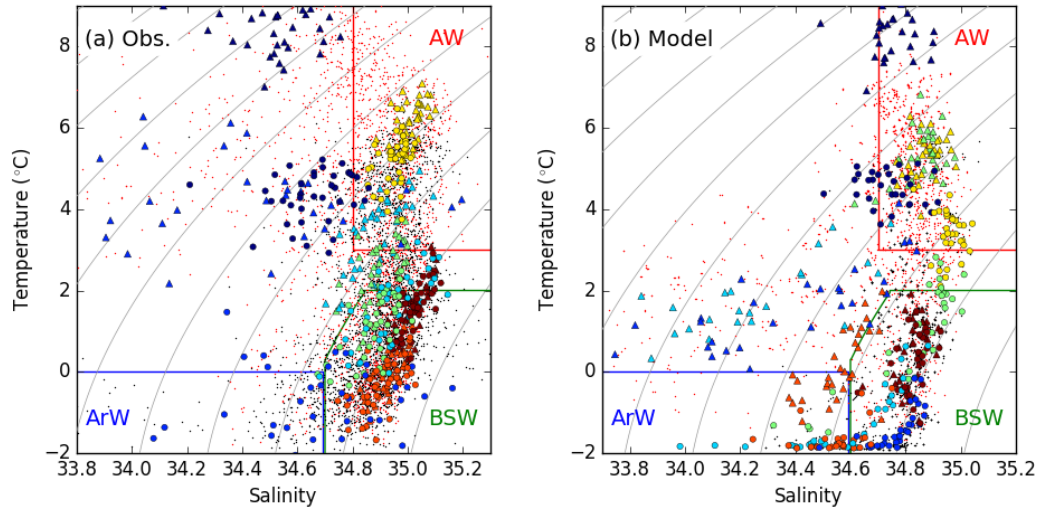


FIGURE 4.1 – T/S diagram showing the relative water mass boundaries. The red box is Atlantic Water (AW), the green box is Barents Sea Water and the blue box is Arctic Water (ArW). (a) shows *in situ* observations from EN4. (b) shows model output from the NEMO model used in this study. The small red and black points are an evenly sampled subset of locations and depths over the time period 1985 to 2015, totalling 60 in the model and 77 in the observations (note they do not correspond to the same locations in model and observations). The larger coloured points are a subset of 7 locations that show the range interannual variability in the properties at the respective location. The triangles and small red points show September properties, the circles and small black points show March properties. Circles and triangles of the same colour represented the same location but the locations are not necessarily consistent between observations and model.

water mass than the AW, ArW and CW around it (Schauer et al., 2002). BSW has been identified in a hydrodynamic model which suggest variability in BSW volume is correlated with sea ice melt water, although no observations confirm that BSW is correctly represented in the model (Oziel et al., 2016). Barton et al. (2018) showed BSW temperature and salinity had increased between 1985-2004 and 2005-2016. In Chapter 3, BSW properties were represented in terms of heat and freshwater content from satellite observations and showed seasonal variability in BSW density was primarily due to heat content but there was similar interannual variability in heat and freshwater content at a 6 year period. BSW is important because it is advected into the Arctic Basin and makes up 50 - 80 % of Arctic Intermediate Water volume (Maslowski et al., 2004; Rudels et al., 2000), before contributing to the deeper branch of Atlantic Meridional Overturning Circulation (Fahrbach et al., 2001; Karcher et al., 2011). Being a major contributor to Arctic Intermediate Water means variability in the properties of BSW can be identified when it exits the Arctic Basin through Fram Strait (Lique et al., 2010).

Fronts are found where water masses meet; AW and BSW are separated by the Barents Sea Front, CW is separated from the others by the Coastal Front and ArW is separated from the others by the Polar Front. The mean position of the fronts are bathymetry constrained (Gawarkiewicz and Plueddemann, 1995). These fronts and their variability are important because, after 2005, winter sea ice was unable to cross south of the northern Polar Front and west of the eastern Coastal Front (Barton et al., 2018). This was suggested to be the result of increasing AW temperature entering the Barents Sea through the BSO. Observations show the regime change in sea ice extent that happened in 2005 resulted in warmer, saltier BSW and ArW (Barton et al., 2018; Lind et al., 2018).

We have identified a gap in the literature where strong variability in BSW properties have been identified but the source of this variability remains unidentified (Barton et al. (2018), Chapter 3). Given the important role this water mass plays in Arctic Intermediate Water, its variability should be quantified and better explained. Barton et al. (2018) suggest the 2005

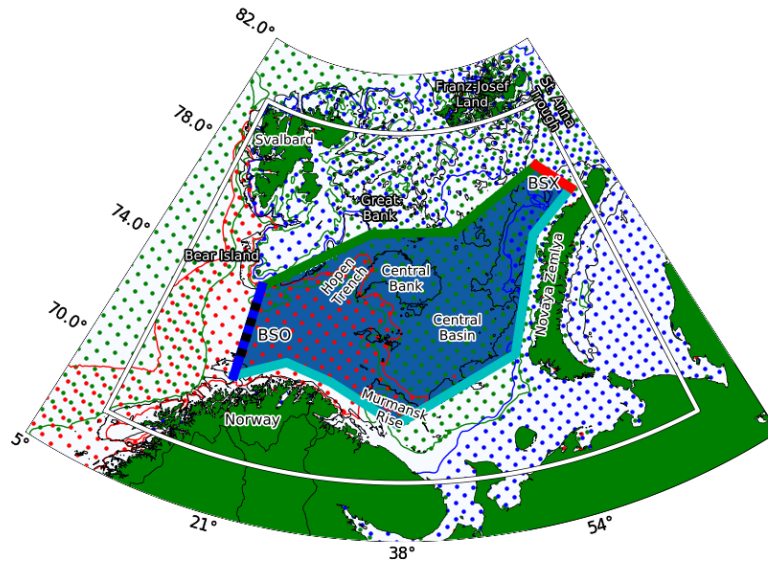


FIGURE 4.2 – Box for budget calculation shown as blue area defined as 69° N 20° E ; 80° N 20° E ; 80° N 54° E ; 76.36° N 65.28° E and 71.1° N 55° E ; 69.5° N 62° E. Lines show boundaries, blue=West, green=North, red=East, cyan=South. Red, green and blue dots hatch the regions with AW, BSW and ArW volume occupancy $> 20\%$, respectively. The thick black dashed line shows the Barents Sea Opening observation section. White line shows the region for sea ice extent calculation. The solid black line indicates the 220 m isobath.

regime change was caused by warming AW but the ocean processes leading to the 2005 regime change are not known due to limited observations. Understanding the ocean dynamics in the Barents Sea is also important because it could be used to determine if the winter sea ice could expand, returning to the previous regime (crossing the Polar Front) or if a tipping point has been irreversibly passed and a further step change reduction in sea ice could occur. We ask, what causes seasonal to interannual variability in AW and BSW volume and properties in the central Barents Sea? Following the regime change in 2005, can the ocean dynamics help predict if a similar or opposing regime change could happen again? We will answer these questions by focusing on the Barents Sea in a high resolution model of the Arctic. In Section 4.2 we describe the model set-up. In Section 4.3 we validate the model in comparison to *in situ* data. In Section 4.4 we calculate the advective heat and freshwater budget for the southern Barents Sea, and analyse the properties within a box. In Section 4.6 the 2005 event is discussed in relation to a similar event in 1990. Conclusions are given in Section 4.7.

4.2 Data and Methods

4.2.1 Model Simulation

We primarily use model output to analyse the heat and freshwater transport budgets and variability of water mass properties in the Barents Sea. The model is a regional configuration of the Arctic and North Atlantic Oceans, using the grid set up defined in Dupont et al. (2015), based on the NEMO (Nucleus for European Modelling of the Ocean ; Madec and The_NEMO_Team (2008)) and LIM3 (Rousset et al., 2015) models for the ocean and sea ice components, respectively. The resolution is $1/12^{\circ}$ which is 4.3 km by 5 - 4 km in the Barents Sea on the irregular

NEMO grid. This grid resolution is not high enough to resolve mesoscale features here, which has a spatial scale of a few kilometres. The model has 75 depth levels which equate to 36 depth levels in the 330 m of the Barents Sea. Surface atmospheric and sea ice flux parameters are calculated in the monthly model output.

Initial conditions are taken from the World Ocean Atlas 2009 climatology for temperature and salinity while the ocean is at rest. The initial sea ice thickness and concentration are taken from a long ORCA12 simulation performed by the Drakkar Group (Barnier et al., 2006; Treguier et al., 2014). Along the lateral open boundaries, monthly climatological conditions (comprising 3-D velocities, temperature and salinity) are taken from the same ORCA12 simulation. Regarding the atmospheric forcing, the latest version of the Drakkar Forcing Set (DFS5.2, which is an updated version of the forcing set described in Brodeau et al. (2010)) is used. Input from the river and ice sheet runoff has been recently corrected to include the large and increasing contribution from Greenland (Gillard et al., 2016). The representation of tidal mixing effect is activated through the new comprehensive parameterization of mixing by breaking internal tides and lee waves (de Lavergne et al., 2019). The simulation covers the period 1979-2015, although only years 1985 to 2015 are analysed in order to allow for model spin up in the first 5 years. The analysis uses monthly means of model output.

4.2.2 Observational Datasets

The realism of the simulation is assessed by comparing the model outputs against the following observation datasets. Satellite SST and sea ice concentration data are used from the OSTIA project spanning January 1985 to December 2016 (Donlon et al. (2012); downloaded from marine.copernicus.eu portal) to validate the model data. This dataset is optimally interpolated from multiple satellite sensors together with *in situ* observations onto a 0.05° grid (1.5×5.6 km for Barents Sea) at a daily frequency. The feature resolution is 10 km and the accuracy of the daily data is ~ 0.57 K (Donlon et al., 2012). Sea ice extent in the Barents Sea is computed from the OSTIA sea ice concentration where the sea ice edge is the 15% contour.

Observations of AW inflow transport and heat transport from the Fugløy-Bear Island section along 20.0° E in the BSO are also used (black dashed line Figure 4.2). This dataset is available through the Norwegian Marine Data Centre portal (www.nmdc.no) and is compiled as monthly means from long term current meter moorings for the period 1997 to 2016. The time series is averaged inflow below 50 m, between 71.5° N and 73.5° N and only considering the part of the water column warmer than $T > 3^\circ\text{C}$ (Ingvaldsen et al., 2004b). A comparable section using the same criteria is taken from the model data.

Temperature and salinity fields from the EN4 dataset are also analysed (EN4.2.0, www.metoffice.gov.uk/hadobs/en4). EN4 comprises *in situ* ship CTD profile data and Argo float data optimally-interpolated on a 1° , monthly z-grid with 42 levels (Gouretski and Reseghetti (2010)). Data are available from January 1980 to December 2016. Within the Barents Sea (10°E to 65°E and 68°N to 80°N) over this time frame, every three-month period has more than 117 profiles. The density of profiles is however biased towards September, October and November when there are usually more than 400 profiles and in the ice-free part of the Barents Sea.

4.2.3 Methods

To calculate budgets of heat and freshwater transport, the Barents Sea boundaries are defined to form a box in Figure 4.2. Heat transport is calculated as $H = \iint (T - T_{ref}) C_p \rho V dx dz$, where C_p is the specific heat capacity of seawater, ρ is the density, V is the velocity, T is the temperature and T_{ref} is the reference temperature taken as 0°C (Arthun and Schrum, 2010). Freshwater transport is calculated as $F = \iint ((S_{ref} - S)/S_{ref}) V dx dz$, where S is salinity, S_{ref} is the reference salinity 35 and V is the velocity (Smedsrud et al., 2010). For the transport calculations, we used the CDFTOOLS package designed to work on NEMO model grids (see <https://github.com/meom-group/CDFTOOLS>). Surface budgets of heat flux, precipitation, river runoff, sea ice melt/freeze, and wind stress are estimated. These parameters are integrated

over the surface area of the same box which has a total area $6.1 \times 10^{11} \text{ m}^2$. Wind stress curl ($\nabla \times \tau$) is calculated as $\nabla \times \tau = \iint (\partial \tau_y / \partial x - \partial \tau_x / \partial y) dx dy$, where $\tau_{x,y}$ is the wind stress on the ocean surface in the zonal, meridional directions of the model grid. The wind stress curl is integrated over the box in Figure 4.2 and negative values represent convergence (i.e. ocean downwelling). Mixed layer depth is calculated from a 0.01 kg m^{-3} change in sigma relative to sigma at 10 m depth. In order to identify the fronts in the model outputs, we follow the equation $|\nabla T_{(x,y)}| = \sqrt{(\partial T / \partial x)^2 + (\partial T / \partial y)^2}$ (Barton et al., 2018). Here, the results are based on the computation of SST gradients by calculating the seasonal mean of the monthly gradient instead of the gradient of the seasonal mean.

There is a 0.1 salinity bias making the model too fresh (Figure 4.1). To account for this bias, the water mass definitions for the model are adjusted by 0.1 salinity to capture the relative variability within the range of the definition properties. The definition used for observations and updated definition for the model properties are shown in Table 4.1.

Linear regressions are calculated using least-squares regression of monthly data with significance estimated at the 95%-level using a 2-tailed Student's t-test. Regression models are calculated using 12-month running mean data to remove the seasonal cycle and focus on interannual variability. Significance is calculated for these regressions using reduced degrees of freedom to account for the running mean.

The amplitude of interannual variability is calculated as the standard deviation of the 12-month running mean. The amplitude of the seasonal variability is calculated by subtracting the 12-month running mean from the monthly data and calculating the standard deviation of this. The transport data is taken a step further because of evident high frequency variability than seasonal. In this case the amplitude of the seasonal cycle is calculated as the standard deviation of the monthly climatology. The amplitude of high frequency variability is then calculated as the standard deviation of the monthly data with the 12-month running mean and seasonal climatology subtracted. Fast Fourier transform (FFT) analysis is used to identify the dominant interannual periodicity in the 12-month running mean timeseries of water mass properties. In this analysis, peaks at resonant frequencies of interannual variability can be identified. Periodicity greater than 15 years are ignored because the 30 year timeseries would not fully resolve more than one cycle in these.

4.3 Model Evaluation

The model sea ice extent also shows a systematic bias relative to the satellite observations (Figure 4.3c). Maps of the sea ice concentration reveal that the model has more sea ice in the coastal southern Barents Sea and over the Central Bank compared to the satellite observations (Figure 4.4). The model also has higher feature resolution than the observations giving it a more rugged edge that may contribute to the systematic bias. The model sea ice extent has a seasonal cycle with similar magnitude to the observations. Interannual variability in the model sea ice extent is a very good simulation of the interannual variability in observations (Figure 4.3c). The model shows a similar sea ice regime change in 2005 to the one observed.

The temperature and salinity properties within the box are represented in T-S diagram format (Figure 4.1). Comparison between the model properties and the observation properties shows the model salinity has a 0.1 fresh bias relative to EN4 when averaged within the box in Figure 4.2. As mentioned in Section 4.2.3, this bias is accounted for by adjusting the model water mass properties as shown in Table 4.1. The property definitions in Figure 4.1 are adjusted to account for this difference. Given that this bias is present in AW properties (Figure 4.1), it suggests the bias is advected into the Barents Sea rather than present due to the excess sea ice shown in Figure 4.3c. The interannual distribution of water properties have a similar clustering in T-S space showing high precision even if there is the bias in salinity accuracy (Figure 4.1). The seasonal range of properties at each location is comparable at 2 to 4 °C for BSW and AW properties. The blue points present in the winter BSW definition are present in both model and observations, and in summer show peroperties warmer by ~ 4 °C and fresher by 0.2 to 1. The

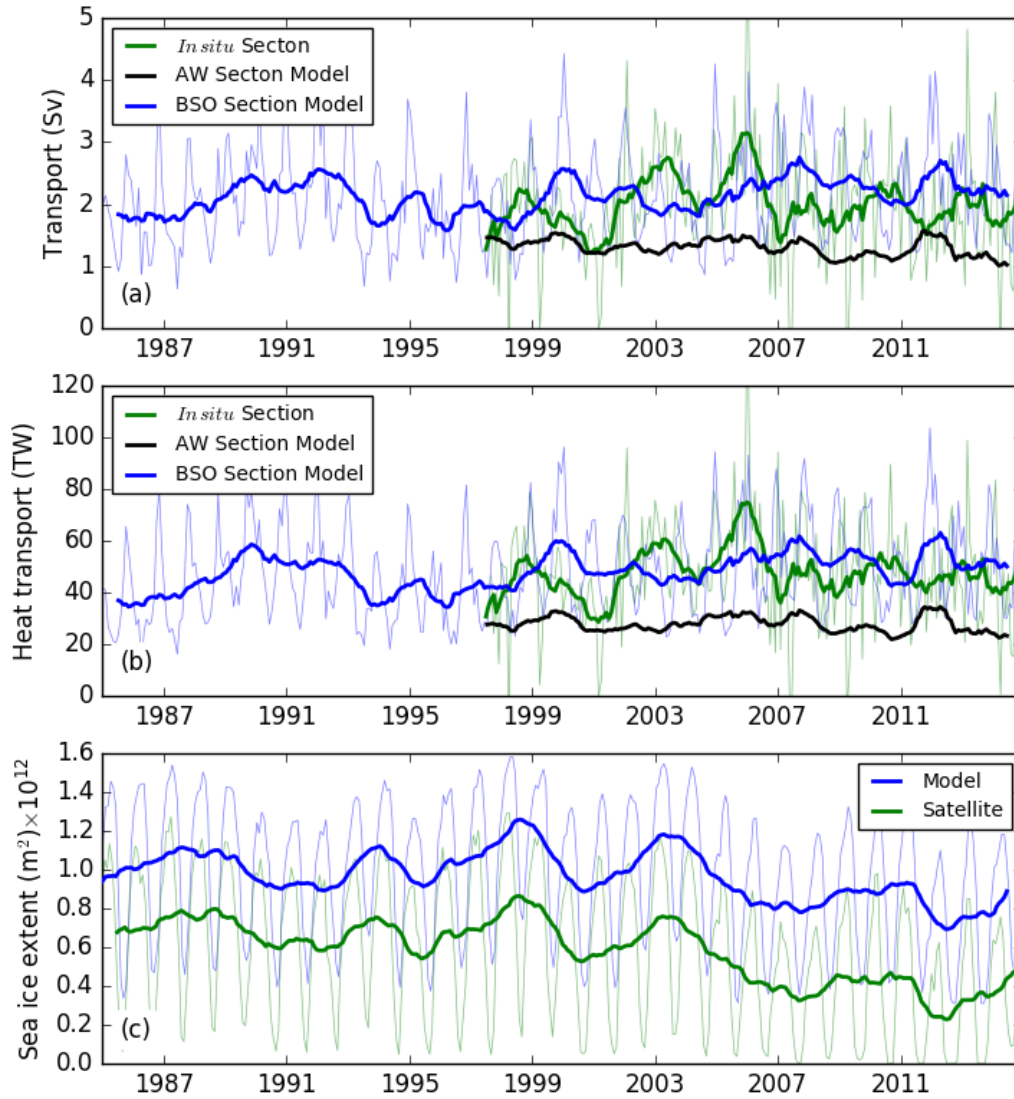


FIGURE 4.3 – (a) Transport and (b) heat transport through the Barents Sea Opening (Fugløy–Bear Island section along 20.0° E). The green line shows the observations of Atlantic Water transport ($T > 3^\circ\text{C}$ and depth > 50 m) across the black dashed line in Figure 4.2, the black line shows model data using the same Atlantic Water definitions as the observations (See Section 4.2.3), the blue line shows model data across the Barents Sea Opening (BSO, blue line in Figure 4.2) with depth > 50 m but without the Atlantic Water definition. (c) Sea ice extent within the Barents Sea (68°N to 80°N and 10°E to 65°E) for model and satellite observations. In all cases, thin line show monthly data and thick lines show 12-month running means.

observations show more locations that are seasonally warmer and fresher than the model. This water could be classed as CW but the seasonal variability suggests this is ArW that can become warmer than the ArW definition, perhaps the difference between CW and ArW needs revising. The other possibility is that seasonal advection moves the water mass boundaries around this location.

The fronts in the Barents Sea affect the sea ice and constrain the water masses present in the region (Oziel et al., 2016; Barton et al., 2018). The climatology of SST gradient calculated over the 2005 to 2014 time period shows the locations of the thermal fronts in the model and observations (Figure 4.4). The locations of the front in the model are in the same places as those found in the observations in all seasons. This shows that the same surface area is available for atmospheric and sea ice interactions in both cases. The realistic locations of the front in the

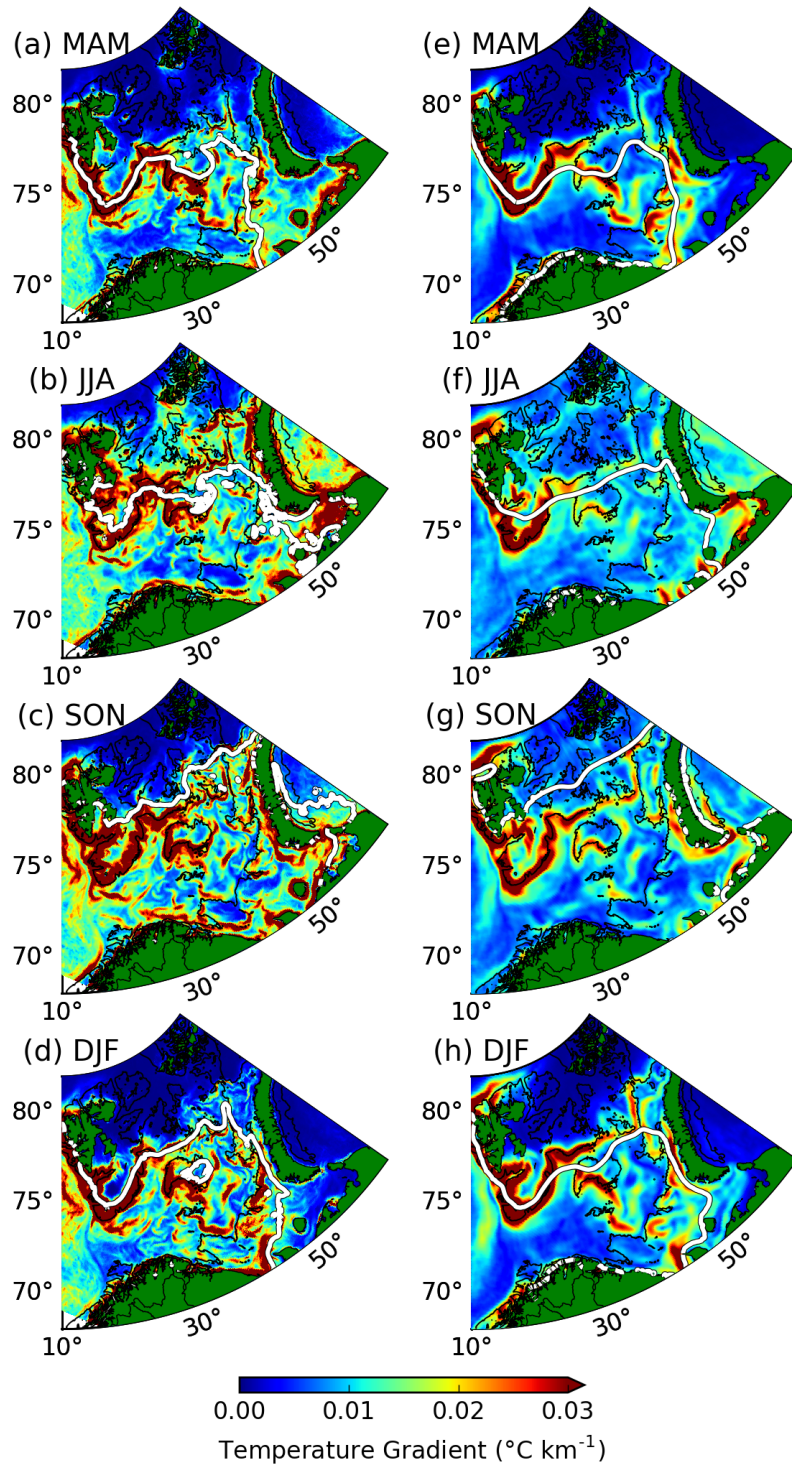


FIGURE 4.4 – Gradient in SST seasonal climatology from 2005 to 2014 for (a,e) spring (March, April and May), (b,f) summer (June, July and August), (c,g) autumn (September, October and November) and (d,h) winter (December, January and February), respectively. (a) to (d) show the model data and (e) to (h) show satellite observations. The sea ice edge is defined by 15% sea ice concentration (white line) and the black line indicates the 220 m isobath.

model also suggests the model captures the interaction between the ocean dynamics and the bathymetry well. Indeed, the main fronts in the Barents Sea have been shown to be associated with bathymetric gradients (Barton et al., 2018). In the observations, the sea ice retreated north of the Polar Front at 76.5 °N after 2005 (Barton et al., 2018). The sea ice in the model persists

over Central Bank for longer in the winters and does not retreat so far north in the summer. While the simulated switch in sea ice regime is less dramatic than the observations, it is the events that surround the change that we are interested in for the rest of the paper.

Current meter observations of transport and heat transport through the BSO are compared to the model in Figure 4.3a,b. These values are calculated from monthly output relative to 0 °C for AW defined as $T > 3$ °C (Ingvaldsen et al., 2004b). Observed transport through the BSO using the AW definition (green line Figure 4.3a) shows systematically more transport (average 2.0 Sv) than the model (average 1.30 Sv) using the same AW definition (black line Figure 4.3a). Observations using the $T > 3$ °C AW definition between 1997-2001 show mean transport of 1.5 Sv (Ingvaldsen et al., 2004b). Discarding the AW definition and using the whole water column Skagseth (2008) estimates 2.0 Sv mean transport. These observations show net volume transport through the BSO is 2.3 Sv with 2.0 Sv of AW inflow, 1.2 Sv of Norwegian Coastal Current transport and roughly 0.9 Sv of AW recirculation (Smedsrud et al., 2013; Skagseth et al., 2011; Skagseth, 2008). Any potential systematic biases due to applying the constraints of the width of the observation section on the model were eliminated by choosing to evaluate total transport through a wider BSO section (Figure 4.2). Given that the Norwegian Coastal Current and the recirculation branch of AW exiting through the BSO roughly balance, the AW transport observations represent net transport (Smedsrud et al., 2013). The difference in interannual variability between the model and observation transport could be the processing and extrapolation of mooring observations that have both spatial and temporal gaps (Ingvaldsen et al., 2004b). The amplitude of interannual variability (12-month running mean) in the model and observations are 0.27 and 0.4 Sv respectively. The amplitude of the seasonal climatology in the model and observations are 0.60 and 0.28 Sv respectively. Removing both the interannual variability and seasonal climatology leaves high frequency monthly variability with an amplitude of 0.43 Sv in the model and 0.83 Sv in the observations. Figure 4.3a shows the model has a more pronounced seasonal cycle while observations have more higher frequency variability and interannual variability. This high frequency variability in the observations could be the result of mesoscale eddies that the model cannot resolve within the Barents Sea.

4.4 Quantifying Variability in BSW Properties

4.4.1 Volume and Properties

To answer our first question "what causes seasonal to interannual variability in AW and BSW volume in the central Barents Sea?", we evaluate volume, heat, freshwater and forcings budgets within the central Barents Sea. We select a box in the Barents Sea roughly defined by the fronts encompassing the region where AW and BSW are expected to be in contact with the atmosphere or sea ice during winter (Figure 4.2). The boundaries of this box are simplified into four parts (North, East, South, West) as shown by the different colours on the map. Total inflow to the box is mainly through the East boundary (i.e. AW inflow), with BSW being the main export towards the Kara Sea and the St. Anna Trough through the West boundary. The transports through the South and North boundaries are minor in comparison to the West and East boundaries. The South boundary largely corresponds to the Coastal Front and land boundary, while the North boundary is roughly aligned with the Polar Front across which there is less exchange.

While the total volume of water within the box will not vary, the volume of the various water masses can vary with the changes in the distribution of heat and freshwater. Volumes of the water masses are calculated by integrating the volume of grid cells matching the respective properties within the box in Figure 4.2. Within the box in both model and observations, BSW makes up the largest water mass by volume, followed by AW and finally ArW (Figure 4.5). This shows the domain of the box is mostly occupied by BSW and AW, as expected. There is a larger volume of BSW in EN4 than is present in the model, this is a bias that does not affect the variability. The amplitude of the seasonal cycle in BSW volume is $0.16 \times 10^{14} \text{ m}^3$, while the seasonal amplitude in AW volume is $0.11 \times 10^{14} \text{ m}^3$. The seasonal cycles in these water masses are in opposite phase i.e. when BSW volume increases in winter, AW volume decreases (Figure 4.5).

This reflects the winter transformation of AW in BSW at the seasonal timescale and subsequent summer refreshment of the pool of AW. The seasonal cycle in temperature of AW has amplitude of $0.57\text{ }^{\circ}\text{C}$ and BSW temperature has seasonal amplitude of $0.30\text{ }^{\circ}\text{C}$ (Figure 4.5). The seasonal amplitude of AW salinity is 0.027 and the seasonal amplitude in BSW salinity is 0.01 (Figure 4.5). The stronger seasonality in AW salinity is likely a result of seasonal variability in mixing of AW with the Norwegian Coastal Current because it has been shown that the transport through the BSO is wind driven at the monthly timescale (Ingvaldsen et al., 2004b,a; Skagseth et al., 2011; Yashayaev and Seidov, 2015). The advection of this signal through the western Barents Sea could smooth the seasonal cycle by mixing, resulting in reduced BSW salinity seasonality. AW density shows a stronger seasonal cycle of 0.08 kg m^{-3} compared to the 0.03 kg m^{-3} found in BSW. This is to be expected given AW has a stronger seasonal cycle in both temperature and salinity than BSW.

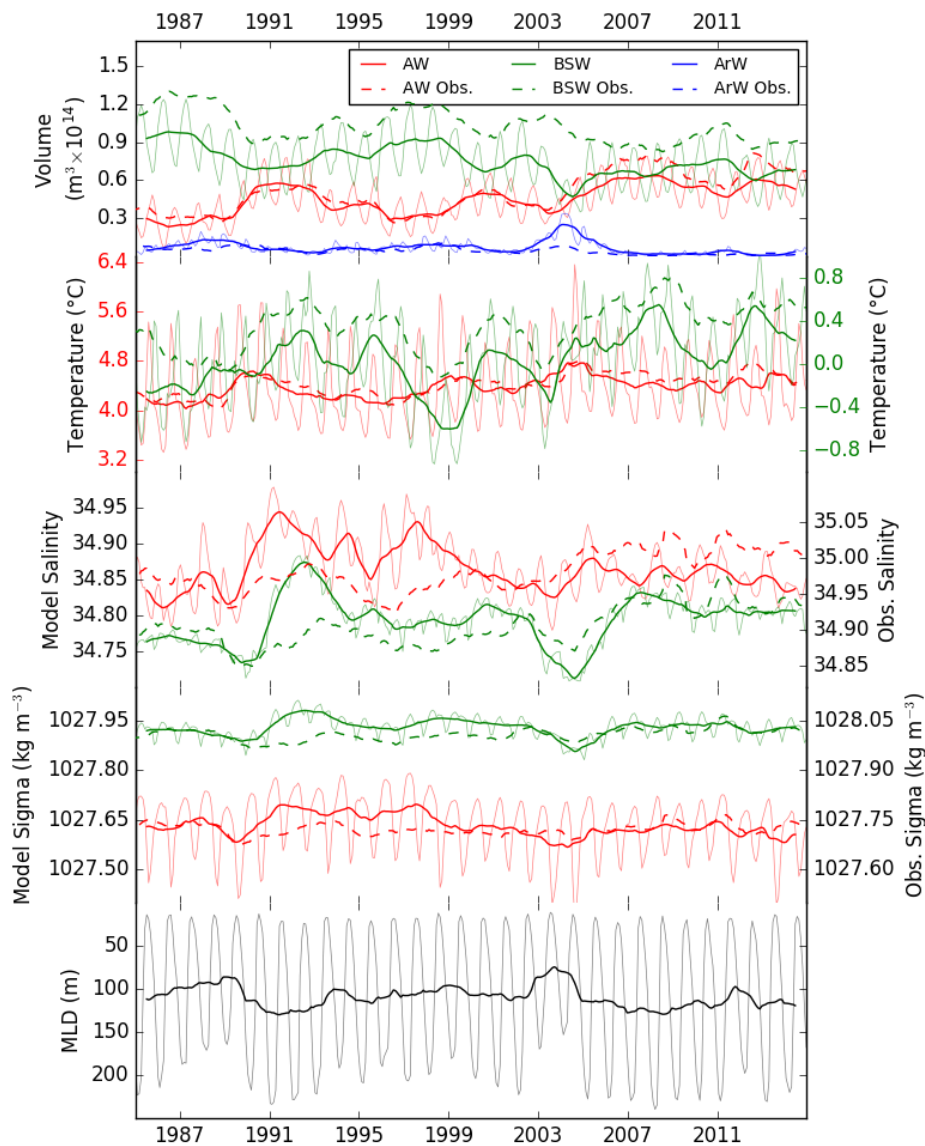


FIGURE 4.5 – Properties within the box shown in Figure 4.2. In each panel the different water masses are represented by the colour in the legend with solid lines showing model values and dashed lines showing observation from the EN4 dataset. Interannual variability is calculated as the 12-month running mean. From the top downwards : the water mass volumes, temperature (where AW is on left axis, BSW is on right axis), salinity (where model is on left axis, EN4 is on right axis), sigma (where model is on left axis, EN4 is on right axis) and the model mixed layer depth (MLD).

The interannual variability in the volume of all three water masses shows good agreement with the interannual variability in EN4 volumes (Figure 4.5). For the 30 years of model data, the mean BSW volume is $0.76 \times 10^{14} \text{ m}^3$ and the amplitude of interannual variability is $0.13 \times 10^{14} \text{ m}^3$. AW volume has mean $0.45 \times 10^{14} \text{ m}^3$ and interannual variability of $0.12 \times 10^{14} \text{ m}^3$. ArW volume has mean of $0.06 \times 10^{14} \text{ m}^3$ and interannual variability $0.05 \times 10^{14} \text{ m}^3$. FFT analysis of the model shows BSW volume has periodicity at 4 and 14 years, while AW and ArW volume have periodicity at 7 and 14 years (graph not shown). The interannual variability in the modelled volume of BSW shows minima of $0.7 \times 10^{14} \text{ m}^3$ in 1990 and $0.45 \times 10^{14} \text{ m}^3$ in 2004. In 1990 the minimum in BSW is preceded by a $0.1 \times 10^{14} \text{ m}^3$ peak in ArW volume, while in 2004 the minimum in BSW is preceded by a $0.3 \times 10^{14} \text{ m}^3$ peak in ArW volume. In both events, 2 years after the ArW volume peak, AW volume increases from around $0.3 \times 10^{14} \text{ m}^3$ to $0.6 \times 10^{14} \text{ m}^3$, compensating the minimum in BSW volume. Compared to the amplitude of interannual variability, these anomalies are noteworthy and will be addressed in greater detail in Section 4.5. The seasonal variability in BSW volume shows a portion of the BSW volume is exported from the formation region every year but a reservoir remains (Figure 4.5). The reservoir will give the properties a "memory" from one year to the next. This is important because these properties influence the properties of Arctic Intermediate Water. The minima events in BSW volume are of particular interest because they show an even smaller reservoir of BSW can be kept in the central Barents Sea, further delineating the interannual variability in BSW properties before and after the events.

The interannual variability in water mass volume is a product of the water mass properties as shown by Figure 4.6. This shows within the water column, temperature anomalies are associated with AW volume anomalies, the freshest salinity anomalies are associated with ArW volume anomalies and density anomalies are associated with BSW volume anomalies, as would be expected from the T-S diagram (Figure 4.1). The low BSW volume anomalies follow low salinity anomalies and warm temperature anomalies. This is in agreement with model results of [Årthun et al. \(2011\)](#); [Oziel et al. \(2016\)](#). The salinity and density anomalies appear first at the surface and propagate to the base of the deeper water column in 1 to 2 years, shown by the diagonal inclination of the anomalies in the Hovmöller plots (Figure 4.6). By contrast, temperature anomalies can also be found isolate below the surface. The temperature anomalies do not show the same diagonal inclination and downward propagation through the water column like the salinity anomalies and tend to be present throughout the water column. This indicates they are mostly ubiquitously advected into the box rather than surface forced. There are surface temperature anomaly minimums in 1989, 1997 and 2003 but they do not propagate downwards. The surface temperature minimum in 2003 is -0.75 , enough to overcome the mean temperature stratification (left panel in Figure 4.6), indicating the box's water column became salinity stratified at this time.

Interannual variability in model temperature for both AW and BSW are comparable to the interannual variability in the EN4 data (Figure 4.5). FFT analysis of the model data shows BSW temperature has periodicity at 4, 6 and 14 years, while AW temperature has periodicity at 5, 7 and 14 years (graph not shown). The interannual amplitudes in temperature are 0.26 and 0.17°C for BSW and AW respectively. For BSW, this is comparable to the seasonal amplitude but AW shows much less interannual variability than the seasonal variability. The larger interannual amplitude in BSW suggests interannual variability is not solely advected from AW. Model salinity is a reasonable simulation of EN4 salinity but it is not as good as the agreement in temperature. Modelled AW salinity overestimates EN4 salinity by 0.03 to 0.08 between 1990 and 2000. The model also suggests the peak in BSW salinity in 1993 is greater by 0.08 than the one found in EN4. It is possible that some variability in EN4 salinity is undersampled but it is more likely that the model lacks some freshwater in the inflowing AW during this period. The range of values on the axes for the model salinity and observation salinity are the same in Figure 4.5 and shows the change in salinity when AW forms BSW is 0.07 for both the model and the observations. This suggests the process for formation of BSW in the model is accurate. Similarly the density transformation is 0.30 and 0.28 kg m^{-3} for the model and observations respectively, reinforcing the idea that BSW salinity comes from AW salinity and giving justification to the adjustment of

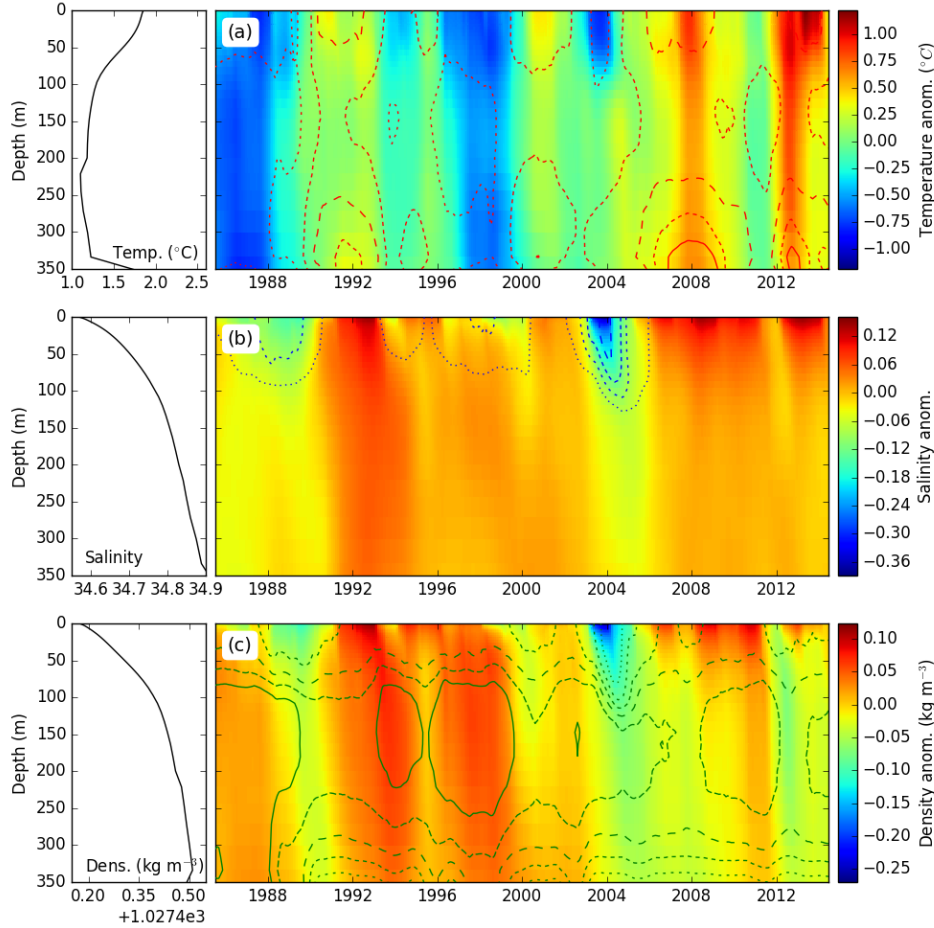


FIGURE 4.6 – Hovmöller plot showing interannual variability in stratification anomalies for (a) temperature, (b) salinity and (c) density averaged with the box shown in Figure 4.2. The anomalies are calculated by subtracting the time-averaged T, S or σ profile (shown in the panels left of (a), (b) and (c)) from the respective 12-month running mean profile to show interannual variability. Contour lines show the percentage of the depth layer within the box occupied by (a) AW, (b) ArW and (c) BSW, again with a 12-month running mean. Contour lines at 10 % intervals from 10 % (dotted line) to 60 % (solid line) with lines becoming more solid with increasing percentage occupancy. Note the depths below 300 m are only present in the western Barents Sea.

fresher water mass definitions for the model (Table 4.1). The FFT analysis of model data shows BSW salinity has periodicity at 5, 7 and 14 years like AW temperature (graph not shown). The FFT of AW salinity shows periodicity at 3.5, 7 and 14 years. The salinity of both AW and BSW have interannual variability amplitude of 0.03. For BSW, this is larger than seasonal variability but for AW, seasonal variability is larger.

From 2004 up to the end of the model run, AW volume and temperature inside the box increases, as does BSW temperature (Figure 4.5). The increase in AW volume is in agreement with the results of [Oziel et al. \(2016\)](#). Over this time period, there is stronger ocean-to-atmosphere heat flux than before 2005 and sea ice extent and melt are lower and less variable (Figure 4.7 and 4.3).

4.4.2 Transport and Flux Budget

Volume is conserved in the model so the total transport into the box through the boundaries is zero (black line, Figure 4.8a). Average transport of 2.1 Sv input to the box comes almost entirely through the BSO at the West boundary and 1.53 Sv exits through the East boundary (Figure 4.8a). As expected, average transport out of the North and South boundary are 0.26 Sv

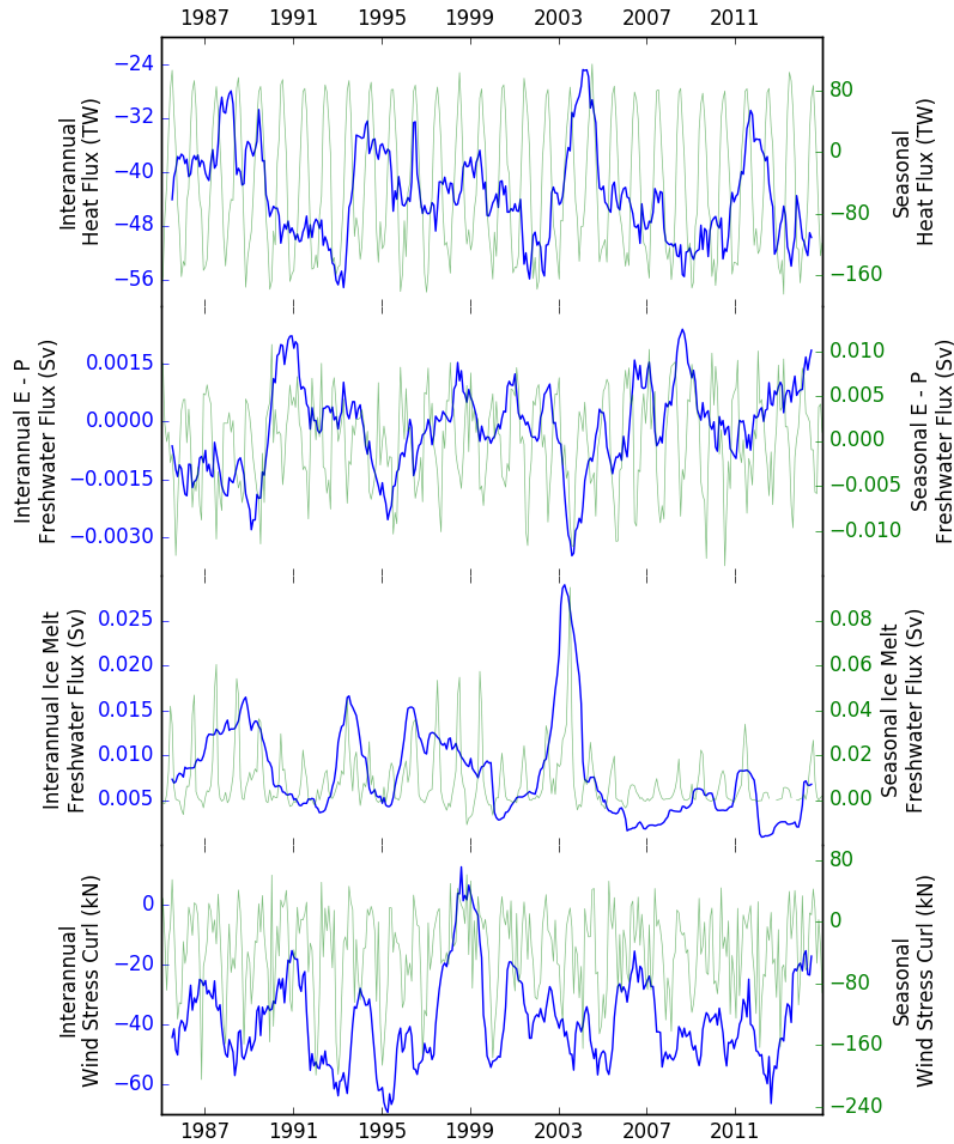


FIGURE 4.7 – Surface fluxes within the box shown in Figure 4.2. From the top down : heat flux, evaporation minus precipitation (E - P), sea ice melt and wind stress curl which are integrated over the surface area of the box in Figure 4.5. Interannual (12-month running mean) variability is shown in blue on the left axes, seasonal variability is shown in green on the right axes. For heat flux, negative values show heat flux from ocean to atmosphere. For evaporation minus precipitation (E - P) negative values indicate net freshwater flux into the ocean. Wind stress curl is calculated from the downward surface stress on the ocean and negative values in wind stress curl represent convergence.

and 0.34 Sv respectively. The amplitude of interannual variability in volume transport are 0.27, 0.16, 0.20 and 0.13 Sv at the West, North, East and South boundaries respectively. For comparison the seasonal variability is 0.74, 0.26, 0.44 and 0.23 Sv at the West, North, East and South boundaries respectively. This shows the stronger interannual and seasonal variability in the West and East boundaries, as these boundaries lie across the path of AW and BSW as these water masses transit through the Barents Sea. The Barents Sea appears to act as a filter where both the interannual and seasonal variability in transport speed at the West boundary have smaller amplitude at the East boundary. The main features of the interannual variability in volume transport through the West and East boundaries are peaks in transport strength between 1989 and 1993 and between 1999 and 2002.

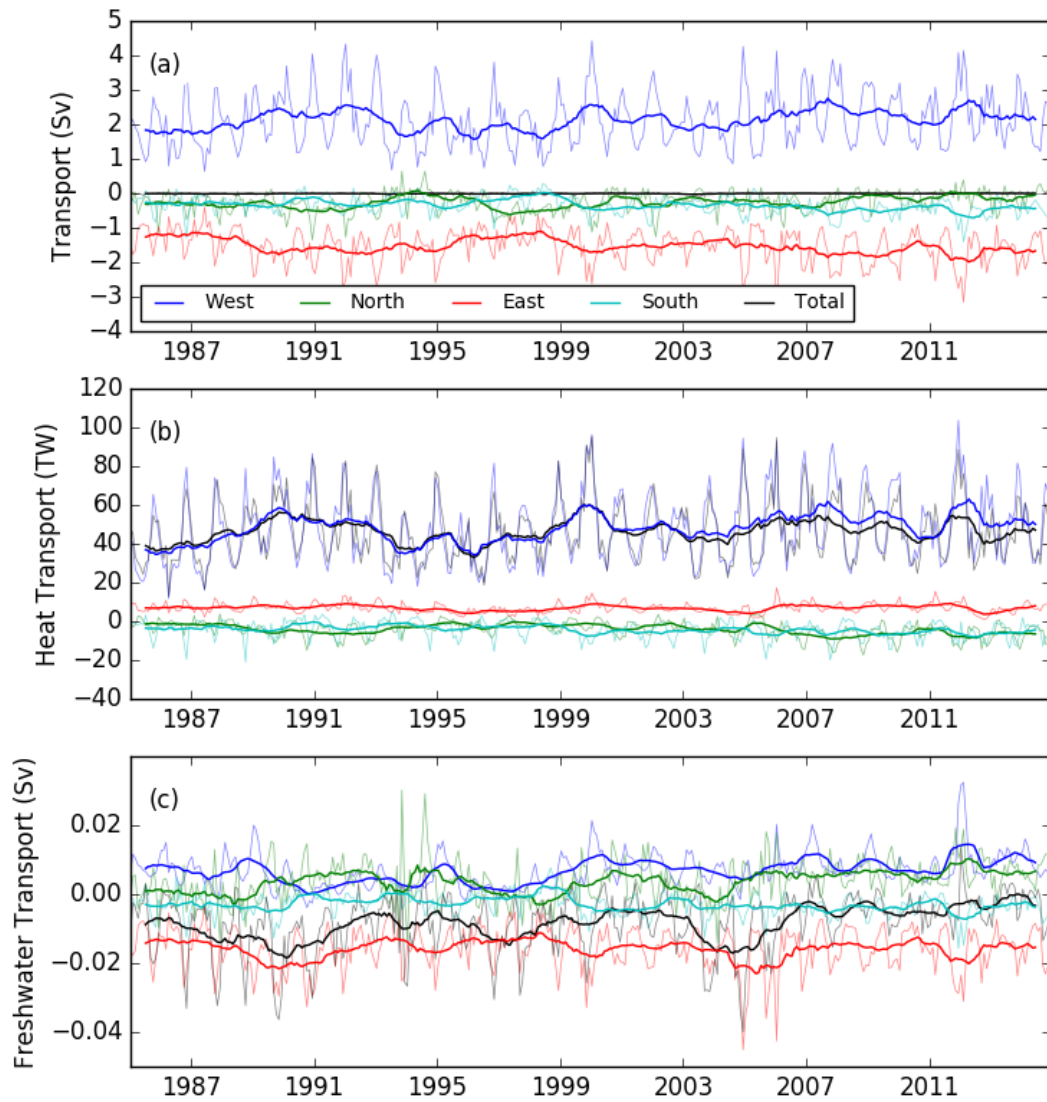


FIGURE 4.8 – Ocean volume transport (a), heat transport (b) and freshwater transport (c) at the West, North, East and South boundaries for the box shown in Figure 4.5. In each panel the colour of the line corresponds to the colour of the boundary on the map with the exception of the black line which is the total sum of transports.

The heat budget can be calculated from ocean heat transport and surface heat flux. Average heat transport entering the box through the West boundary is 47 TW and is not fully compensated by oceanic heat import of 6.9 TW at the East boundary and export of 4.1 and 4.3 TW at North and South boundaries (Figure 4.8b). Heat transport through the BSO is in agreement with observations that show $49 \text{ TW} \pm 7 \text{ TW}$ (Skagseth, 2008) and is between model results suggesting a means 71 TW (Smedsrud et al., 2010) and 28 TW (Årthun and Schrum, 2010). The net heat transport is of similar magnitude to the West boundary suggesting most of the heat entering through this boundary is lost to the atmosphere within the box. This is supported by the average surface heat flux being 44 TW from ocean-to-atmosphere (Figure 4.7). Model results from Årthun and Schrum (2010) also suggest mean ocean-to-atmosphere heat flux of 40 TW. Positive heat transport through the East boundary in combination with negative volume transport at this boundary out of the box, shows the temperature of the exported water here is less than the 0°C reference temperature (Smedsrud et al., 2010). In other words, rather than warm water imported through the East boundary, cold water is exported from the box instead. Export temperatures around 0°C and heat transport roughly agree with the observations of Schauer

et al. (2002); Gammelsrød et al. (2009).

The amplitude of interannual variability at the West boundary is 6.8 TW and seasonal is 16.6 TW (Figure 4.8b). This seasonal variability is comparable to the model results of (Smedsrud et al., 2010). The interannual amplitude in ocean-to-atmosphere heat flux is 7 TW and the seasonal cycle is 86 TW (Figure 4.7). This shows the interannual variability in surface heat flux and ocean heat transport are similar but the seasonal cycle in surface heat flux is greater than the ocean heat transport because of seasonal solar heat gains. The amplitude of both interannual and seasonal variability at the other boundaries are all less than 5 TW (Figure 4.8b). From 2003 onwards, the heat transport through the West boundary and net heat transport diverge by 5 to 10 TW, consistent with increases in oceanic heat export through the North and South boundaries over the same time period (Figure 4.8b).

The freshwater budget can be calculated from freshwater transport through the boundaries, evaporation minus precipitation and from sea ice melt. The freshwater transport at the West and North boundaries have mean import to the box of 0.0068 Sv and 0.0037 Sv respectively (Figure 4.8c). Smedsrud et al. (2010) estimates the freshwater transport in the Norwegian Coastal Current as 0.02 Sv which is greater than our freshwater transport through the West boundary but our box does not full account for the Norwegian Coast Current (Figure 4.2). The East and South boundaries have mean freshwater export of -0.0159 Sv and -0.0029 Sv respectively (Figure 4.8c). The seasonal amplitudes are 0.0036, 0.0053, 0.0059 and 0.0028 Sv for the West, North, East and South boundaries respectively. There are similar in amplitude to the interannual variability which is 0.0032, 0.0030, 0.0025 and 0.0017 Sv for the West, North, East and South boundaries respectively. Unlike the volume transport, the freshwater transport does not have net transport through the boundaries of 0. The mean freshwater transports suggest freshwater imported from the West and North boundaries is exported through the East boundary but the average net freshwater transport is -0.008 Sv, showing there is more exported than is imported. At times the imbalance can be 0.015 Sv for example in 1990 and in 2004. This imbalance must be brought about by the freshwater fluxes at the surface.

The freshwater flux from precipitation and evaporation are roughly in balance with a mean of 1.4×10^{-4} Sv of freshwater into the ocean but seasonal variability is 0.005 Sv, which is large compared to the interannual variability of 0.001 Sv (Figure 4.7). The mean atmospheric freshwater flux is not enough to balance the net freshwater transport budget (Figure 4.8c). Atmospheric freshwater flux interannual variability tends to mirror interannual variability in heat flux (Figure 4.7). This is because the latent heat flux comes from the state change of water, is a component of net surface heat flux and is proportional to evaporation and condensation. The seasonal variability in heat flux and precipitation are in agreement with the results of Chapter 3 and of the model results of Smedsrud et al. (2010) and Ellingsen et al. (2009).

Fluxes to the ocean come from the sea ice as well as the atmosphere. Sea ice melt is the balance of total sea ice melting and total sea ice freezing. The freshwater flux from sea ice melt has a mean value of 0.008 Sv with interannual and seasonal amplitude of 0.05 Sv and 0.12 Sv (Figure 4.7). The volume of the sea ice melt is great enough to balance the net freshwater transport out of the box and suggests this addition of freshwater is exported through East boundary (Figure 4.8c). Figure 4.7 shows ice melt rarely becomes negative which would indicate net freezing within the box, therefore sea ice is mostly imported. Comparing the ice melt to the associated salt flux shows the salinity of sea ice melt water is relatively constant at 6.4. Net melting within the Barents Sea of sea ice with salinity 6.4 is roughly in agreement with model results of Ellingsen et al. (2009). The sea ice melt within the box is dependant on sea ice extent and after 2005, sea ice extent is reduced (Barton et al., 2018). Modelled freshwater flux from sea ice melt has a mean of 0.010 Sv for 1985-2005 and 0.004 Sv for 2005-2015. This is a greater change in freshwater flux than the 0.002 Sv estimated using the sea ice extent for roughly the same area (Barton et al., 2018). The difference reflects the greater sea ice volume than the estimate from seasonal melt between winter maximum extent and summer minimum extent.

Wind stress curl indicates whether atmospheric forcing is imposing convergent or divergent wind conditions on the box. On average wind stress curl is -38 kN with interannual amplitude

15 kN and seasonal amplitude 53 kN. In general, Figure 4.7 shows more intense seasonal variability in wind stress curl in the first half of the time series.

To summaries, variability in modelled AW and BSW properties are in reasonable agreement with observations from EN4. AW temperature, AW salinity and BSW salinity share periodicity at 7 years but BSW temperature shows periodicity at 4 and 6 years. Seasonality in BSW volume is out of phase with seasonality in AW volume representing the seasonal transformation of AW into BSW. This seasonality in volume removes some BSW from the box but the remaining volume gives it a "memory" of the previous year's properties. At two events in 1990 and 2004 the volume reaches minima where the "memory" is reduced. AW salinity has larger amplitude seasonal variability than interannual but BSW has larger interannual variability than seasonal. This is perhaps a feature of the BSW "memory" filtering higher frequency seasonal variability but being influenced by the volume minimum events. The positive BSW volume anomalies in the water column are associated with positive density anomalies. These density anomalies can come from freshwater propagating downwards from the surface or temperature anomalies that are instantaneously distributed throughout the water column. Between 1985 and 2003 the incoming ocean heat transport is equivalent to net heat transport (i.e. ocean-to-atmosphere heat flux) showing the box is in balance but after 2003 the West boundary heat transport and net heat transport diverge showing the imported heat in the West is no longer balanced by ocean-to-atmosphere heat flux.

4.5 Notable Events in BSW Variability

Throughout the simulation, there are occasions on which larger-than-average fluctuations occurred. These fluctuations, referred to as events, are most pronounced in the volume and salinity minimums of BSW that occur in 1990 and 2004 (Figure 4.5). These two events are the focus of this section because they represent times when there is a smaller reservoir of BSW and a reduced "memory" of BSW properties within the box.

Focusing first on the period around 1990, the reduction in BSW volume is accompanied by a decrease in BSW sigma, mainly due to freshening (Figure 4.5). Before the 1990 event, ArW volume in the box increases to $0.1 \times 10^{14} \text{ m}^3$ and then declines during the event suggesting mixing between this ArW and BSW as a source of the fresher salinity of BSW at the start of the 1990 event. Before this event, in 1989, Figure 4.3 shows modelled sea ice extent was relatively large at $1.1 \times 10^{12} \text{ m}^2$ but decreased to $0.9 \times 10^{12} \text{ m}^2$ during the event suggesting the balance of ice freezing/import was outweighed by local melt. Sea ice melt was 0.015 Sv in 1988, and together with the modest net freshwater input through precipitation of -0.0015 in 1989, likely contributed to the 1990 freshwater event. The greater freshwater content added buoyancy to the upper ocean and decreased the winter mixed layer depth from 200 m in 1986 to 160 m in 1989 (Figure 4.5). The input of freshwater and increase in ArW volume strengthens the water column stratification before the freshwater anomaly is mixed downwards (Figure 4.6). Around 1990, AW temperature also increased, followed by the greater ocean-to-atmosphere heat loss (Figure 4.7). Transport through the West boundary also reached a local maximum of 2.5 Sv in volume transport and 60 TW in heat transport (Figure 4.8). The net ocean heat transport also increases showing the increase in heat transport contributes to the increase in ocean-to-atmosphere heat flux. This is an important point because it is more commonly accepted that the atmosphere forces the ocean and atmospheric variability manifests internally (Blackport et al., 2019), here we show the ocean temperature anomalies do not begin at the surface (Figure 4.6). The ocean-to-atmosphere heat flux is in agreement with the results of Årthun et al. (2011); Årthun and Schrum (2010). The combination of these changes and the increase in AW volume show a larger inflow of AW, flushing a significantly larger portion of BSW out of the Barents Sea (Figure 4.5). Under this flushing hypothesis, the increased volume and temperature of AW causes greater surface heat loss to the atmosphere but in order to balance the budget it also results in a warmer BSW temperature (Figure 4.5 and 4.8). As the event evolves through 1991-92, salinity and density of BSW increase due to increased saline AW influence, restoring the volume of BSW (Figure 4.5). This salinity

increase also decreased the upper ocean buoyancy (positive density anomaly in upper 50 m in 1991-92) and deepened the winter mixed layer to 230 m in 1991 (Figure 4.6 and 4.5).

We now focus on the 2004 BSW volume minima event. This event shows a similar decline in BSW sigma and salinity (Figure 4.5). This event occurs at the same time as a marked increase in ArW volume to $3.5 \times 10^{13} \text{ m}^3$ (Figure 4.5a). The sigma and volume minimum are also the result of fresher and warmer BSW. Like the event in 1990, sea ice extent is higher than average in winter 2003 (Figure 4.3) but, unlike the 1990 event, this is followed by an exceptionally large peak in sea ice melt of 0.028 Sv in summer 2003 (Figure 4.7). The combination of these two fresh water sources, ArW volume anomaly and sea ice melt anomaly, causes the BSW salinity minimum (Figure 4.6). Unlike the 1990 event, 2004 shows relatively low volume transport of 1.9 Sv and heat transport of 40 TW though the West boundary (Figure 4.8). This event also shows less ocean-to-atmosphere heat flux than the 1990 event, reaching 24 TW, which at the interannual time scale does not balance the 40 TW net heat transport anomaly (Figure 4.7 and 4.8). The combination of this decrease in surface heat loss isolating and accumulating warm water below the surface at 150 m in 2005 (Figure 4.6) and warmer AW temperature (Figure 4.5), is the source of the warm BSW temperature anomaly into 2004 and beyond. The lower volume transport during the 2004 event suggests it is more stagnant transport than 1990, perhaps blocked by the anomalous ArW volume and buoyant freshwater. In contrast with 1990, the decrease in surface heat flux is the result of the temporary lower salinity surface layer forming within the box, limiting the average winter mixed layer depth to 150 m in 2004 (Figure 4.5 and 4.6). The main difference between 1990 and 2004 for surface heat flux is that the water column becomes salinity stratified instead of temperature stratified in 2004, meaning AW is unable to interact with the atmosphere and reduces the transformation rate of AW into BSW. The decrease in winter mixed layer depth before the 1990 event appears to have had the same effect, decreasing surface heat flux but to a lesser extent. The transformation rate of AW to BSW has not increased enough after 2004 to restore BSW volume to the 60 % of some depth layers it occupied before 2004 (Figure 4.6). The upper water column shows positive density anomalies near the surface after 2005 that weaken the water column stability and deepen the mixed layer depth.

4.6 The Emergence of a Regime Shift

In line with our questions in Section 4.1, this section explores the mechanisms at play for the BSW volume anomalies within the box using lead-lag regressions. Lagged regression between the various properties in Figure 4.5 show that a positive anomaly in sea ice extent is preceded by a negative anomaly in AW temperature by 7 to 35 months, with regression values peaking at -0.6 around 23 months lag (Figure 4.9a). Sea ice melt positive anomalies are also preceded by AW temperature negative anomalies by 5 to 30 months, with regression peaking at -0.58 around 18 months lag. The correlation between AW inflow temperature or AW heat transport and sea ice has been identified in model results of Årthun et al. (2012) and observations of Herbaut et al. (2015); Onarheim et al. (2015). AW temperature can contribute directly to sea ice melt and the lag times we identify are consistent with 1 - 2.5 year flushing time for the Barents Sea (Smedsrud et al., 2010). Ocean-to-atmosphere surface heat flux anomalies lags behind positive AW temperature anomalies by 23 to 33 months with -0.48 peak in regression at 28 months. This correlation is in agreement with model results of Årthun et al. (2012) who found heat flux lagged heat transport through the BSO by 2 years. While the positive anomalies of AW temperature precedes negative sea ice extent, melt and heat flux, there is a stronger regression peak of 0.7 with 8 months lag between negative ice melt and stronger ocean-to-atmosphere heat flux (Figure 4.9a). Positive AW temperature anomalies also lead positive AW volume anomalies by -3 to +40 months peaking at regression of 0.8 around 20 months. Positive AW volume anomalies also lag negative BSW volume anomalies by -18 to +38 months peaking with BSW volume leading by 7 months and regression value -0.8. Positive anomalies in AW volume coincide with negative sea ice melt anomalies, peaking at 0 months with regression -0.71.

Positive anomalies in BSW salinity lag behind positive AW salinity anomalies by 0 to 29

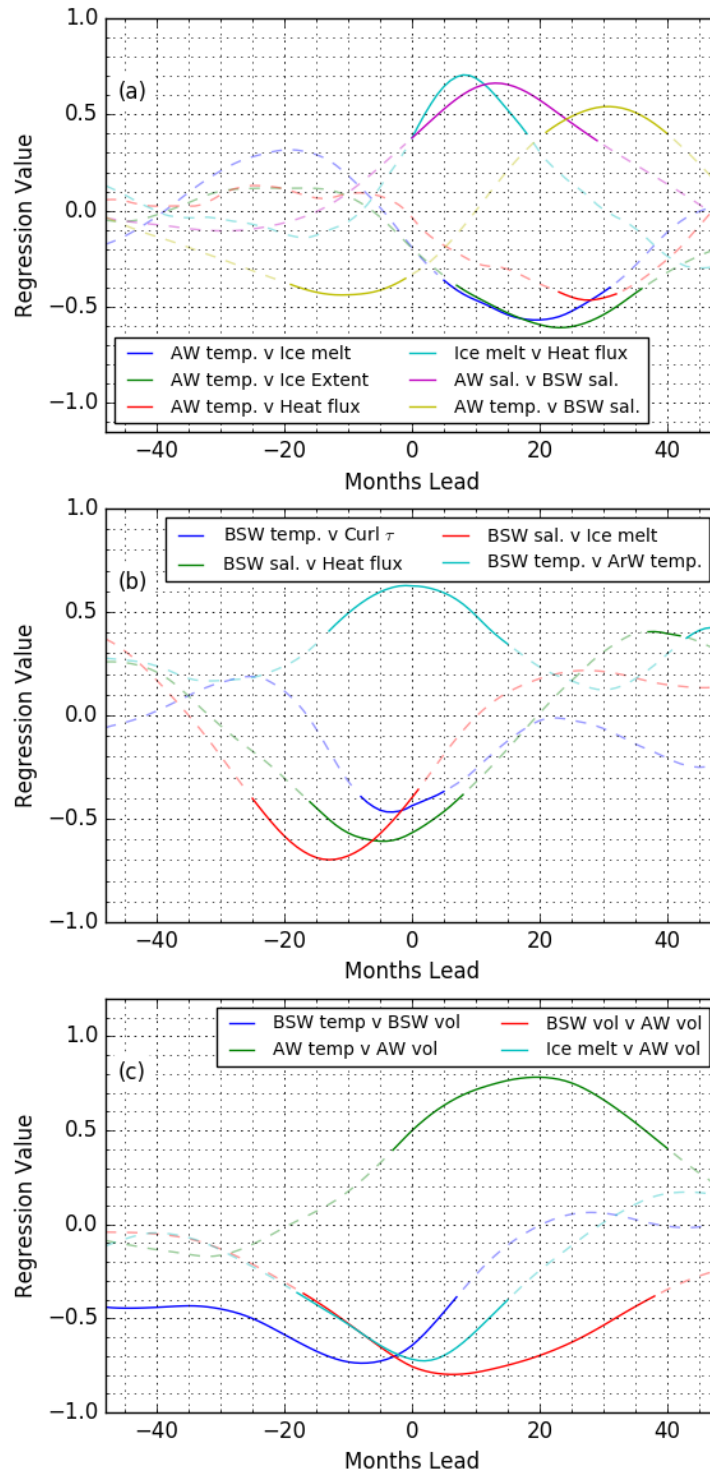


FIGURE 4.9 – Lead and lag regression values for combinations of properties and fluxes shown in Figure 4.5 and 4.7. The legend shows the combination of regressed properties where the property on the left of the v is the independent variable so positive months of lead indicate that the independent variable leads the dependant variable and negative months lead indicate the independent variable lags. The regressions are calculated with 12-month running mean data to focus on interannual variability. The solid lines show regression values significant at the 95% level and dashed lines show insignificant regression with reduced degrees of freedom accounting for the 12-month running mean.

months peaking at 12 months with a regression value of 0.68 (Figure 4.9). Positive anomalies in BSW salinity also lag behind positive anomalies in AW temperature by 20 to 40 months peaking at regression value 0.52 at 30 months. Positive BSW salinity anomalies lead stronger ocean-to-atmosphere heat flux anomalies ranging from +7 to -17 months, regression peaks at -0.6 with BSW lagging heat flux at 5 months. Positive BSW salinity lags negative sea ice melt anomalies by 0 to 25 months peaking at -0.7 at 13 months lag. This is in agreement with Ellingsen et al. (2009), who showed freshwater content lagged sea ice melt and Oziel et al. (2016) who showed ice melt correlated with BSW volume.

Wind stress curl corresponds to Ekman pumping, downwelling water and the potential convergence of heat or freshwater from outside the box. BSW temperature is correlated with wind stress curl, showing a lead of +5 to -8 months and regressions peaking at -0.49 with BSW temperature lagging wind stress curl by 4 months (Figure 4.9). This suggests positive BSW temperature is coincident with convergence/downwelling. Positive BSW temperature anomalies also lag behind negative BSW volume anomalies by +6 to -30 months, peaking at regression value -0.72 with BSW temperature lagging by 8 months. This is in agreement with the wind stress curl causing greater convergence, removing BSW volume from the Central Basin and advecting warmer water.

BSW temperature variability is correlated with ArW temperature peaking at regression value 0.7 at 0 months lag. This correlation is in agreement with the results of Lind and Ingvaldsen (2012) and Lind et al. (2016), who shows the mixing between these water masses affects the temperature of ArW.

Figure 4.9b shows that the negative BSW salinity anomalies lag behind positive sea ice melt anomalies indicating meltwater is mixed into BSW. The correlation of BSW salinity and heat flux is likely following the mechanism where increased freshwater input gives stronger stratification and less ocean-to-atmosphere heat flux. Although BSW salinity has a positive response to AW temperature via the sea ice melt, Figure 4.9a also suggests AW temperature lags BSW salinity by -10 months. There does not appear to be any clear forcing response for this correlation and it would be the result of variability with a similar periodicity. Instead the peak to trough time in the lags correlations quantify half a cycle as 40 months i.e. half the 7 year cycle as confirmed by the FFT analysis.

To clarify the relative timing of anomalies in the Barents Sea and show the mechanisms, Figure 4.10 shows a summary schematic of the main sequence of anomalies. A plausible physical mechanism that supports atmospheric heat flux anomalies originating in the ocean is cool AW temperature anomalies enabling expansion of winter sea ice extent because *in situ* sea ice is a precondition of substantial sea ice melt. Equally, a cool AW temperature anomaly also decreases ocean-to-atmosphere heat flux, a mechanism that is aided by increased sea ice melt, further increasing the vertical water column stability.

The lead-lag regressions can be combined with the events analysis to answer the second question in Section 4.1, "Following the regime change in 2005, can the ocean dynamics help predict if a similar or opposing regime change could happen again?". By understanding the period of ocean variability around the regime change we can identify the conditions required for another step change. The sequence of events leading up to the shift in regime in 2004-05 was as follows (Figure 4.10) :

1. A long-term trend in increasing AW temperature warmed the western Barents Sea from 1980 onwards (Levitus et al., 2009).
2. Anomalously cold AW in 2001 causes an increase in winter sea ice extent and an unusually large summer sea ice melt in 2003.
3. The freshwater released by sea ice melt decreased salinity, density and volume of BSW in 2004.
4. Once this fresher, more buoyant BSW was pushed out of the eastern Barents Sea, volume conservation resulted in a greater volume of warmer AW in the Barents Sea after 2005, helped by convergent wind stress curl.
5. The strong interannual response in AW temperature on top of the long term trend of warming AW decreased sea ice extent in 2005.

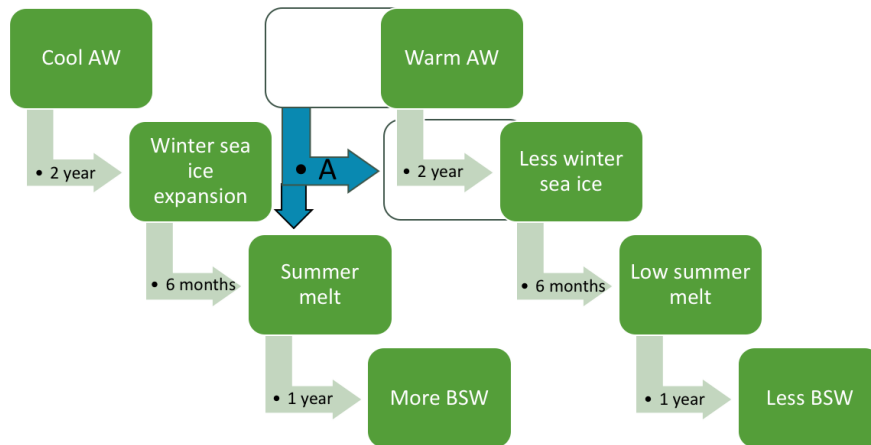


FIGURE 4.10 – Schematic of lead-lag regressions in Figure 4.9. The schematic starts with a cool anomaly in AW temperature as an example. The direction of the arrows show the lead-lag dependance of properties based on the strongest regression value. The arrows specify the time lag between anomalies. The green boxes show the rough time of anomalies and the black outline boxes with blue arrow (A) shows the interaction between warm AW and summer sea ice melt anomalies that results in the extreme event in 2005.

6. This mechanism suggests with the reduced sea ice melt after 2005, the AW temperature will have a greater influence on the surface heat flux since there is reduced strength and variability in stratification.

The imbalance between the inflowing AW temperature and ocean-to-atmosphere heat loss is evident after 2003 in the divergence of heat transport at the West boundary and net heat transport (blue and black lines Figure 4.8). This post-2005 warm period is somewhat entrenched since greater AW temperature means greater AW volume and greater BSW temperature (Figure 4.9). This analysis helps answer the second question in Section 4.1 "Following the regime change in 2005, can the ocean dynamics help predict if a similar or opposing regime change could happen again?". The regression analysis suggests AW temperature is the limiting factors in preventing return to the interannual variability of the pre-2005 regime (Figure 4.9 and 4.10). Without a period of cool AW after 2005, the sea ice extent will remain diminished, stopping the cycle that was present in the pre-2005 regime from occurring after 2005. If a cold anomaly in AW temperature occurs by advection, then sea ice could return to the southern Barents Sea and may initialise the pre-2005 regime.

For the case of identifying if a second complementary regime change could occur, we need to examine the post-2005 regime and identify if AW temperature anomalies could continue to increase the overall temperature of the Barents Sea, either through AW volume increase or BSW temperature increase. By discarding the connection with sea ice melt, BSW salinity is more dependant on AW salinity that before 2005 and BSW temperature increases coincide with stronger wind stress convergence. However, AW temperature could increase AW volume (Figure 4.9), although without the help of the sea ice freshwater anomaly to decrease BSW volume, like in 2004, we speculate there would be higher threshold for a regime change in this way. Due to the overlaps in lead-lag regression it could be possible for AW volume increase to decrease BSW volume which would tend to increase BSW temperature (Figure 4.9). Given that ArW temperature within the box is correlated with BSW temperature, there is potential for further BSW temperature increase to impact winter sea ice in the northern Barents Sea via ArW temperatures (Figure 4.9). This is supported by the increasing heat transport through the BSX and suggests the AW temperature trend is already propagating further north.

4.7 Conclusion

To conclude, the Barents Sea has seen significant changes in sea ice and water mass properties around the mid-2000s ([Årthun et al., 2012](#); [Lind et al., 2018](#); [Barton et al., 2018](#); [Herbaut et al., 2015](#)). Using a high resolution ocean-sea ice model of the Barents Sea we have explored the interannual variability in a box encompassing the southern region largely occupied by Atlantic Water and Barents Sea Water. The lead-lag regressions show cool AW anomalies are followed by greater winter sea ice extent allowing greater summer melt, freshening BSW. Warm AW anomalies are followed by anomalously low BSW volume. This connects the variability in AW properties to BSW properties. The exact mechanism of the regime change in 2005 was unknown but this analysis shows how the change resulted from AW warming trend induced coincidence in the timing of periods in AW volume expansion and extensive summer sea ice melt. This suggests a similar or opposing regime change could happen again.

The model is validated against satellite SST fronts, sea ice, AW transport and hydrographic profiles. BSW volume variability exhibited two anomalously low events in 1990 and 2004. Comparison of the two events reveals a similar sequence of events that are confirmed by lead-lag regressions. In each case a period of cool AW triggers larger winter sea ice extent and subsequently larger summer sea ice melt. This freshwater release combined with relatively fresh AW and a greater volume of ArW cause the BSW volume minima that was subsequently filled by expanding AW volume. The fresh meltwater release in the 2005 event is more extreme than the 1990 event and removed some BSW volume, a change that has yet to be reversed. This combined with the warming trend in the inflowing AW results in the regime shift.

Ocean temperature in the Barents Sea has been predicted to increase up to 1 °C by 2099, mostly due to advection ([Long and Perrie, 2017](#)). Understanding the dynamics in the Barents Sea are important as it has been suggested that sea ice has a chance of returning to pre-2005 conditions in the 2040s ([Årthun et al., 2019](#)). It has also been suggested that the Atlantification of the Barents Sea could extend beyond the Barents Sea into the Eurasian Basin, deepening convection there ([Lique et al., 2018](#)). These results suggest a reversal in the sea ice regime change could occur following a cold AW temperature anomaly lasting 2.5 or 3.5 years (half the dominant 5 or 7 year periods). However, following the 2005 loss of seasonal sea ice, the heat export through the BSX has continued to increase suggesting BSW is inheriting the AW temperature trend, in agreement with ([Barton et al., 2018](#)). This is important for sea ice prediction attempts such as [Onarheim et al. \(2015\)](#) because the sea ice extent in the northern Barents Sea is correlated with AW and ArW temperature even after the regime change ([Lind et al., 2018](#)). The reduced sea ice melt after 2005 also means surface heat flux is more dependant on AW temperature than before 2005, when sea ice melt was an important factor affecting stratification. Understanding the Barents Sea temperature and heat flux variability under the present regime is also important for the coincident extreme weather events in Europe and Asia ([Luo et al., 2016](#); [Petoukhov and Semenov, 2010](#); [Hoshi et al., 2019](#); [Blackport et al., 2019](#)).

Chapitre 5

Summary and Synthesis

5.1 Summary

The purpose of this thesis is to investigate the Arctic Ocean stratification and circulation in the context of changes in seasonal sea ice cover. The motivation for this thesis question comes from observations of the changing Arctic environment. The Arctic surface air temperature has been warming more rapidly than the global average (Serreze et al., 2009; Screen and Simmonds, 2010a). These changes make it important to understand the ocean dynamics to improve predictions about the future Arctic and impacts it may have on the climate at lower latitudes. In particular, reduction in Barents Sea sea ice has been shown to cause anomalously cold winter surface air temperature in Europe and Asia (Hoshi et al., 2019; Mori et al., 2014).

The Barents Sea has been a focus of this thesis because it is a region of the Arctic in the marginal ice zone where there is some seasonal sea ice coverage. This enabled the study of the ocean in the presence of sea ice while utilising historic observational datasets. Both the Eurasian Basin of the Arctic Ocean and Barents Sea have been becoming warmer and saltier, a phenomenon known as "atlantification" (Polyakov et al., 2017; Årthun et al., 2012). Given that the Barents Sea also produces Barents Sea Water (BSW), part of Arctic Intermediate Water (Karcher et al., 2011; Lique et al., 2010), it is important to understand the changes in dynamics of this region. Following this, the thesis has identified that very little is known about BSW, its formation and response to longer term trends.

This study has addressed the question : how does the seasonal sea ice impact ocean stratification and mean flow ? This has been addressed from different perspectives in each of the three results Chapters 2, 3 and 4.

- Chapter 2 answers the questions : where is the Polar Front's location in the eastern Barents Sea, how does this compares to the seasonal sea ice edge and what are the implications for BSW formation given the documented sea ice loss and atlantification of the Barents Sea ?
- Chapter 3 answers the question : how can satellite data can be used to obtain information on the heat and freshwater content variations within the water column and in particular to measure BSW variability.
- Chapter 4 answers the questions : what causes seasonal to interannual variability in AW and BSW volume and properties in the central Barents Sea ? Following the regime change in 2005, can the ocean dynamics help predict if a similar or opposing regime change could happen again ?

In this Chapter, the three results chapters will be summarised highlighting the new results produced in this thesis, synthesis will follow in Section 5.2 to answer the main question, in Section 5.3 the methods used will be evaluated and future work that could lead on from this thesis will be presented.

5.1.1 Chapter 2 : Observed atlantification of the Barents Sea

Chapter 2 focused on satellite sea surface temperature (SST) observations of the Polar Front. Previous studies suggested a broad range of variable locations for the Barents Sea Polar Front, with 600 km between the most southerly to most northerly estimate (Smedsrud et al., 2010; Oziel et al., 2016). These estimates were based on either temperature or salinity definitions. Narrowing down the location of this front is important because it divides temperature stratified water from salinity stratified water and defines the surface area available for direct ocean-ice-atmosphere interaction (Figure 5.1). These interactions are important for the formation of Barents Sea Water (BSW) that contributes to Arctic Intermediate Water (Schauer et al., 1997; Maslowski et al., 2004). The surface area defined by the Polar Front will affect atmospheric heat loss and sea ice variability in this region that has been associated with winter surface air temperature variability in Europe and Asia (Hoshi et al., 2019; Mori et al., 2014).

Our results focused on finding the front using the gradient in SST data and comparing it with *in situ* hydrographic profile climatologies. This method shows the mean location of the Polar Front is along a bathymetric ridge produced by Great Bank and Ludlov Saddle at 76.5

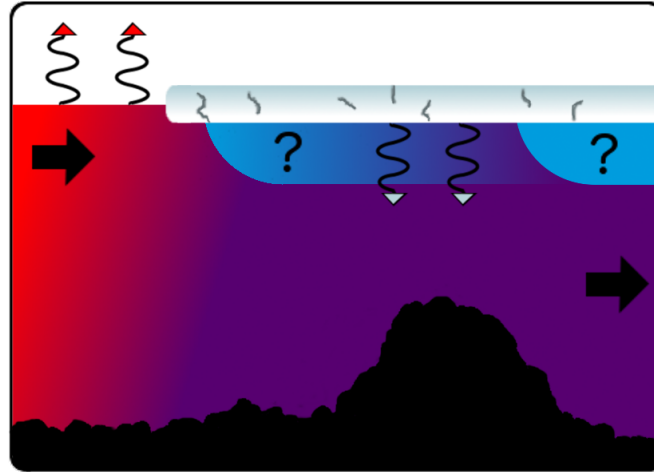


FIGURE 5.1 – Schematic of the Polar Front where blue represents Arctic Water, red represents Atlantic Water and purple represents Barents Sea Water. Sea ice is represented by the grey box. Red arrows show ocean to atmosphere heat flux and blue arrows show freshwater flux from sea ice melt.

°N. The Barents Sea SST was shown to have experienced a warming trend that started in the western Barents Sea and propagated into the Central Basin. Empirical orthogonal function (EOF) analysis suggested the variability in SST came from AW temperature at the Barents Sea Opening (BSO) but also affected the surface air temperature across the eastern Arctic. While previous studies found natural variability in AW temperature was linked to sea level pressure, the EOF analysis showed no significant correlation with sea level pressure and suggested this recent warming trend was an extension outside of the natural atmospheric forced variability. The warming trend resulted in a significant increase in BSW temperature between 1985-2004 and 2005-2016 that prevented the extension of winter sea ice south of the Polar Front after 2005. This meant BSW became significantly saltier, partly from a trend in AW salinity and partly from the decline in fresh, seasonal sea ice melt. This regime change was a non-linear shift, from one stable climate system that has been present since at least 1850 where winter sea ice crossed the Polar Front, to a new sea ice climate system (Figure 5.2).

5.1.2 Chapter 3 : Satellite water mass properties

Chapter 3 primarily attempts to develop a technique to extract more information from existing satellite datasets. As identified in Chapter 2, variability in BSW is important for Arctic Intermediate Water properties. In the Barents Sea we can monitor BSW with satellites before it is isolated from the surface. The Barents Sea is a region where water transitions from temperature stratification to salinity stratification (Carmack, 2007). At the low water temperature found here, especially during winter, traditional methods of estimating satellite sea surface salinity (SSS) become very sensitive to temperature variability, rendering them unusable at present. We developed a method of estimating satellite based freshwater content and SSS that takes advantage of the decreased sensitivity of density (and steric height) to temperature at low temperatures, reinforcing the salinity contribution relative to the temperature contribution.

The proposed method uses a combination of physical equations and statistical regression to obtain vertically integrated steric height, thermosteric height (proportional to heat content) and halosteric height (proportional to freshwater content) representative of the upper mixed layer. Focusing on the Central Basin where BSW is present, our satellite water properties dataset shows regression values around 0.5 with *in situ* data. The dataset also confirms the change in freshwater

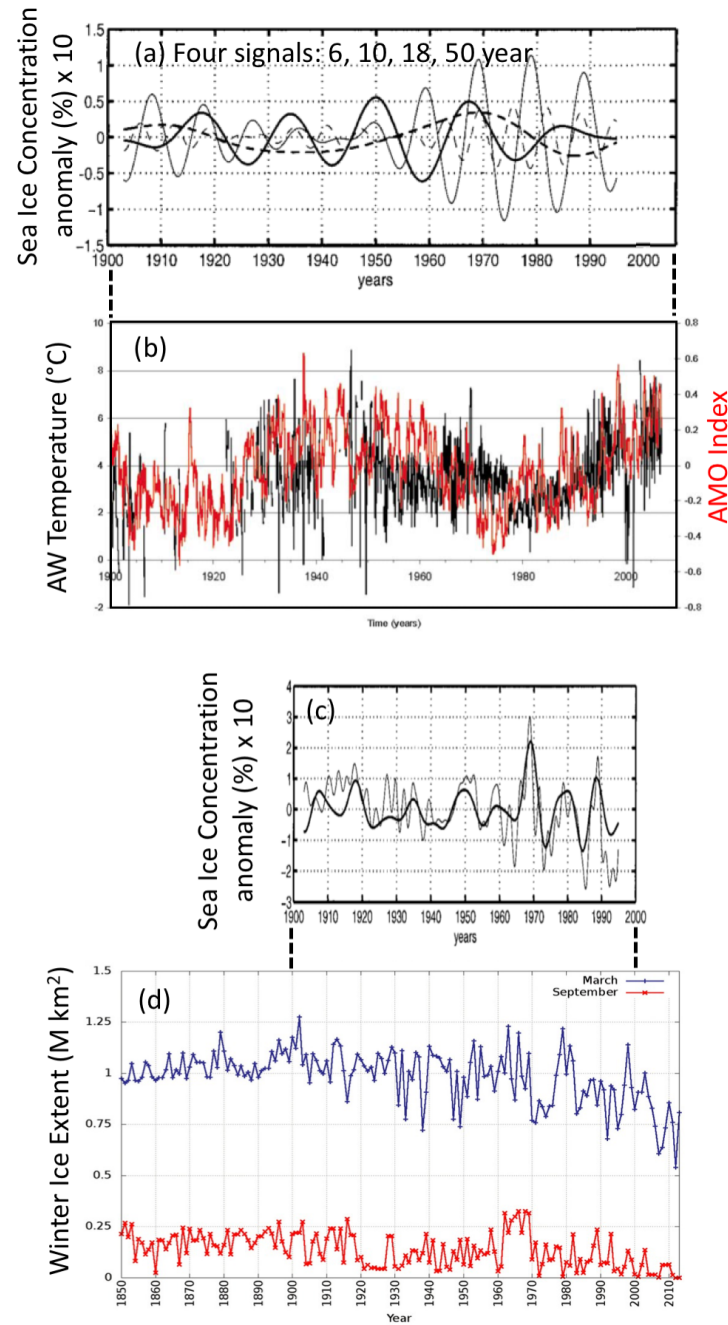


FIGURE 5.2 – Multi-decadal temporal variability in the Barents Sea : (a) the four dominant signals found in the sea ice concentration in the Barents Sea between 35 °E and 75 °E. (b) Atlantic Water (AW) temperature compiled from hydrographic profiles at 100-150 m for 11 - 57 °E, 69 - 78 °N. Atlantic Multi-decadal Oscillation (AMO) defined by detrended SST in the North Atlantic. (c) The thick line shows reproduction of sea ice concentration using the four dominant signals found in (a), the thin line shows observations of sea ice concentration. (d) Winter sea ice extent calculated in an area covering roughly 15 - 65 °E and 67 - 78 °N, data are interpolated ship-based sea ice surveys. The graphs are reproductions (a) and (c) sourced from [Venegas and Mysak \(2000\)](#), (b) sourced from [Levitus et al. \(2009\)](#), (d) sourced from [Walsh et al. \(2017\)](#).

content and salinity that occurs in 2005 found in Chapter 2. Analysis of atmospheric fluxes suggests that seasonal variability in steric height is derived from net surface heating and cooling. Interannual variability in steric height is derived from both heat content and freshwater content but the interannual variability in freshwater content is not associated with local atmospheric

fluxes suggesting advective sources.

5.1.3 Chapter 4 : Model study of Barents Sea Water variability

Chapter 4 returns to the subject of BSW variability and the regime change in 2005 identified in Chapter 2 but using a model based methodology. This method has the advantage of being able to fully resolve interannual variability all across the Barents Sea unlike the *in situ* hydrographic profiles that are less numerous in the north and eastern Barents Sea. The regime change in 2005 is an important event because of the potential for more widespread regime changes to weather patterns. There is a warming trend in the temperature of the northern Barents Sea and the temperature there is correlated with sea ice extent (Lind et al., 2018) and under projected warming up to 2099, convection depth may increase in the Eurasian Basin (Lique and Thomas, 2018). Using model dynamics, Chapter 4 addresses how the change occurred by looking at the timing of events.

Over the 1985 to 2015 time period, the model shows the volume of BSW within the southern Barents Sea box has two distinct minimum events. One minimum event happens around 1990 and the other around 2004. Performing lagged regressions between properties shows similar variability around these events where cool AW causes greater winter sea ice extent, followed by increased sea ice melt. This fresh melt water causes the BSW volume minimum and in the more extreme case of 2005 the anomaly is extensive and resonates with an expansion in AW volume. Since AW temperature is driving most of the variability, a return to the pre-2005 regime could occur if AW temperature was anomalously cool for 2.5 to 3.5 years and sea ice expanded. Since 2003, the heat budget shows an imbalance of the AW heat inflow and the net surface heat flux. This shows the trend in AW temperature is being carried by the ocean out of the BSX suggesting further regime change could be possible.

5.2 Synthesis

This thesis has focused on the Barents Sea and the formation of Barents Sea Water within it to answer the overarching question : how does the seasonal sea ice impact ocean stratification and mean flow ? Each of the Chapters contributes a part to the puzzle and furthers the knowledge based on the climate variability in this region.

Sea ice can affect ocean dynamics by forming a layer between the ocean and the atmosphere reducing interactions between these fluid bodies. Sea ice forms from freezing sea water and over the lifetime of the sea ice, fractional freezing rejects the saline brine reducing the salt content of sea ice. The remaining sea ice can then melt in summer and release the relatively fresh water. This partitioning affects the stratification in the Arctic Ocean. Although loss of summer sea ice is well documented, the results of Onarheim and Årthun (2017) show the Barents Sea has lost winter sea ice. Our results in Chapter 2 show the loss of winter sea ice is important to the hydrodynamics. This is because the return of winter sea ice means there is a regular freshwater supply when it melts in summer. The seasonally melting sea ice is partitioned into ArW and BSW depending on where it melts. In both cases the freshwater release is an input of buoyancy. In ArW, the fresh melt-water maintains the persistent halocline that helps produce the cold sea water layer, a foundation for the following years sea ice (Lind et al., 2018). When winter sea ice is present above BSW, the heat contained in BSW is isolated from the surface reducing the thermal gradient. With average winter open water surface air temperature of -3°C (Jakowczyk and Stramska, 2014) and wind enhanced turbulent (sensible) heat flux, the air-sea thermal gradient for BSW with temperature $<2^{\circ}\text{C}$ is larger than the sea-ice thermal gradient where sea ice has a temperature of -1.8°C . Chapters 2 and 4 showed the variability in inflowing AW temperature caused sea ice extent variability which changed the surface area for ocean-atmosphere heat flux. The flexibility introduced by the sea ice layer neutralised temperature variability advected to BSW (Chapters 4 and 3). This regime was present until 2005 but the regime was time limited by the trend in AW temperature.

The decline in seasonal sea ice reduced the freshwater input to BSW resulting in an overall density increase (Chapter 2). Density changes in BSW have been suggested to change the velocity of BSW in St. Anna Trough (Dmitrenko et al., 2015; Smedsrud et al., 2013; Årthun et al., 2011). If this is the case, mass conservation would suggest greater transport through the Barents Sea Exit and Barents Sea Opening, a conclusion supported by the model output (Chapter 4). A change in the transport of BSW through St. Anna Trough could alter Eurasian Basin circulation. It has been shown that the Barents Sea is a source of potential vorticity to the Eurasian Basin (Karcher et al., 2007). The cascade of relatively dense water off a continental shelf, such as BSW transport in St. Anna Trough, induces potential vorticity via friction, developing eddies and resulting in along slope velocity (Yankovsky and Legg, 2019). It is this potential vorticity and induced Rossby Waves that control variability of transport in the Arctic Intermediate Water layer around the Eurasian basin’s shelf slope (Lique et al., 2015). Yang (2005) has shown that changes in the thickness or volume flux of an input to the Arctic Intermediate Water can affect circulation patterns by changing the net potential vorticity of the Arctic Basin.

The large amplitude of interannual variability in sea ice extent before the regime change (Herbaut et al., 2015; Onarheim and Årthun, 2017) suggests the pre-2005 regime became unstable (Chapter 4). This instability and break from the traditional pre-2005 regime is supported by the declining correlation between sea level pressure and sea ice extent after 1990 (Smedsrud et al., 2013) (Figure 5.2). Perhaps the volume anomaly in BSW that occurred in 1990 was the beginning of the delineation (Chapter 4). The sea level pressure induced variability in sea ice concentration identified between 1900 and 1998 shows sea ice deviating from the signal based prediction during the 1990s and it does not return to these patterns in the 2000s (Figure 5.2). This shows the 4 main signals in sea ice extent could not produce the 2005 sea ice decline suggesting the change was not natural variability induced.

With such a substantial impact on the properties and circulation, this regime change begs the question, what causes the main interannual variability in watermass properties since the reduction in forcing from sea level pressure and sea ice? Chapter 3 explores variability in observations of BSW properties after the 2005 regime change while Chapter 4 addresses this from a model perspective. Both studies show BSW temperature variability is primarily forced by local air-sea interaction. In the seasonal mixed layer, heat flux is important for seasonal stratification and heat content (Chapter 3). The interannual variability in AW temperature is also shown to be present in the SST EOF across the BSW region. The BSW temperature variability is correlated with wind stress curl suggesting Ekman pumping causes convergence of warm water and this signal combines with the AW temperature signal to produce BSW temperature (Chapter 4). Given that sea ice extent has declined, the variability in advected AW salinity becomes as important for BSW salinity as sea ice melt (Chapter 4).

5.3 Future Work

Future work following on from this thesis could focus on several important and unanswered questions that have been highlighted by this study. While undertaking the project in Chapter 2, the main problems encountered were in performing the EOF analysis. In theory, the trend and seasonality can be removed from the dataset before performing EOF analysis but SST contains a changing trend that could be part of variability at longer the time scales than those identified in Figure 5.2. Several attempts were made to remove the trend such as fitting a linear, polynomial or logistic function to the data. The trend removal techniques proved to produce their own problems since the same trend removal operation should be performed on the other parameters before regression analysis. The solution was to simplify the analysis and leave any trend in. This produced a more robust result since a trend at any time-scale could be part of an incomplete cycle in longer term variability. Figure 5.2 shows the natural variability in the Barents Sea at various time scales with the sea ice record covering the industrial period from 1850. While these observations are invaluable, there is room for work to conclusively determine if the regime change has anthropogenic forcing. This could be answered both by looking further

back in paleoceanographic samples, using models to simulate the climate variability at longer time scales than 150 years and by carrying out controlled model experiments with and without anthropogenic forcing.

The main challenge in Chapter 3 was finding why the theory with satellite data did not match the *in situ* observations. In theory, satellite steric height can be derived from ocean bottom pressure and sea surface height but simple regression could not correct the difference between the satellite steric height and the *in situ* steric height. After thoroughly testing the three data products (sea surface height, ocean bottom pressure and *in situ* steric height) against alternatives, it was concluded that there were no immediate systematic problems. As analysis showed, regression improved if only the upper part of the *in situ* data was integrated using a bi-modal regression model to produce the optimum satellite steric height. The method could be improved in two ways. First by weighting the regression model on time periods when hydrographic profiles are available to reduce the reliance on the EN4 climatology when there are gaps in hydrographic profiles. The dataset could also be improved by global expansion. Although it would not be suitable for in warmer regions or sea ice covered regions, it would extend the capability of sea surface salinity satellite data into cooler regions and perhaps could be refined to expand the range of temperatures it is suitable for.

The model presented challenges in Chapter 4 with how representative it is of observations. In this case comparisons are made between the model and observational data in both the temporal and spatial context relevant to the conclusions that are drawn. The model gives a simulation of condition that could have been present during that time based on the known physics. To validate the model, satellite data generally gives a 2-dimensional perspective of the surface but *in situ* measurements are needed for the water column and stratification. Mooring arrays such as the one across the BSO have been very useful and although the model suggests correlation between the BSO and BSX, it would be valuable for *in situ* observations at the BSX (or in St. Anna Trough) for comparison and to enable regularly monitor BSW properties.

Chapitre 6

Résumé Étendu en Français

6.1 Résumé

Le but de cette thèse est d'étudier la stratification et la circulation de l'Océan Arctique dans un contexte de changement de la couverture saisonnière de glace de mer. Ce questionnement est motivée par l'observation de changements affectant l'environnement Arctique. L'air à la surface du continent Arctique s'est réchauffée bien plus rapidement que la moyenne mondiale (Serreze et al., 2009; Screen and Simmonds, 2010a). Du fait de ces changements, il est important de comprendre la dynamique océanique afin d'améliorer les prédictions concernant le future de l'Arctique et les impacts possibles sur le climat aux plus basses latitudes. En particulier, il a été démontré qu'une diminution de la couverture de glace en mer de Barents entraînait des températures hivernales de l'air en surface anormalement froides en Europe et en Asie (Hoshi et al., 2019; Mori et al., 2014).

Cette thèse se concentre sur la Mer de Barents parce-que c'est une région de la zone marginale des glaces Arctique qui dispose d'une couverture de glace de mer saisonnière. Cela nous a permis d'étudier l'océan en présence de glace de mer tout en utilisant à des jeux de données issus d'observations historiques. Le Bassin Eurasién de l'Océan Arctique ainsi que la Mer de Barents sont tous les deux devenus plus chaud et plus salés, un phénomène connu sous le nom d' "Atlantification" (Polyakov et al., 2017; Årthun et al., 2012). Dans la mesure où la Mer de Barents produit également de l'Eau de la Mer de Barents (BSW pour "Barents Sea Water" en anglais), qui constitue en partie l'Eau Arctique Intermédiaire (AIW pour "Arctic Intermediate Water") (Karcher et al., 2011; Lique et al., 2010), il est important de comprendre les changements dans la dynamique océanique de cette région. Cette thèse a également permis de constater que l'Eau de la Mer de Barents est très mal connue, que ce soit sa formation ou son comportement face à des tendances à long terme.

Ce travail s'est attaché à répondre à la question suivante : comment la couverture saisonnière de glace de mer influence-t-elle la stratification océanique ainsi que la circulation océanique moyenne ? Pour répondre à cette question, nous l'avons abordé sous différents angles, chacun correspondant à un des trois chapitres suivant : Chapitres 2, 3 and 4.

- Le Chapitre 2 répond aux questions suivantes : où est localisé le Front Polaire dans l'Est de la Mer de Barents ? Quel est le lien entre la localisation du Front Polaire et celle de la limite de la banquise saisonnière ? et Qu'est ce que cela implique quant à la formation de BSW étant donné la diminution bien connue du volume de glace de mer et l'atlantification de la Mer de Barents ?
- Le Chapitre 3 répond à la question suivante : comment peut-on exploiter les données satellite pour obtenir des informations sur les variations des contenus en chaleur et en eau douce dans la colonne d'eau, et en particulier, pour mesurer la variabilité de l'Eau de la Mer de Barents (BSW) ?
- Le Chapitre 4 répond quant à lui aux questions suivantes : quelle est la cause de la variabilité du volume et des propriétés de l'Eau Atlantique (AW) et de l'Eau de la Mer de Barents (BSW) dans la partie centrale de la Mer de Barents ? Compte tenu du changement de régime de 2005, la dynamique océanique peut-elle contribuer à prédire si un changement de régime similaire ou opposé pourrait de nouveau se produire ?

Dans ce Chapitre, nous résumerons les trois chapitres principaux, mettant en avant les résultats originaux produits dans le cadre de cette thèse ; puis une synthèse suivra en Section 6.2 afin de répondre à la question principale, en Section 6.3 les méthodes utilisées seront évaluées et nous présenterons les futures travaux qui pourraient découler de cette thèse

6.1.1 Chapitre 2 : Atlantification observée dans la Mer de Barents

Le Chapitre 2 se concentre sur les observations du Front Polaire via des mesures par satellite de la température de surface de l'océan. Des études antérieures ont suggéré un large éventail de positions différentes du Front Polaire de la Mer de Barents, 600 km séparant la position estimée la plus au Nord de celle la plus au Sud (Smedsrud et al., 2010; Oziel et al., 2016). Ces estimations étaient basées sur deux définitions différentes du front, reposant soit sur un critère

en température, soit sur un critère en salinité. Il est important de localiser plus précisément ce front dans la mesure où c'est lui qui sépare les eaux stratifiées en température de celles stratifiées en salinité, et qui délimite la zone où une interaction directe entre océan, atmosphère et glace peut avoir lieu (Figure 6.1). Ces interactions jouent un rôle important dans la formation de l'Eau de la Mer de Barents (BSW), qui alimente les Eaux Arctiques intermédiaires (AIW) (Schauer et al., 1997; Maslowski et al., 2004). La taille de la zone délimitée par le Front Polaire aura une incidence sur la perte de chaleur par l'atmosphère et la variabilité de la glace de mer dans cette région, qui a été reliée à la variabilité des températures de l'air hivernales en Europe et en Asie (Hoshi et al., 2019; Mori et al., 2014).

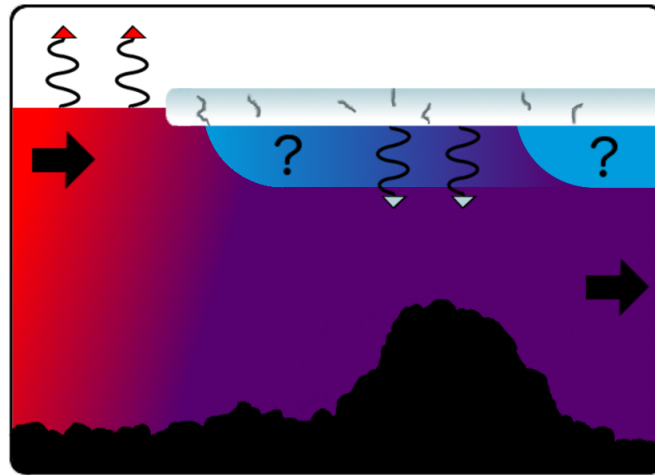


FIGURE 6.1 – Schéma du Front Polaire : les Eaux Arctiques (ArW) sont représentées en Bleu, les Eaux Atlantiques (AW) en rouge, les Eaux de la Mer de Barents (BSW) en violet. Le rectangle gris délimite la glace de mer. Les flèches rouges figurent un flux de chaleur de l'océan vers l'atmosphère, tandis que les flèches bleues indiquent un flux d'eau douce issu de la fonte de la banquise.

Nos résultats se sont attachés à localiser le front en calculant le gradient des données SST et en le comparant avec des climatologies de profils hydrographiques *in situ*. Cette méthode indique que le Front Polaire se trouve en moyenne le long d'une crête bathymétrique située près du Great Bank et de Ludlov Saddle à 76.5 °N. Il a été démontré que la SST de la Mer de Barents a connu une tendance au réchauffement qui a commencé dans l'Ouest de la Mer de Barents et s'est propagée jusqu'au Bassin Central. Une analyse en EOF (Empirical Orthogonal Functions) laisse penser que la variabilité de la SST est issue de la température de l'Eau Atlantique (AW) à l'entrée de la Mer de Barents (Barents Sea Opening, BSO) mais qu'elle influence aussi la température de l'air en surface dans l'Est de l'Arctique. Des études antérieures ont découvert que la variabilité naturelle de la température de l'AW était liée à la pression au niveau de la mer, mais l'analyse en EOF n'a montré aucune corrélation significative avec la pression au niveau de la mer et suggère que cette récente tendance au réchauffement dépasse le cadre de la variabilité naturelle de l'océan forcé par l'atmosphère. Cette tendance au réchauffement a entraîné une augmentation importante de la température de la BSW entre 1985 et 2004 et entre 2005 et 2016, limitant l'extension de la banquise hivernale au Sud du Front Polaire après 2005. L'Eau de la Mer de Barents (BSW) est par conséquent devenue notablement plus salée, en partie à cause d'une tendance positive de la salinité de l'Eau Atlantique (AW), mais aussi à cause de la diminution de la fonte de la banquise saisonnière. Ce changement de régime a été non-linéaire, passant d'un état climatique stable présent depuis au moins 1850 et lors duquel la banquise hivernale traversait le Front Polaire, à un nouveau système banquise (Figure 6.2).

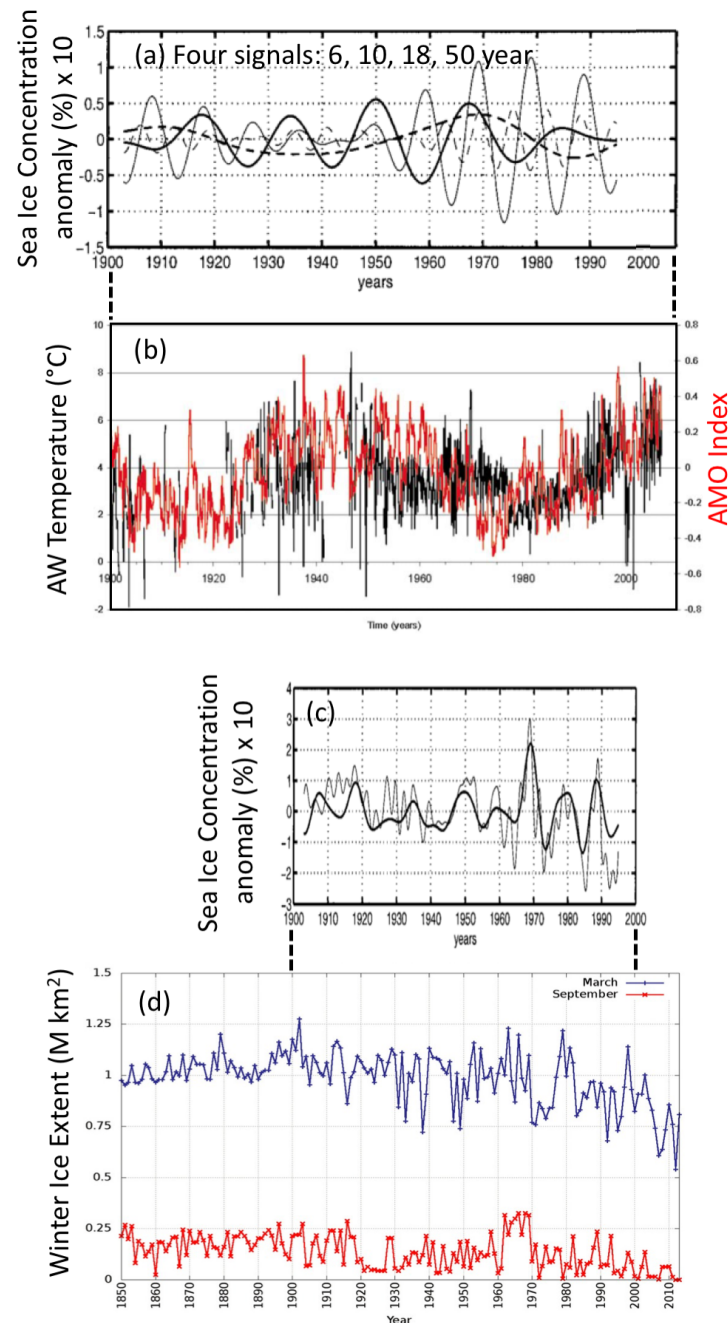


FIGURE 6.2 – Variabilité multi-décennale de la Mer de Barents : (a) les 4 composantes principales de la variabilité de la concentration en glace de mer dans la Mer de Barents entre 35 °E et 75 °E. (b) température de l'Eau Atlantique (AW) compilée à partir de profils hydrographiques à 100-150 m for 11 - 57 °E, 69 - 78 °N. Index de l'Oscillation Atlantique Multi-Décennale (AMO, Atlantic Multi-decadal Oscillation), définie par la SST dans l'Atlantique Nord à laquelle la tendance a été soustraite. (c) La courbe épaisse correspond à une concentration en glace de mer composite produite à partir des 4 composantes principales de (a), la ligne fine correspond aux observations de la concentration en glace de mer. (d) Extension de la banquise hivernale calculée sur une zone couvrant approximativement 15 - 65 °E et 67 - 78 °N, ces données sont issues d'observations faites à partir de navires puis interpolées. Ces figures sont des reproductions : (a) et (c) sont issues de [Venegas and Mysak \(2000\)](#), (b) est issue de [Levitus et al. \(2009\)](#), (d) est issue de [Walsh et al. \(2017\)](#).

6.1.2 Chapitre 3 : Caractéristiques des masses d'eau observées par satellite

Le Chapitre 3 vise principalement à élaborer une technique permettant d'extraire davantage d'informations des jeux de données satellites existants. Comme indiqué dans le Chapitre 2, la variabilité de la BSW influence grandement les caractéristiques des Eaux Arctiques Intermédiaies (AIW). Dans la Mer de Barents, il est possible d'observer par satellite l'Eau de la Mer de Barents (BSW) avant que celle-ci se retrouve isolée de la surface. La mer de Barents est une région où les eaux passent d'une stratification en température à une stratification en salinité (Carmack, 2007). On trouve dans cette zone, surtout en hiver, des températures de l'océan très faibles : les méthodes traditionnelles d'estimation de la salinité de surface de l'océan (SSS pour Sea Surface Salinity) par satellite sont dans ces conditions très sensibles à la variabilité de la température, les rendant inutilisables dans le cas présent. Nous avons développé une méthode pour estimer le contenu en eau douce et la SSS à partir d'observations par satellite : elle tire profit de la sensibilité réduite à la température de la densité (et de la hauteur stérique) aux faibles températures, renforçant la contribution de la salinité par rapport à celle de la température.

La méthode que nous proposons utilise à la fois des équations physiques et une régression statistique pour calculer une hauteur stérique, une hauteur thermostérique (proportionnelle au contenu thermique) et une hauteur halostérique (proportionnelle au contenu en eau douce) intégrées sur la verticale et représentative de la couche mélangée supérieure. Si l'on se focalise sur le Bassin Central dans lequel l'Eau de la Mer de Barents (BSW) est présente, notre jeu de données regroupant les caractéristiques des masses d'eau issues d'observation satellite présente un coefficient de régression avec des données *in situ* proche de 0.5. Notre jeu de données confirme également qu'une variation du contenu en eau douce et de la salinité a eu lieu en 2005, telle que décrite dans le Chapitre 2. L'analyse des flux atmosphériques suggère que la variabilité saisonnière de la hauteur stérique provient du réchauffement et du refroidissement nets de la surface. La variabilité interannuelle de la hauteur stérique trouve quant à elle son origine à la fois dans le contenu thermique et dans celui en eau douce, alors que la variabilité interannuelle du contenu d'eau douce n'est pas associée à des flux atmosphériques locaux, ce qui suggère des sources d'advection.

6.1.3 Chapitre 4 : Etude par modélisation de la variabilité de la Mer de Barents

Le Chapitre 4 s'intéresse de nouveau à la variabilité de la BSW et au changement de régime de 2005 identifié au Chapitre 2, mais en utilisant cette fois une méthodologie basée sur la modélisation. Cette méthode a l'avantage de pouvoir résoudre entièrement la variabilité interannuelle dans toute la Mer de Barents, contrairement aux profils hydrographiques *in situ* qui sont moins nombreux dans le nord et l'est de la Mer de Barents. Le changement de régime de 2005 est un événement important dans la mesure où de tels changements de régimes météorologiques pourraient s'étendre à d'autres régions. La température dans le Nord de la Mer de Barents a tendance à augmenter, alors même que cette dernière est corrélée à l'extension de la glace de mer (Lind et al., 2018) et, l'on prévoit qu'un réchauffement continu jusqu'en 2099 entraînerait une augmentation de la profondeur de convection dans le Bassin Eurasién (Lique and Thomas, 2018). En se penchant sur la dynamique du modèle utilisé, le Chapitre 4 s'attache à comprendre comment le changement s'est produit en s'intéressant à l'enchaînement des événements.

Sur la période de 1985 à 2015, le modèle indique que le volume de BSW dans la zone sud de la Mer de Barents a connu deux minima distincts. Un des événements s'est produit autour de 1990 tandis que le second a eu lieu vers 2004. Une analyse de régression avec retard nous indique que la variabilité était similaire autour de ces événements, avec une Eau Atlantique (AW) froide entraînant une plus grande extension de la banquise hivernale, suivie par une fonte accrue de la glace de mer. Cette eau douce issue de la fonte de la glace est ce qui fait que le volume de BSW atteint un minimum et, dans le cas de l'événement de 2005 (le plus extrême), cette anomalie est étendue et fait écho à une expansion du volume de l'Eau Atlantique (AW). Etant donné que la température de l'AW est à l'origine de la majeure partie de la variabilité, un retour au régime

pre-2005 pourrait avoir lieu si la température de l'AW était anormalement fraîche pendant 2.5 ou 3.5 années et si l'étendue de la banquise augmentait. Depuis 2003, le bilan thermique fait état d'un déséquilibre entre l'apport en chaleur de l'AW et le flux thermique net en surface. Tout cela montre que la tendance sur la température de l'AW est transportée par l'océan en dehors de la Mer de Barents suggérant que de nouveaux changements de régime soient possibles.

6.2 Synthèse

Cette thèse s'est concentrée sur l'étude de la Mer de Barents et de la formation de l'Eau de la Mer de Barents en son sein, afin de répondre à la question générale : comment la banquise saisonnière impacte-t-elle la stratification et la circulation moyenne de l'océan ? Chacun des chapitres apporte sa pièce au puzzle et permet d'enrichir les connaissances sur la variabilité climatique de cette région.

La glace de mer peut modifier la dynamique des océans lorsqu'elle forme une couche entre l'océan et l'atmosphère réduisant les interactions entre ces deux fluides. La glace de mer est créée par congélation de l'eau de mer. La congélation fractionnée de l'eau de mer s'accompagne d'un rejet de saumure dans l'océan, ce qui tend à diminuer le contenu en sel de la glace de mer. La glace de mer ainsi créée peut ensuite fondre en été et libérer à cette occasion de l'eau relativement douce. Ces deux mécanismes affectent la stratification de l'océan Arctique. Bien que la disparition de la banquise en été soit bien documentée, les résultats récents de [Onarheim and Årthun \(2017\)](#) montrent que la Mer de Barents perd également de la glace de mer en hiver. Dans le Chapitre 2, nos résultats montrent que cette perte de glace hivernale influe grandement sur l'hydrodynamique de la région. En effet, la présence de glace de mer en hiver implique un apport régulier en eau douce lorsque cette glace fond en été. L'eau issue de la fonte saisonnière de la banquise alimente soit l'Eau Arctique (ArW) soit l'Eau de la Mer de Barents (BSW), en fonction de l'endroit où se produit la fonte. Dans les deux cas, le rejet d'eau douce entraîne un apport de flottabilité. Dans l'Eau Arctique (ArW), l'eau douce de fonte entretient la halocline persistante qui participe à la production d'une couche d'eau froide, qui servira de base pour la formation de glace de mer les années suivantes ([Lind et al., 2018](#)). Quand la banquise hivernale surmonte l'Eau de la Mer de Barents, elle l'isole de la surface et réduit donc le gradient thermique entre les deux fluides. L'hiver, la température moyenne de l'air à la surface de l'océan libre est d'environ -3°C ([Jakowczyk and Stramska, 2014](#)) et le vent participe à accroître le flux thermique turbulent (sensible). Le gradient thermique air-mer (pour des températures de la BSW $< 2^{\circ}\text{C}$) est alors inférieur au gradient thermique mer-banquise (la glace de mer ayant des températures proches de -1.8°C). Dans les Chapitres 2 et 4, nous avons montré que la variabilité de la température de flux entrant d'AW provoquait une variabilité de l'étendue de la glace de mer, modifiant ainsi la surface disponible pour les échanges thermiques entre l'océan et l'atmosphère. La flexibilité introduite par la couche de glace de mer a neutralisé la variabilité de la température advectée vers la BSW (Chapitres 4 et 3). Ce régime était présent jusqu'en 2005, mais était limité dans le temps par la tendance en température de l'AW.

La réduction de la banquise saisonnière a entraîné une diminution de l'apport en eau douce vers la BSW, et ainsi globalement une augmentation de la densité (Chapitre 2). Certaines études ont suggéré que les changements de densité de la BSW pouvaient influencer sur la vitesse d'écoulement de la BSW à travers la fosse de Saint Anne ([Dmitrenko et al., 2015](#); [Smedsrud et al., 2013](#); [Årthun et al., 2011](#)). Si tel est bien le cas, la conservation de la masse suggérerait un transport plus important à travers l'entrée et la sortie de la Mer de Barents, une conclusion appuyée par nos sorties de modèle (Chapitre 4). Une modification du transport de la BSW par la Fosse de Sainte-Anne pourrait modifier la circulation dans le bassin eurasién. Il a été démontré que la Mer de Barents est une source de vorticit  potentielle pour le bassin eurasi n ([Karcher et al., 2007](#)). L' coulement d'une eau relativement dense le long du plateau continental, tel que le transport de la BSW   travers la fosse de Saint Anne, induit de la vorticit  potentielle par friction ce qui cr e des tourbillons et induit une vitesse le long du talus ([Yankovsky and Legg, 2019](#)). C'est cette vorticit  potentielle et les ondes de Rossby qu'elle d clenche qui contr le la variabilit  du transport

dans la couche d'Eau Arctique Intermédiaire autour du talus du bassin eurasién (Lique et al., 2015). Yang (2005) a montré que des changements de l'épaisseur ou du volume de l'apport vers l'Eau Arctique Intermédiaire pouvaient avoir un effet sur les régimes de circulation en modifiant la vorticit   potentielle totale du bassin Arctique.

La grande amplitude de la variabilit   interannuelle de l'  tendue de la glace de mer avant le changement de r  gime (Herbaut et al., 2015; Onarheim and   rthun, 2017) sugg  re que le r  gime pre-2005   tait devenu instable (Chapitre 4). Cette instabilit   et de l'interruption du r  gime pre-2005 sont appuy  es par la baisse de corr  lation entre la pression au niveau de la mer et l'  tendue de la glace de mer apr  s 1990 (Smedsrud et al., 2013) (Figure 6.2). Il est possible que l'anomalie de volume de la BSW ayant eu lieu en 1990 marque le d  but de la rupture de r  gime (Chapitre 4). La variabilit   de la concentration en glace de mer induite par les variations de pression au niveau de la mer, identifi  e entre 1990 et 1998, montre que le comportement de la glace de mer d  vie des pr  dictions lors des ann  es 1990 et ne suit de nouveau ces r  gimes que dans les ann  es 2000 (Figure 6.2). Tout cela montre que les quatres composantes principales de la variabilit   de l'  tendue en glace de mer (Figure 6.2) ne peuvent entra  ner une baisse comme celle ayant eu lieu en 2005, ce qui laisse    penser que ce changement n'a pas   t   induit par la variabilit   naturelle du syst  me.

Le changement de r  gime   voqu   pr  c  demment a un impact consid  rable sur les propri  t  s des masses d'eau et la circulation, ce qui soul  ve donc la question suivante : quelle est la cause de la variabilit   interannuelle principale des propri  t  s des masses d'eau    partir du moment o   le for  age d      la pression au niveau de la mer et    la glace de mer a diminu   ? Le Chapitre 3 s'int  resse    la variabilit   des propri  t  s observ  es de la BSW apr  s le changement de r  gime de 2005, tandis que le Chapitre 4 aborde cette question du point de vue du mod  le. Les deux   tudes montrent que la variabilit   de la temp  rature de la BSW est principalement forc  e par les interactions air-mer locales. Dans la couche de m  lange saisonni  re, les   changes thermiques r  gulent la stratification saisonni  re et le contenu thermique (Chapitre 3). On a   galement montr   qu'on retrouve la variabilit   interannuelle de la temp  rature de l'Eau Atlantique (AW) dans les EOF de la SST de la r  gion de la BSW. La variabilit   de la temp  rature de la BSW est corr  l  e au rotationnel de la tension du vent, ce qui sugg  re que le pompage d'Ekman entra  ne une convergence des eaux chaudes et que le signal correspondant s'ajoute    celui de la temp  rature de l'AW pour moduler la temp  rature de la BSW (Chapitre 4).   tant donn   la diminution de l'  tendue de la glace de mer, la variabilit   de la salinit   de l'advection d'AW devient aussi importante pour la salinit   de la BSW que la fonte de la glace de mer (Chapitre 4).

6.3 Perspectives

Les travaux qui feront suite    ce travail de th  se pourraient se concentrer sur plusieurs questions importantes et actuellement sans r  ponse, mises en   vidence par notre   tude. Lorsque nous avons r  alis   l'  tude d  crite dans le Chapitre 2, les principaux probl  mes auxquels nous avons   t   confront   sont li  s    l'analyse en EOF. En th  orie, la tendance et le signal saisonnier peuvent   tre soustraits du jeu de donn  es avant d'effectuer l'analyse en EOF. Mais le jeu de donn  e de SST contient une tendance variable qui pourrait faire partie de la variabilit      des   chelles de temps plus longues que celles identifi  es dans la Figure 6.2. Nous avons essay      plusieurs reprises d'  liminer cette tendances via plusieurs techniques telles qu'ajuster aux donn  es des fonctions lin  aire, des polyn  mes ou des fonctions logistiques. Les techniques de suppression des tendances se sont av  r  es causer leurs propres probl  mes puisque la m  me op  ration de suppression des tendances doit   tre effectu  e sur les autres param  tres avant d'effectuer la r  gression. La solution pour laquelle nous avons opt  e a   t   de simplifier l'analyse et de laisser toute tendance en place. Le r  sultat est alors plus robuste puisqu'une tendance    n'importe quelle   chelle de temps pourrait faire partie d'un cycle incomplet dans la variabilit      long terme. La Figure 6.2 pr  sente la variabilit   naturelle dans la Mer de Barents    diff  rentes   chelles de temps, les donn  es de glace de mer couvrent la p  riode industrielle    partir de 1850. Bien que ces observations soient pr  cieuses, il reste encore beaucoup    faire pour d  terminer de fa  on d  finitive si le changement

de régime à un forçage anthropique. On pourrait par exemple tenter de répondre à cette interrogation par deux moyens : soit en regardant plus en arrière grâce à l'étude d'échantillons paléo-océanographiques, soit en utilisant des modèles numériques pour simuler la variabilité du climat à des échelles de temps plus longues que 150 ans, en effectuant des simulations contrôlées incluant ou non un forçage anthropique.

Le principal défi du Chapitre 3 était de trouver pourquoi la théorie concernant les données satellitaires ne concordait pas avec les observations *in situ*. Théoriquement, la hauteur stérique peut être calculée à partir de la pression au fond de l'océan et du niveau de la mer (hauteur de la surface de la mer) mesurée par satellite. Mais cette hauteur stérique calculée à partir de mesures satellites et la hauteur stérique *in situ* présentent des différences qu'une simple régression ne nous a pas permis de corriger. Nous avons soigneusement testé les trois produits de données (hauteur de la surface de la mer, pression du fond de l'océan et hauteur textuelle *in situ*) à des, et avons conclu qu'il n'y avait pas de problème systématique dans l'immédiat. Nos analyses ont montré qu'une régression améliorerait les choses si seule la partie supérieure des données *in situ* était intégré via une régression bi-modale pour générer une hauteur stérique optimale issue des données satellites. La méthode pourrait être améliorée de deux façons. Tout d'abord, en accordant plus de poids dans le modèle de régression où périodes auxquelles les profils hydrographiques sont disponibles, ce afin de faire en sorte que la régression soit moins dépendante de la climatologie du jeu de données EN4 lorsqu'il y a des trous dans les données. Le jeu de données pourrait également devenir plus pertinent en étant étendu à d'autres régions du monde. Bien qu'il ne serait pas adapté aux régions chaudes ou aux régions couvertes par la glace de mer, cela permettrait d'étendre le domaine d'application des satellite mesurant la salinité aux régions plus froides mais également d'augmenter la gamme de température auxquelles la méthode est adaptée.

Nous avons fait face à plusieurs difficultés avec le modèle présenté dans le Chapitre 4, notamment dans sa capacité à être représentatif vis-à-vis des observations. Nous avons donc effectué des comparaisons entre le modèle et les données issues d'observations, dans les domaines spatial et temporel et sur des plages et zones pertinentes pour notre étude. Le modèle simule un état possible du système à une période de temps donnée en fonction de ce que l'on connaît de la physique du dit système. Pour valider le modèle, on utilise des données issues d'observations : si les données satellite permettent généralement d'avoir un point de vue à deux dimensions de la surface, on a besoin de mesures *in situ* pour accéder à des informations sur la colonne d'eau, notamment la stratification. Les réseaux de mouillages tels que ceux installés dans la région de l'Entrée de la Mer de Barents (Barents Sea Opening, BSO) se sont révélés très utiles et, bien que le modèle suggère une corrélation entre l'Entrée de la Mer de Barents (BSO) et la Sortie de la Mer de Barents (BSX), il serait utile d'installer des mouillages en Sortie de Mer de Barents (BSX) (ou dans la fosse de Saint Anne) à des fins de comparaison et pour permettre de surveiller régulièrement les propriétés de la BSW.

Bibliographie

- K. Aagaard and R. A. Woodgate. Some thoughts on the freezing and melting of sea ice and their effects on the ocean. *Ocean Modelling*, 3(1-2) :127–135, 2001. ISSN 14635003. doi : 10.1016/S1463-5003(01)00005-1.
- K. Aagaard, J. H. Swift, and E. C. Carmack. Thermohaline circulation in the Arctic Mediterranean Seas. *Journal of Geophysical Research*, 90(C3) :4833, 1985. ISSN 0148-0227. doi : 10.1029/JC090iC03p04833. URL <http://doi.wiley.com/10.1029/JC090iC03p04833>.
- Y. Aksenov, S. Bacon, A. C. Coward, and A. J. G. Nurser. The North Atlantic inflow to the Arctic Ocean : High-resolution model study. *Journal of Marine Systems*, 79(1-2) :1–22, 2010. ISSN 09247963. doi : 10.1016/j.jmarsys.2009.05.003. URL <http://dx.doi.org/10.1016/j.jmarsys.2009.05.003>.
- Y. I. Aleksandrov, N. N. Bryazgin, E. J. Førland, V. F. Radionov, and P. N. Svyashchennikov. Seasonal, interannual and long-term variability of precipitation and snow depth in the region of the Barents and Kara seas. *Polar Research*, 24(1-2) :69–85, 2005. ISSN 08000395. doi : 10.3402/polar.v24i1.6254.
- M. H. Ambaum, B. J. Hoskins, and D. B. Stephenson. Arctic Oscillation or North Atlantic Oscillation? *Journal of Climate*, 14(16) :3495–3507, 2001. ISSN 08948755. doi : 10.1175/1520-0442(2001)014<3495:AOONAO>2.0.CO;2.
- M. Ardyna, M. Babin, M. Gosselin, E. Devred, S. Bélanger, A. Matsuoka, and J. E. Tremblay. Parameterization of vertical chlorophyll a in the Arctic Ocean : Impact of the subsurface chlorophyll maximum on regional, seasonal, and annual primary production estimates. *Bio-geosciences*, 10(6) :4383–4404, 2013. ISSN 17264170. doi : 10.5194/bg-10-4383-2013.
- T. W. K. Armitage, S. Bacon, A. L. Ridout, S. F. Thomas, Y. Aksenov, and D. J. Wingham. Arctic sea surface height variability and change from satellite radar altimetry and GRACE, 2003–2014. *Journal of Geophysical Research : Oceans*, 121 :4303–4322, 2016. ISSN 21699275. doi : 10.1002/2015JC011579.
- T. W. K. Armitage, S. Bacon, A. L. Ridout, A. A. Petty, S. Wolbach, and M. Tsamados. Arctic Ocean surface geostrophic circulation 2003-2014. *The Cryosphere*, 11(4) :1767–1780, 2017. ISSN 1994-0424. doi : 10.5194/tc-11-1767-2017. URL <https://www.the-cryosphere.net/11/1767/2017/>.
- K. R. Arrigo and G. L. Van Dijken. Secular trends in Arctic Ocean net primary production. *Journal of Geophysical Research : Oceans*, 116(9) :1–15, 2011. ISSN 21699291. doi : 10.1029/2011JC007151. URL <http://dx.doi.org/10.1029/2011JC007151>;doi:10.102.
- M. Årthun and T. Eldevik. On anomalous ocean heat transport toward the Arctic and associated climate predictability. *Journal of Climate*, 29(2) :689–704, 2016. ISSN 08948755. doi : 10.1175/JCLI-D-15-0448.1.
- M. Årthun and C. Schrum. Ocean surface heat flux variability in the Barents Sea. *Journal of Marine Systems*, 83(1-2) :88–98, 2010. ISSN 09247963. doi : 10.1016/j.jmarsys.2010.07.003. URL <http://dx.doi.org/10.1016/j.jmarsys.2010.07.003>.

- M. Årthun, R. B. Ingvaldsen, L. H. Smedsrud, and C. Schrum. Dense water formation and circulation in the Barents Sea. *Deep-Sea Research Part I : Oceanographic Research Papers*, 58 (8) :801–817, 2011. ISSN 09670637. doi : 10.1016/j.dsr.2011.06.001.
- M. Årthun, T. Eldevik, L. H. Smedsrud, Ø. Skagseth, and R. B. Ingvaldsen. Quantifying the influence of atlantic heat on barents sea ice variability and retreat. *Journal of Climate*, 25 (13) :4736–4743, 2012. ISSN 08948755. doi : 10.1175/JCLI-D-11-00466.1.
- M. Årthun, B. Bogstad, U. Daewel, N. S. Keenlyside, A. B. Sandø, C. Schrum, and G. Ottersen. Climate based multi-year predictions of the Barents Sea cod stock. *PLoS ONE*, 13(10) :1–13, 2018. ISSN 19326203. doi : 10.1371/journal.pone.0206319.
- M. Arthun, T. Eldevik, and L. H. Smedsrud. The role of Atlantic heat transport in future Arctic winter sea ice loss. *Journal of Climate*, 2019. doi : 10.1175/JCLI-D-18-0750.1.
- B. Barnier, G. Madec, T. Penduff, J. M. Molines, A. M. Treguier, J. Le Sommer, A. Beckmann, A. Biastoch, C. Böning, J. Dengg, C. Derval, E. Durand, S. Gulev, E. Remy, C. Talandier, S. Theetten, M. Maltrud, J. McClean, and B. De Cuevas. Impact of partial steps and momentum advection schemes in a global ocean circulation model at eddy-permitting resolution. *Ocean Dynamics*, 56(5-6) :543–567, 2006. ISSN 16167341. doi : 10.1007/s10236-006-0082-1.
- B. I. Barton, Y.-D. Lenn, and C. Lique. Observed atlantification of the Barents Sea Polar Front limits the expansion of winter sea ice. *Journal of Physical Oceanography*, 48 :1849–1866, 2018. ISSN 0022-3670. doi : 10.1175/JPO-D-18-0003.1. URL <http://journals.ametsoc.org/doi/10.1175/JPO-D-18-0003.1>.
- T. Bernauer and T. Siegfried. Climate change and international water conflict in Central Asia. *Journal of Peace Research*, 49(1) :227–239, 2012. ISSN 00223433. doi : 10.1177/0022343311425843.
- P. Berrisford, D. Dee, K. Fielding, M. Fuentes, P. Kallberg, S. Kobayashi, and S. Uppala. The ERA-Interim Archive : Version 2.0. *ERA report series*, 2(1) :1–16, 2011.
- R. Bintanja and O. Andry. Towards a rain-dominated Arctic. *Nature Climate Change*, 7(4) :263–267, 2017. ISSN 17586798. doi : 10.1038/nclimate3240.
- R. Blackport, J. A. Screen, K. van der Wiel, and R. Bintanja. Minimal influence of reduced Arctic sea ice on coincident cold winters in mid-latitudes. *Nature Climate Change*, pages 1–9, 2019. ISSN 1758-678X. doi : 10.1038/s41558-019-0551-4. URL <http://www.nature.com/articles/s41558-019-0551-4>.
- Y. A. Bochkov. Water temperature in the 0-200 m layer in the Kola-Meridian section in the Barents Sea, 1900-1981. *Trudy PINRO, Murmansk*, 46 :113–122, 1982.
- V. D. Boitsov, A. L. Karsakov, and A. G. Trofimov. Atlantic water temperature and climate in the Barents Sea, 2000–2009. *ICES Journal of Marine Science*, 69(5) :833–840, 2012. ISSN 1206616369. doi : 10.1093/icesjms/fst075.
- L. Brodeau, B. Barnier, A. M. Treguier, T. Penduff, and S. Gulev. An ERA40-based atmospheric forcing for global ocean circulation models. *Ocean Modelling*, 31(3-4) :88–104, 2010. ISSN 14635003. doi : 10.1016/j.ocemod.2009.10.005. URL <http://dx.doi.org/10.1016/j.ocemod.2009.10.005>.
- E. C. Carmack. The alpha/beta ocean distinction : A perspective on freshwater fluxes, convection, nutrients and productivity in high-latitude seas. *Deep-Sea Research Part II : Topical Studies in Oceanography*, 54(23-26) :2578–2598, 2007. ISSN 09670645. doi : 10.1016/j.dsr2.2007.08.018.

- E. C. Carmack, K. Aagaard, J. H. Swift, R. W. Macdonald, F. A. McLaughlin, E. P. Jones, R. G. Perkin, J. N. Smith, K. M. Ellis, and L. R. Killiush. Changes in temperature and tracer distributions within the Arctic Ocean : Results from the 1994 Arctic Ocean section. *Deep-Sea Research Part II : Topical Studies in Oceanography*, 44(8) :1487–1502, 1997. ISSN 09670645. doi : 10.1016/S0967-0645(97)00056-8.
- L. Chafik, J. Nilsson, Ø. Skagseth, and P. Lundberg. On the flow of Atlantic water and temperature anomalies in the Nordic Seas toward the Arctic Ocean. *Journal of Geophysical Research : Oceans*, 120 :7897–7918, 2015. ISSN 21699275. doi : 10.1002/2015JC011012.Received.
- D. P. Chambers and J. A. Bonin. Evaluation of Release-05 GRACE time-variable gravity coefficients over the ocean. *Ocean Science*, 8(5) :859–868, 2012. ISSN 18120784. doi : 10.5194/os-8-859-2012.
- D. P. Chambers and J. K. Willis. A global evaluation of ocean bottom pressure from GRACE, OMCT, and steric-corrected altimetry. *Journal of Atmospheric and Oceanic Technology*, 27 (8) :1395–1402, 2010. ISSN 07390572. doi : 10.1175/2010JTECHO738.1.
- G. A. Chepurin and J. A. Carton. Subarctic and Arctic sea surface temperature and its relation to ocean heat content 1982-2010. *Journal of Geophysical Research : Oceans*, 117(6) :1–12, 2012. ISSN 21699291. doi : 10.1029/2011JC007770.
- J. Cohen, J. A. Screen, J. C. Furtado, M. Barlow, D. Whittleston, D. Coumou, J. Francis, K. Dethloff, D. Entekhabi, J. Overland, and J. Jones. Recent Arctic amplification and extreme mid-latitude weather. *Nature Geoscience*, 7(9) :627–637, 2014. ISSN 17520908. doi : 10.1038/ngeo2234. URL <http://dx.doi.org/10.1038/ngeo2234>.
- R. Dankers and H. Middelkoop. River discharge and freshwater runoff to the Barents Sea under present and future climate conditions. *Climatic Change*, 87(1-2) :131–153, 2008. ISSN 01650009. doi : 10.1007/s10584-007-9349-x.
- J. J. Day, S. Tietsche, and E. Hawkins. Pan-arctic and regional sea ice predictability : Initialization month dependence. *Journal of Climate*, 27(12) :4371–4390, 2014. ISSN 08948755. doi : 10.1175/JCLI-D-13-00614.1.
- C. de Lavergne, S. Falahat, G. Madec, F. Roquet, J. Nycander, and C. Vic. Toward global maps of internal tide energy sinks. *Ocean Modelling*, 137(March) :52–75, 2019. ISSN 14635003. doi : 10.1016/j.ocemod.2019.03.010. URL <https://doi.org/10.1016/j.ocemod.2019.03.010>.
- S. R. Dewey, J. H. Morison, and J. Zhang. An Edge-Referenced Surface Fresh Layer in the Beaufort Sea Seasonal Ice Zone. *Journal of Physical Oceanography*, 47(5) :1125–1144, 2017. ISSN 0022-3670. doi : 10.1175/JPO-D-16-0158.1. URL <http://journals.ametsoc.org/doi/10.1175/JPO-D-16-0158.1>.
- R. R. Dickson, J. Meincke, S. A. Malmberg, and A. J. Lee. The "great salinity anomaly" in the Northern North Atlantic 1968-1982. *Progress in Oceanography*, 20(2) :103–151, 1988. ISSN 00796611. doi : 10.1016/0079-6611(88)90049-3.
- Y. Ding, J. A. Carton, G. A. Chepurin, M. Steele, and S. Hakkinen. Seasonal heat and freshwater cycles in the Arctic Ocean in CMIP5 coupled models. *Journal of Geophysical Research : Oceans*, 121 :2043–2057, 2016. ISSN 21699275. doi : 10.1002/2015JC011534.Received.
- I. A. Dmitrenko, S. A. Kirillov, N. Serra, N. V. Koldunov, V. V. Ivanov, U. Schauer, I. V. Polyakov, D. Barber, M. Janout, V. S. Lien, M. Makhotin, and Y. Aksenov. Heat loss from the Atlantic water layer in the northern Kara Sea : Causes and consequences. *Ocean Science*, 10(4) :719–730, 2014. ISSN 18120792. doi : 10.5194/os-10-719-2014.

- I. A. Dmitrenko, B. Rudels, S. A. Kirillov, Y. O. Aksenov, V. S. Lien, V. V. Ivanov, U. Schauer, I. V. Polyakov, A. Coward, and B. D. G. Atlantic water flow into the Arctic Ocean through the St. Anna Trough in the northern Kara Sea. *Journal of Geophysical Research : Oceans*, 120 :5158– 5178, 2015. ISSN 21699275. doi : 10.1002/2015JC010969.
- M. G. Donat, G. C. Leckebusch, J. G. Pinto, and U. Ulbrich. Examination of wind storms over Central Europe with respect to circulation weather types and NAO phases. *International Journal of Climatology*, 30(9) :1289–1300, 2010. ISSN 08998418. doi : 10.1002/joc.1982.
- C. J. Donlon, M. Martin, J. Stark, J. Roberts-Jones, E. Fiedler, and W. Wimmer. The Operational Sea Surface Temperature and Sea Ice Analysis (OSTIA) system. *Remote Sensing of Environment*, 116 :140–158, 2012. ISSN 00344257. doi : 10.1016/j.rse.2010.10.017. URL <http://dx.doi.org/10.1016/j.rse.2010.10.017>.
- F. Dupont, S. Higginson, R. Bourdall  -Badie, Y. Lu, F. Roy, G. C. Smith, J. F. Lemieux, G. Gar  ric, and F. Davidson. A high-resolution ocean and sea-ice modelling system for the Arctic and North Atlantic oceans. *Geoscientific Model Development*, 8(5) :1577–1594, 2015. ISSN 19919603. doi : 10.5194/gmd-8-1577-2015.
- H. Eicken. Arctic sea ice needs better forecasts. *Nature*, 497(7450) :431–433, 2013. ISSN 0028-0836. doi : 10.1038/497431a.
- I. Ellingsen, D. Slagstad, and A. Sundfjord. Modification of water masses in the Barents Sea and its coupling to ice dynamics : A model study. *Ocean Dynamics*, 59(6) :1095–1108, 2009. ISSN 16167341. doi : 10.1007/s10236-009-0230-5.
- E. Eriksen, B. Bogstad, and O. Nakken. Ecological significance of 0-group fish in the Barents Sea ecosystem. *Polar Biology*, 34(5) :647–657, 2011. ISSN 07224060. doi : 10.1007/s00300-010-0920-y.
- E. Fahrbach, J. Meincke, S.   sterhus, G. Rohardt, U. Schauer, V. Tverberg, J. Verduin, and R. a. Woodgate. Direct measurements of heat and mass transports through the Fram Strait. *Polar Research*, 20(2) :217–224, 2001. ISSN 0800-0395. doi : 10.1111/j.1751-8369.2001.tb00059.x.
- I. Fer and K. Drinkwater. Mixing in the Barents Sea Polar Front near Hopen in spring. *Journal of Marine Systems*, 130 :206–218, 2014. ISSN 09247963. doi : 10.1016/j.jmarsys.2012.01.005. URL <http://dx.doi.org/10.1016/j.jmarsys.2012.01.005>.
- T. Gammelsr  d,   . Leikvin, V. Lien, W. P. Budgell, H. Loeng, and W. Maslowski. Mass and heat transports in the NE Barents Sea : Observations and models. *Journal of Marine Systems*, 75(1-2) :56–69, 2009. ISSN 09247963. doi : 10.1016/j.jmarsys.2008.07.010. URL <http://dx.doi.org/10.1016/j.jmarsys.2008.07.010>.
- G. Gawarkiewicz and A. J. Plueddemann. Topographic control of thermohaline frontal structure in the Barents Sea Polar Front on the south flank of Spitsbergen Bank. *Journal of Geophysical Research*, 100(C3) :4509–4524, 1995.
- S. Gerland, A. H. H. Renner, F. Godtli  bsen, D. Divine, and T. B. L  yning. Decrease of sea ice thickness at Hopen, Barents Sea, during 1966-2007. *Geophysical Research Letters*, 35(6) :1–5, 2008. ISSN 00948276. doi : 10.1029/2007GL032716.
- D. Giglio, D. Roemmich, and B. Cornuelle. Understanding the annual cycle in global steric height. *Geophysical Research Letters*, 40(16) :4349–4354, 2013. ISSN 00948276. doi : 10.1002/grl.50774.
- K. A. Giles, S. W. Laxon, A. L. Ridout, D. J. Wingham, and S. Bacon. Western Arctic Ocean freshwater storage increased by wind-driven spin-up of the Beaufort Gyre. *Nature Geoscience*, 5(3) :194–197, 2012. ISSN 17520894. doi : 10.1038/ngeo1379. URL <http://dx.doi.org/10.1038/ngeo1379>.

- A. E. Gill and P. P. Niiler. The theory of the seasonal variability in the ocean. *Deep-Sea Research and Oceanographic Abstracts*, 20(2) :141–177, 1973. ISSN 00117471. doi : 10.1016/0011-7471(73)90049-1.
- L. C. Gillard, X. Hu, P. G. Myers, and J. L. Bamber. Meltwater pathways from marine terminating glaciers of the Greenland ice sheet. *Geophysical Research Letters*, 43(20) :10,873–10,882, 2016. ISSN 19448007. doi : 10.1002/2016GL070969.
- T. Gong and D. Luo. Ural blocking as an amplifier of the Arctic sea ice decline in winter. *Journal of Climate*, 30(7) :2639–2654, 2017. ISSN 08948755. doi : 10.1175/JCLI-D-16-0548.1.
- S. A. Good, M. J. Martin, and N. A. Rayner. EN4 : Quality controlled ocean temperature and salinity profiles and monthly objective analyses with uncertainty estimates. *Journal of Geophysical Research : Oceans*, 118(12) :6704–6716, 2013. ISSN 21699291. doi : 10.1002/2013JC009067.
- V. Gouretski and F. Reseghetti. On depth and temperature biases in bathythermograph data : Development of a new correction scheme based on analysis of a global ocean database. *Deep-Sea Research Part I : Oceanographic Research Papers*, 57(6) :812–833, 2010. ISSN 09670637. doi : 10.1016/j.dsr.2010.03.011. URL <http://dx.doi.org/10.1016/j.dsr.2010.03.011>.
- C. L. Harris, A. J. Plueddemann, and G. G. Gawarkiewicz. Water mass distribution and polar front structure in the western Barents Sea. *Journal of Geophysical Research*, 103(C2) :2905–2917, 1998.
- C. Herbaut, M.-N. Houssais, S. Close, and A.-C. Blaizot. Two wind-driven modes of winter sea ice variability in the Barents Sea. *Deep-Sea Research Part I : Oceanographic Research Papers*, 106 :97–115, 2015. ISSN 09670637. doi : 10.1016/j.dsr.2015.10.005. URL <http://dx.doi.org/10.1016/j.dsr.2015.10.005>.
- K. Hoshi, J. Ukita, M. Honda, T. Nakamura, K. Yamazaki, Y. Miyoshi, and R. Jaiser. Weak stratospheric polar vortex events modulated by the Arctic sea ice loss. *Journal of Geophysical Research : Atmospheres*, 124 :858–869, 2019. ISSN 2169897X. doi : 10.1029/2018JD029222. URL <http://doi.wiley.com/10.1029/2018JD029222>.
- J. W. Hurrell and H. Van Loon. Decadal variations in climate associated with the North Atlantic Oscillation. *Climatic Change at High Elevation Sites*, 36(3-4) :301–326, 1997. ISSN 0165-0009. doi : 10.1023/a:1005314315270.
- R. B. Ingvaldsen. Width of the North Cape Current and location of the Polar Front in the western Barents Sea. *Geophysical Research Letters*, 32(16) :1–4, 2005. ISSN 00948276. doi : 10.1029/2005GL023440.
- R. B. Ingvaldsen, H. Loeng, O. Geir, and A. Bjorn. Climate variability in the Barents Sea during the 20th century with a focus on the 1990s. *ICES Journal of Marine Science*, pages 160–168, 2003. URL <http://www.ices.dk/sites/pub/PublicationReports/MarineScienceSymposia/Phase2/ICESMarineScienceSymposia-Volume219-2003-Part20of75.pdf>.
- R. B. Ingvaldsen, L. Asplin, and H. Loeng. Velocity field of the western entrance to the Barents Sea. *J. Geophys. Res.*, 109(C3) :1–12, 2004a. ISSN 0148-0227. doi : 10.1029/2003JC001811. URL [10.1029/2003JC001811](http://doi.org/10.1029/2003JC001811).
- R. B. Ingvaldsen, L. Asplin, and H. Loeng. The seasonal cycle in the Atlantic transport to the Barents Sea during the years 1997-2001. *Continental Shelf Research*, 24(9) :1015–1032, 2004b. ISSN 02784343. doi : 10.1016/j.csr.2004.02.011.

- J. Inoue, M. E. Hori, and K. Takaya. The role of barents sea ice in the wintertime cyclone track and emergence of a warm-Arctic cold-Siberian anomaly. *Journal of Climate*, 25(7) :2561–2569, 2012. ISSN 08948755. doi : 10.1175/JCLI-D-11-00449.1.
- V. Ivanov, V. Alexeev, N. V. Koldunov, I. Repina, A. B. Sandø, L. H. Smedsrud, and A. Smirnov. Arctic Ocean Heat Impact on Regional Ice Decay : A Suggested Positive Feedback. *Journal of Physical Oceanography*, 46(5) :1437–1456, 2016. ISSN 0022-3670. doi : 10.1175/JPO-D-15-0144.1. URL <http://journals.ametsoc.org/doi/abs/10.1175/JPO-D-15-0144.1> <http://journals.ametsoc.org/doi/10.1175/JPO-D-15-0144.1>.
- V. V. Ivanov and G. I. Shapiro. Formation of a dense water cascade in the marginal ice zone in the Barents Sea. *Deep-Sea Research Part I : Oceanographic Research Papers*, 52(9) :1699–1717, 2005. ISSN 09670637. doi : 10.1016/j.dsr.2005.04.004.
- M. Jakowczyk and M. Stramska. Spatial and temporal variability of satellite-derived sea surface temperature in the Barents Sea. *International Journal of Remote Sensing*, 35(17) :6545–6560, 2014. ISSN 13665901. doi : 10.1080/01431161.2014.958247. URL <http://dx.doi.org/10.1080/01431161.2014.958247>.
- O. M. Johannessen and L. A. Foaster. A Note on the Topographically Controlled Oceanic Polar Front in the Barents Sea. *Journal of Geophysical Research*, 83(C9) :4567 – 4571, 1978.
- S. Kaltin, L. G. Anderson, K. Olsson, A. Fransson, and M. Chierici. Uptake of atmospheric carbon dioxide in the Barents Sea. *Journal of Marine Systems*, 38(1-2) :31–45, 2002. ISSN 09247963. doi : 10.1016/S0924-7963(02)00168-9.
- L. H. Kantha and C. A. Clayson. An improved mixed layer model for geophysical applications. *Journal of Geophysical Research*, 99(C12) :25235–25266, 1994. URL <https://doi.org/10.1029/94JC02257>.
- M. Karcher, F. Kauker, R. Gerdes, E. Hunke, and J. Zhang. On the dynamics of Atlantic Water circulation in the Arctic Ocean. *Journal of Geophysical Research : Oceans*, 112(C04S02) :1–19, 2007. ISSN 21699291. doi : 10.1029/2006JC003734.
- M. Karcher, A. Beszczynska-Möller, F. Kauker, R. Gerdes, S. Heyen, B. Rudels, and U. Schauer. Arctic Ocean warming and its consequences for the Denmark Strait overflow. *Journal of Geophysical Research : Oceans*, 116(C02037) :1–10, 2011. ISSN 21699291. doi : 10.1029/2010JC006265.
- T. Koenigk, U. Mikolajewicz, J. H. Jungclaus, and A. Kroll. Sea ice in the Barents Sea : Seasonal to interannual variability and climate feedbacks in a global coupled model. *Climate Dynamics*, 32(7-8) :1119–1138, 2009. ISSN 09307575. doi : 10.1007/s00382-008-0450-2.
- R. Kwok. Outflow of Arctic Ocean Sea Ice into the Greenland and Barents Seas : 1979–2007. *Journal of Climate*, 22(9) :2438–2457, 2009. ISSN 0894-8755. doi : 10.1175/2008JCLI2819.1.
- R. Kwok, W. Maslowski, and S. W. Laxon. On large outflows of Arctic sea ice into the Barents Sea. *Geophysical Research Letters*, 32(22) :1–5, 2005. ISSN 00948276. doi : 10.1029/2005GL024485.
- K. M. H. Larsen, C. Gonzalez-Pola, P. Fratantoni, A. Beszczynska-Möller, and S. L. E. Hughes. ICES Report on Ocean Climate 2015. *ICES Cooperative Research Report*, 331(May) :1–79, 2016.
- S. Laxon. Sea ice altimeter processing scheme at EODC. *International Journal of Remote Sensing*, 15(4) :915–924, 1994.
- S. Levitus, G. Matishov, D. Seidov, and I. Smolyar. Barents Sea multidecadal variability. *Geophysical Research Letters*, 36(19) :1–5, 2009. ISSN 00948276. doi : 10.1029/2009GL039847.

- F. Li and H. Wang. Autumn sea ice cover, winter northern hemisphere annular mode, and winter precipitation in Eurasia. *Journal of Climate*, 26(11) :3968–3981, 2013. ISSN 08948755. doi : 10.1175/JCLI-D-12-00380.1.
- S. Li and T. A. McClimans. The effects of winds over a barotropic retrograde slope current. *Continental Shelf Research*, 18(5) :457–485, 1998. ISSN 02784343. doi : 10.1016/S0278-4343(97)00077-0.
- V. S. Lien, F. B. Vikebø, and Ø. Skagseth. One mechanism contributing to co-variability of the Atlantic inflow branches to the Arctic. *Nature Communications*, 4 :1–6, 2013. ISSN 20411723. doi : 10.1038/ncomms2505.
- V. S. Lien, P. Schlichtholz, Ø. Skagseth, and F. B. Vikebø. Wind-Driven Atlantic Water Flow as a Direct Mode for Reduced Barents Sea Ice Cover. *Journal of Climate*, 30(2) :803–812, 2017. ISSN 0894-8755. doi : 10.1175/JCLI-D-16-0025.1.
- S. Lind and R. B. Ingvaldsen. Variability and impacts of Atlantic Water entering the Barents Sea from the north. *Deep-Sea Research Part I : Oceanographic Research Papers*, 62 :70–88, 2012. ISSN 09670637. doi : 10.1016/j.dsr.2011.12.007.
- S. Lind, R. B. Ingvaldsen, and T. Furevik. Arctic layer salinity controls heat loss from deep Atlantic layer in seasonally ice-covered areas of the Barents Sea. *Geophysical Research Letters*, 43(10) :5233–5242, 2016. ISSN 19448007. doi : 10.1002/2016GL068421.
- S. Lind, R. B. Ingvaldsen, and T. Furevik. Arctic warming hotspot in the northern Barents Sea linked to declining sea-ice import. *Nature Climate Change*, 8 :634–639, 2018. ISSN 1758-6798. doi : 10.1038/s41558-018-0205-y. URL <http://dx.doi.org/10.1038/s41558-018-0205-y>.
- C. Lique and M. Steele. Seasonal to decadal variability of Arctic Ocean heat content : A model-based analysis and implications for autonomous observing systems. *Journal of Geophysical Research : Oceans*, 118(4) :1673–1695, 2013. ISSN 21699291. doi : 10.1002/jgrc.20127.
- C. Lique and M. D. Thomas. Latitudinal shift of the Atlantic Meridional Overturning Circulation source regions under a warming climate. *Nature Climate Change*, 8(11) :1013–1020, 2018. ISSN 17586798. doi : 10.1038/s41558-018-0316-5. URL <http://dx.doi.org/10.1038/s41558-018-0316-5>.
- C. Lique, A. M. Treguier, B. Blanke, and N. Grima. On the origins of water masses exported along both sides of Greenland : A Lagrangian model analysis. *Journal of Geophysical Research : Oceans*, 115(5) :1–20, 2010. ISSN 21699291. doi : 10.1029/2009JC005316.
- C. Lique, H. L. Johnson, and P. E. D. Davis. On the Interplay between the Circulation in the Surface and the Intermediate Layers of the Arctic Ocean. *Journal of Physical Oceanography*, 45(5) :1393–1409, 2015. ISSN 0022-3670. doi : 10.1175/jpo-d-14-0183.1.
- C. Lique, H. L. Johnson, and Y. Plancherel. Emergence of deep convection in the Arctic Ocean under a warming climate. *Climate Dynamics*, 50(9-10) :3833–3847, 2018. ISSN 14320894. doi : 10.1007/s00382-017-3849-9. URL <http://dx.doi.org/10.1007/s00382-017-3849-9>.
- H. Loeng. Features of the physical oceanographic conditions of the Barents Sea. *Polar Research*, 10(1) :5–18, 1991. ISSN 0800-0395. doi : 10.1111/j.1751-8369.1991.tb00630.x.
- Z. Long and W. Perrie. Changes in Ocean Temperature in the Barents Sea in the Twenty-First Century. *Journal of Climate*, 30(15) :5901–5921, 2017. ISSN 0894-8755. doi : 10.1175/JCLI-D-16-0415.1. URL <http://journals.ametsoc.org/doi/10.1175/JCLI-D-16-0415.1>.
- D. Luo, Y. Xiao, Y. Yao, A. Dai, I. Simmonds, and C. L. Franzke. Impact of ural blocking on winter warm Arctic-cold Eurasian anomalies. Part I : Blocking-induced amplification. *Journal of Climate*, 29(11) :3925–3947, 2016. ISSN 08948755. doi : 10.1175/JCLI-D-15-0611.1.

- G. Madec and The_NEMO_Team. NEMO ocean engine. Technical Report 27, Pôle de modélisation, Institut Pierre Simon Laplace, 2008. URL <http://www.nemo-ocean.eu/About-NEMO/Reference-manuals{\protect\T1\textdollar}{\}%5C{\protect\T1\textdollar}npapers2://publication/uuid/73E7FF17-99BE-4B10-A823-0037C823EF6E>.
- W. Maslowski, D. Marble, W. Walczowski, U. Schauer, J. L. Clement, and A. J. Semtner. On climatological mass, heat, and salt transports through the Barents Sea and Fram Strait from a pan-Arctic coupled ice-ocean model simulation. *Journal of Geophysical Research*, 109(C3) : C03032, 2004. ISSN 0148-0227. doi : 10.1029/2001JC001039.
- T. J. McDougall. Neutral Surfaces. *Journal of Physical Oceanography*, 17 :1950–1964, 1987.
- T. J. McDougall, D. R. Jackett, F. J. Millero, R. Pawlowicz, and P. M. Barker. A global algorithm for estimating Absolute Salinity. *Ocean Science*, 8(6) :1123–1134, 2012. ISSN 18120792. doi : 10.5194/os-8-1123-2012.
- L. Midttun. Formation of dense bottom water in the Barents Sea. *Deep Sea Research Part A, Oceanographic Research Papers*, 32(10) :1233–1241, 1985. ISSN 01980149. doi : 10.1016/0198-0149(85)90006-8.
- B. Moat, S. Josey, and B. Sinhu. Impact of Barents Sea winter air-sea exchanges on Fram Strait dense water transport. *Journal of Geophysical Research : Oceans*, 119(2) :1009–1021, 2014. doi : 10.1002/2013JC009220. Received.
- M. Mori, M. Watanabe, H. Shiogama, J. Inoue, and M. Kimoto. Robust Arctic sea-ice influence on the frequent Eurasian cold winters in past decades. *Nature Geoscience*, 7(12) :869–873, 2014. ISSN 17520908. doi : 10.1038/ngeo2277.
- J. Morison, R. Kwok, C. Peralta-Ferriz, M. Alkire, I. Rigor, R. Andersen, and M. Steele. Changing Arctic Ocean freshwater pathways. *Nature*, 481(7379) :66–70, 2012. ISSN 00280836. doi : 10.1038/nature10705. URL <http://dx.doi.org/10.1038/nature10705>.
- M. Muilwijk, L. H. Smedsrud, M. Ilicak, and H. Drange. Atlantic Water Heat Transport Variability in the 20th Century Arctic Ocean From a Global Ocean Model and Observations. *Journal of Geophysical Research : Oceans*, 2018. ISSN 21699291. doi : 10.1029/2018JC014327.
- T. Nakanowatari, K. Sato, and J. Inoue. Predictability of the barents sea ice in early winter : Remote effects of oceanic and atmospheric thermal conditions from the North Atlantic. *Journal of Climate*, 27(23) :8884–8901, 2014. ISSN 08948755. doi : 10.1175/JCLI-D-14-00125.1.
- D. Notz and J. Stroeve. Observed Arctic sea-ice loss directly follows anthropogenic CO2 emission. *Science*, 354(6313) :747–750, 2016.
- E. Olmedo, C. Gabarró, V. González-Gambau, J. Martínez, J. Ballabrera-Poy, A. Turiel, M. Portabella, S. Fournier, and T. Lee. Seven Years of SMOS sea surface salinity at high latitudes : Variability in Arctic and Sub-Arctic Regions. *Remote Sensing*, 10(11) :1–24, 2018. ISSN 20724292. doi : 10.3390/rs10111772.
- I. H. Onarheim and M. Årthun. Toward an ice-free Barents Sea. *Geophysical Research Letters*, pages 8387–8395, 2017. ISSN 00948276. doi : 10.1002/2017GL074304. URL <http://doi.wiley.com/10.1002/2017GL074304>.
- I. H. Onarheim, T. Eldevik, M. Årthun, R. B. Ingvaldsen, and L. H. Smedsrud. Skillful prediction of Barents Sea ice cover. *Geophysical Research Letters*, 42 :5364–5371, 2015. doi : 10.1002/2015GL064359. Abstract.
- I. H. Onarheim, T. Eldevik, L. H. Smedsrud, and J. C. Stroeve. Seasonal and regional manifestation of Arctic sea ice loss. *Journal of Climate*, 31 :4917–4931, 2018. ISSN 0894-8755. doi : 10.1175/JCLI-D-17-0427.1. URL <http://journals.ametsoc.org/doi/10.1175/JCLI-D-17-0427.1>.

- V. K. Ozhigin, A. G. Trofimov, and V. A. Ivshin. The Eastern Basin Water and currents in the Barents Sea. In *ICES Annual Science Conference 2000 Theme Session L : North Atlantic Processes*, pages 1–19, 2000.
- L. Oziel, J. Sirven, and J. C. Gascard. The Barents Sea frontal zones and water masses variability (1980-2011). *Ocean Science*, 12(1) :169–184, 2016. ISSN 18120792. doi : 10.5194/os-12-169-2016.
- L. Oziel, G. Neukermans, M. Ardyna, C. Lancelot, J.-L. Tison, P. Wassmann, J. Sirven, D. Ruiz-Pino, and J.-C. Gascard. Role for Atlantic inflows and sea ice loss on shifting phytoplankton blooms in the Barents Sea. *Journal of Geophysical Research : Oceans*, 122 :1–19, 2017. doi : 10.1002/2016JC012582. Received.
- L. Padman and S. Erofeeva. A barotropic inverse tidal model for the Arctic Ocean. *Geophysical Research Letters*, 31(2) :2–5, 2004. ISSN 00948276. doi : 10.1029/2003GL019003.
- C. L. Parkinson and D. J. Cavalieri. Arctic sea ice variability and trends, 1979-2006. *Journal of Geophysical Research : Oceans*, 113(7) :1979–2006, 2008. ISSN 21699291. doi : 10.1029/2007JC004558.
- A. R. Parsons, R. H. Bourke, R. D. Muench, C.-S. Chiu, J. F. Lynch, J. H. Miller, A. J. Plueddemann, and R. Pawlowicz. The Barents Sea Polar Front in summer. *Journal of Geophysical Research*, 101(C6) :14201–14221, 1996. ISSN 0148-0227. doi : 10.1029/96JC00119. URL <http://doi.wiley.com/10.1029/96JC00119>.
- C. Peralta-Ferriz, J. H. Morison, J. M. Wallace, J. A. Bonin, and J. Zhang. Arctic ocean circulation patterns revealed by GRACE. *Journal of Climate*, 27(4) :1445–1468, 2014. ISSN 08948755. doi : 10.1175/JCLI-D-13-00013.1.
- C. Peralta-Ferriz, J. H. Morison, and J. M. Wallace. Proxy representation of Arctic ocean bottom pressure variability : Bridging gaps in GRACE observations. *Geophysical Research Letters*, 43 (17) :9183–9191, 2016. ISSN 19448007. doi : 10.1002/2016GL070137.
- V. Petoukhov and V. A. Semenov. A link between reduced Barents-Kara sea ice and cold winter extremes over northern continents. *Journal of Geophysical Research Atmospheres*, 115(21) : 1–11, 2010. ISSN 01480227. doi : 10.1029/2009JD013568.
- I. V. Polyakov, A. V. Pnyushkov, M. B. Alkire, I. M. Ashik, T. M. Baumann, E. C. Carmack, I. Goszczko, J. Guthrie, V. V. Ivanov, T. Kanzow, R. Krishfield, R. Kwok, A. Sundfjord, J. Morison, R. Rember, and A. Yulin. Greater role for Atlantic inflows on sea-ice loss in the Eurasian Basin of the Arctic Ocean. *Science*, 291(April) :285–291, 2017. ISSN 10959203. doi : 10.1126/science.aai8204.
- I. V. Polyakov, A. V. Pnyushkov, and E. C. Carmack. Stability of the arctic halocline : A new indicator of arctic climate change. *Environmental Research Letters*, 13(12), 2018. ISSN 17489326. doi : 10.1088/1748-9326/aaec1e.
- L. J. Pratt. Recent progress on understanding the effects of rotation in models of sea straits. *Deep-Sea Research Part II : Topical Studies in Oceanography*, 51(4-5) :351–369, 2004. ISSN 09670645. doi : 10.1016/j.dsr2.2003.06.005.
- J. Proudman. On the motion of solids in a liquid possessing vorticity. *Proceedings of the Royal Society London A*, 92 :408–424, 1916. ISSN 0034-6861. doi : 10.1103/RevModPhys.4.87.
- H. C. Regan, C. Lique, and T. W. K. Armitage. The Beaufort Gyre Extent, Shape, and Location Between 2003 and 2014 From Satellite Observations. *Journal of Geophysical Research : Oceans*, pages 1–19, 2019. ISSN 21699275. doi : 10.1029/2018JC014379. URL <http://doi.wiley.com/10.1029/2018JC014379>.

- M. Reigstad, P. Wassmann, C. Wexels Riser, S. Øygarden, and F. Rey. Variations in hydrography, nutrients and chlorophyll a in the marginal ice-zone and the central Barents Sea. *Journal of Marine Systems*, 38(1-2) :9–29, 2002. ISSN 09247963. doi : 10.1016/S0924-7963(02)00167-7.
- K. Richter, J. E. Ø. Nilsen, and H. Drange. Contributions to sea level variability along the Norwegian coast for 1960-2010. *Journal of Geophysical Research : Oceans*, 117(5) :1–12, 2012. ISSN 21699291. doi : 10.1029/2011JC007826.
- T. P. Rippeth, B. J. Lincoln, Y. D. Lenn, J. A. Green, A. Sundfjord, and S. Bacon. Tide-mediated warming of Arctic halocline by Atlantic heat fluxes over rough topography. *Nature Geoscience*, 8(3) :191–194, 2015. ISSN 17520908. doi : 10.1038/ngeo2350.
- M. Rojo, C. Claud, P. E. Mallet, G. Noer, A. M. Carleton, and M. Vicomte. Polar low tracks over the Nordic Seas : A 14-winter climatic analysis. *Tellus, Series A : Dynamic Meteorology and Oceanography*, 67(1), 2015. ISSN 16000870. doi : 10.3402/tellusa.v67.24660.
- F. Roquet, G. Madec, T. J. McDougall, and P. M. Barker. Accurate polynomial expressions for the density and specific volume of seawater using the TEOS-10 standard. *Ocean Modelling*, 90 :29–43, 2015. ISSN 14635003. doi : 10.1016/j.ocemod.2015.04.002. URL <http://dx.doi.org/10.1016/j.ocemod.2015.04.002>.
- C. Rousset, M. Vancoppenolle, G. Madec, T. Fichefet, S. Flavoni, A. Barthélemy, R. Benshila, J. Chanut, C. Levy, S. Masson, and F. Vivier. The Louvain-La-Neuve sea ice model LIM3.6 : Global and regional capabilities. *Geoscientific Model Development*, 8(10) :2991–3005, 2015. ISSN 19919603. doi : 10.5194/gmd-8-2991-2015.
- B. Rudels, L. G. Anderson, and E. P. Jones. Formation and evolution of the surface mixed layer and halocline of the Arctic Ocean. *Journal of Geophysical Research*, 101 :8807–8821, 1996. ISSN 2156-2202. doi : 10.1029/96JC00143.
- B. Rudels, R. D. Muench, J. Gunn, U. Schauer, and H. J. Friedrich. Evolution of the Arctic Ocean boundary current north of the Siberian shelves. *Journal of Marine Systems*, 25(1) :77–99, 2000. ISSN 09247963. doi : 10.1016/S0924-7963(00)00009-9.
- B. Rudels, M. Korhonen, U. Schauer, S. Pisarev, B. Rabe, and A. Wisotzki. Circulation and transformation of Atlantic water in the Eurasian Basin and the contribution of the Fram Strait inflow branch to the Arctic Ocean heat budget. *Progress in Oceanography*, 132 :128–152, 2015. ISSN 00796611. doi : 10.1016/j.pocean.2014.04.003. URL <http://dx.doi.org/10.1016/j.pocean.2014.04.003>.
- C. Sakumura, S. Bettadpur, and S. Bruinsma. Ensemble prediction and intercomparison analysis of GRACE time-variable gravity field models. *Geophysical Research Letters*, 41(5) :1389–1397, 2014. ISSN 19448007. doi : 10.1002/2013GL058632.
- E. M. Samuelsen, S. Løset, and K. Edvardsen. Marine icing observed on KV Nordkapp during a cold air outbreak with a developing polar low in the Barents Sea. *Proceedings of the 23rd International Conference on Port and Ocean Engineering under Arctic Conditions*, 87 :1–14, 2015.
- A. B. Sandø, J. E. Ø. Nilsen, Y. Gao, and K. Lohmann. Importance of heat transport and local air-sea heat fluxes for Barents Sea climate variability. *Journal of Geophysical Research : Oceans*, 115(7), 2010. ISSN 21699291. doi : 10.1029/2009JC005884.
- U. Schauer, R. D. Muench, B. Rudels, and L. Timokhov. Impact of eastern Arctic shelf waters on the Nansen Basin intermediate layers. *Journal of Geophysical Research*, 102(C2) :3371, 1997. ISSN 0148-0227. doi : 10.1029/96JC03366.

- U. Schauer, H. Loeng, B. Rudels, V. K. Ozhigin, and W. Dieck. Atlantic Water flow through the Barents and Kara Seas. *Deep-Sea Research Part I : Oceanographic Research Papers*, 49(12) : 2281–2298, 2002. ISSN 09670637. doi : 10.1016/S0967-0637(02)00125-5.
- P. Schlichtholz. Local wintertime tropospheric response to oceanic heat anomalies in the Nordic seas area. *Journal of Climate*, 27(23) :8686–8706, 2014. ISSN 08948755. doi : 10.1175/JCLI-D-13-00763.1.
- P. Schlichtholz and M. N. Houssais. Forcing of oceanic heat anomalies by air-sea interactions in the Nordic Seas area. *Journal of Geophysical Research : Oceans*, 116(1) :1–21, 2011. ISSN 21699291. doi : 10.1029/2009JC005944.
- S. Schmidtko, G. C. Johnson, and J. M. Lyman. MIMOC : A global monthly isopycnal upper-ocean climatology with mixed layers. *Journal of Geophysical Research : Oceans*, 118(4) : 1658–1672, 2013. ISSN 21699291. doi : 10.1002/jgrc.20122.
- J. A. Screen and I. Simmonds. The central role of diminishing sea ice in recent Arctic temperature amplification. *Nature*, 464(7293) :1334–1337, 2010a. ISSN 0028-0836. doi : 10.1038/nature09051. URL <http://dx.doi.org/10.1038/nature09051>.
- J. A. Screen and I. Simmonds. Increasing fall-winter energy loss from the Arctic Ocean and its role in Arctic temperature amplification. *Geophysical Research Letters*, 37(16) :1–5, 2010b. ISSN 00948276. doi : 10.1029/2010GL044136.
- O. H. Segtnan, T. Furevik, and A. D. Jenkins. Heat and freshwater budgets of the Nordic seas computed from atmospheric reanalysis and ocean observations. *Journal of Geophysical Research : Oceans*, 116(11) :1–17, 2011. ISSN 21699291. doi : 10.1029/2011JC006939.
- M. C. Serreze and R. G. Barry. Processes and impacts of Arctic amplification : A research synthesis. *Global and Planetary Change*, 77(1-2) :85–96, 2011. ISSN 09218181. doi : 10.1016/j.gloplacha.2011.03.004. URL <http://dx.doi.org/10.1016/j.gloplacha.2011.03.004>.
- M. C. Serreze, A. P. Barrett, J. C. Stroeve, D. N. Kindig, and M. M. Holland. The emergence of surface-based Arctic amplification. *The Cryosphere*, 3 :11–19, 2009. ISSN 00243477.
- F. Sévellec, A. V. Fedorov, and W. Liu. Arctic sea-ice decline weakens the Atlantic Meridional Overturning Circulation. *Nature Climate Change*, 7(8) :604–610, 2017. ISSN 17586798. doi : 10.1038/NCLIMATE3353.
- G. I. Shapiro. Dense water cascading off the continental shelf. *Journal of Geophysical Research*, 108(C12) :3390, 2003. ISSN 0148-0227. doi : 10.1029/2002JC001610. URL <http://doi.wiley.com/10.1029/2002JC001610>.
- M. Sigmond, M. C. Reader, G. M. Flato, W. J. Merryfield, and A. Tivy. Skillful seasonal forecasts of Arctic sea ice retreat and advance dates in a dynamical forecast system. *Geophysical Research Letters*, 43(24) :12,457–12,465, 2016. ISSN 19448007. doi : 10.1002/2016GL071396.
- I. Simmonds and K. Keay. Extraordinary September Arctic sea ice reductions and their relationships with storm behavior over 1979-2008. *Geophysical Research Letters*, 36(19) :1–5, 2009. ISSN 00948276. doi : 10.1029/2009GL039810.
- R. K. Singh, M. Maheshwari, S. R. Oza, and R. Kumar. Long-term variability in Arctic sea surface temperatures. *Polar Science*, 7(3-4) :233–240, 2013. ISSN 18739652. doi : 10.1016/j.polar.2013.10.003. URL <http://dx.doi.org/10.1016/j.polar.2013.10.003>.
- Ø. Skagseth. Recirculation of Atlantic Water in the western Barents Sea. *Geophysical Research Letters*, 35(11) :1–5, 2008. ISSN 00948276. doi : 10.1029/2008GL033785.

- O. Skagseth, K. F. Drinkwater, and E. Terrile. Wind-and buoyancy-induced transport of the Norwegian Coastal Current in the Barents Sea. *Journal of Geophysical Research : Oceans*, 116(8), 2011. ISSN 21699291. doi : 10.1029/2011JC006996.
- J. Skardhamar, Ø. Skagseth, and J. Albretsen. Diurnal tides on the Barents Sea continental slope. *Deep-Sea Research Part I : Oceanographic Research Papers*, 97 :40–51, 2015. ISSN 09670637. doi : 10.1016/j.dsr.2014.11.008. URL <http://dx.doi.org/10.1016/j.dsr.2014.11.008>.
- D. Slagstad and T. A. McClimans. Modeling the ecosystem dynamics of the Barents sea including the marginal ice zone : I. Physical and chemical oceanography. *Journal of Marine Systems*, 58(1-2) :1–18, 2005. ISSN 09247963. doi : 10.1016/j.jmarsys.2005.05.005.
- L. H. Smedsrud, R. Ingvaldsen, J. E. Ø. Nilsen, and Ø. Skagseth. Heat in the Barents Sea : transport, storage, and surface fluxes. *Ocean Science*, 6(1) :219–234, 2010. ISSN 1812-0792. doi : 10.5194/os-6-219-2010.
- L. H. Smedsrud, I. Esau, R. B. Ingvaldsen, T. Eldevik, P. M. Haugan, C. Li, V. S. Lien, A. Olsen, A. M. Omar, B. Risebrobakken, A. B. Sandø, V. A. Semenov, and S. A. Sorokina. The role of the Barents Sea in the Arctic climate system. *Reviews of Geophysics*, 51(3) :415–449, 2013. ISSN 87551209. doi : 10.1002/rog.20017.
- T. Snape. Decline of Arctic Sea Ice : Evaluation and weighting of CMIP5 projections. *Journal of Geophysical Research : Atmospheres*, 119(2) :546–554, 2013. ISSN 2169897X. doi : 10.1002/2013JD020593. Received.
- A. Sorteberg and B. Kvingedal. Atmospheric forcing on the Barents Sea winter ice extent. *Journal of Climate*, 19(19) :4772–4784, 2006. ISSN 08948755. doi : 10.1175/JCLI3885.1.
- M. Steele and W. Ermold. Steric sea level change in the Northern Seas. *J. Climate*, 20 :403–417, 2007.
- M. Steele and W. Ermold. Loitering of the retreating sea ice edge in the Arctic Seas. *Journal of Geophysical Research : Oceans*, 120 :7699–7721, 2015. ISSN 21699275. doi : 10.1002/2015JC010969.
- K. D. Stewart and T. W. N. Haine. Thermobaricity in the Transition Zones between Alpha and Beta Oceans. *Journal of Physical Oceanography*, 46(6) :1805–1821, 2016. ISSN 0022-3670. doi : 10.1175/JPO-D-16-0017.1. URL <http://journals.ametsoc.org/doi/10.1175/JPO-D-16-0017.1>.
- P. J. Stoll, R. G. Graversen, G. Noer, and K. Hodges. An objective global climatology of polar lows based on reanalysis data. *Quarterly Journal of the Royal Meteorological Society*, 144(716) :2099–2117, 2018. ISSN 1477870X. doi : 10.1002/qj.3309.
- V. H. Strass and E. M. Nöthig. Seasonal shifts in ice edge phytoplankton blooms in the Barents Sea related to the water column stability. *Polar Biology*, 16(6) :409–422, 1996. ISSN 07224060. doi : 10.1007/BF02390423.
- E. Svendsen, M. Skogen, P. Budgell, G. Huse, J. Erik Stiansen, B. Ådlandsvik, F. Vikebø, L. Asplin, and S. Sundby. An ecosystem modeling approach to predicting cod recruitment. *Deep-Sea Research Part II : Topical Studies in Oceanography*, 54(23-26) :2810–2821, 2007. ISSN 09670645. doi : 10.1016/j.dsr2.2007.07.033.
- S. Swart, S. Speich, I. J. Ansorge, and J. R. Lutjeharms. An altimetry-based gravest empirical mode south of Africa : 1. Development and validation. *Journal of Geophysical Research : Oceans*, 115(3) :1–19, 2010. ISSN 21699291. doi : 10.1029/2009JC005299.
- G. I. Taylor. Motion of solids in fluids when the flow is not irrotational. *Proceedings of the Royal Society London A*, 93 :92–113, 1917.

- J. Terhaar, J. C. Orr, M. Gehlen, C. Ethé, and L. Bopp. Model constraints on the anthropogenic carbon budget of the Arctic Ocean. *Biogeosciences Discussions*, pages 1–36, 2018. doi : 10.5194/bg-2018-283.
- R. E. Thomson and W. J. Emery. *Data analysis methods in physical oceanography*. Newnes, third edition, 2014.
- A. M. Treguier, J. Deshayes, J. Le Sommer, C. Lique, G. Madec, T. Penduff, J. M. Molines, B. Barnier, R. Bourdalle-Badie, and C. Talandier. Meridional transport of salt in the global ocean from an eddy-resolving model. *Ocean Science*, 10(2) :243–255, 2014. ISSN 18120792. doi : 10.5194/os-10-243-2014.
- K. E. Trenberth. The Definition of El Nino. *Bulletin of the American Meteorological Society*, 78(12) :2771–2778, 1997. ISSN 08948755. doi : 10.1175/1520-0442(1996)009<0161:FALMFV>2.0.CO;2.
- K. E. Trenberth and D. J. Shea. Atlantic hurricanes and natural variability in 2005. *Geophysical Research Letters*, 33(12) :1–4, 2006. ISSN 00948276. doi : 10.1029/2006GL026894.
- S. Våge, S. L. Basedow, K. S. Tande, and M. Zhou. Physical structure of the Barents Sea Polar Front near Storbanken in August 2007. *Journal of Marine Systems*, 130(August 2007) :256–262, 2014. ISSN 09247963. doi : 10.1016/j.jmarsys.2011.11.019. URL <http://dx.doi.org/10.1016/j.jmarsys.2011.11.019>.
- H. van Loon and J. C. Rogers. The Seesaw in Winter Temperatures between Greenland and Northern Europe. Part 1 : General Description. *Monthly Weather Review*, 106 :296–310, 1978.
- M. Vancoppenolle, T. Fichefet, H. Goosse, S. Bouillon, G. Madec, and M. A. M. Maqueda. Simulating the mass balance and salinity of Arctic and Antarctic sea ice. 1. Model description and validation. *Ocean Modelling*, 27(1-2) :33–53, 2009. ISSN 14635003. doi : 10.1016/j.ocemod.2008.10.005. URL <http://dx.doi.org/10.1016/j.ocemod.2008.10.005>.
- S. A. Venegas and L. A. Mysak. Is there a dominant timescale of natural climate variability in the Arctic? *Journal of Climate*, 13(19) :3412–3434, 2000. ISSN 08948755. doi : 10.1175/1520-0442(2000)013<3412:ITADTO>2.0.CO;2.
- T. Vihma. Effects of Arctic Sea Ice Decline on Weather and Climate : A Review. *Surveys in Geophysics*, 35 :1175–1214, 2014. ISSN 01693298. doi : 10.1007/s10712-014-9284-0.
- D. L. Volkov and M. I. Pujol. Quality assessment of a satellite altimetry data product in the Nordic, Barents, and Kara seas. *Journal of Geophysical Research : Oceans*, 117(3) :1–18, 2012. ISSN 21699291. doi : 10.1029/2011JC007557.
- D. L. Volkov, F. W. Landerer, and S. A. Kirillov. The genesis of sea level variability in the Barents Sea. *Continental Shelf Research*, 66 :92–104, 2013. ISSN 02784343. doi : 10.1016/j.csr.2013.07.007. URL <http://dx.doi.org/10.1016/j.csr.2013.07.007>.
- J. Wahr, M. Molenaar, and F. Bryan. Time variability of the Earth’s gravity field : Hydrological and oceanic effects and their possible detection using GRACE. *Journal of Geophysical Research*, 103(B12) :30205–30229, 1998.
- J. E. Walsh, V. Kattsov, D. Portis, and V. Meleshko. Arctic Precipitation and Evaporation : Model Results and Observational Estimates. *Journal of Climate*, 11 :72–87, 1998.
- J. E. Walsh, F. Fetterer, J. Scott Stewart, and W. L. Chapman. A database for depicting Arctic sea ice variations back to 1850. *Geographical Review*, 107(1) :89–107, 2017. ISSN 19310846. doi : 10.1111/j.1931-0846.2016.12195.x.

- M. Wang and J. E. Overland. A sea ice free summer Arctic within 30 years : An update from CMIP5 models. *Geophysical Research Letters*, 39(17) :2–6, 2012. ISSN 00948276. doi : 10.1029/2012GL052868.
- P. Weatherall, K. M. Marks, M. Jakobsson, T. Schmitt, S. Tani, J. E. Arndt, M. Rovere, D. Chayes, V. Ferrini, and R. Wigley. A new digital bathymetric model of the world’s oceans. *Earth and Space Science*, 2 :331–345, 2015. ISSN 23335084. doi : 10.1002/2015EA000107. Received.
- C. J. White, T. W. Tanton, and D. W. Rycroft. The Impact of Climate Change on the Water Resources of the Amu Darya Basin in Central Asia. *Water Resources Management*, 28(15) : 5267–5281, 2014. ISSN 09204741. doi : 10.1007/s11269-014-0716-x.
- J. Yang. The Arctic and Subarctic Ocean Flux of Potential Vorticity and the Arctic Ocean Circulation*. *Journal of Physical Oceanography*, 35(12) :2387–2407, 2005. ISSN 0022-3670. doi : 10.1175/JPO2819.1.
- J. Yang and J. F. Price. Water-mass formation and potential vorticity balance in an abyssal ocean circulation. *Journal of Marine Research*, 58 :789–808, 2000. ISSN 00222402. doi : 10.1357/002224000321358918.
- X. Y. Yang, X. Yuan, and M. Ting. Dynamical link between the Barents-Kara sea ice and the arctic oscillation. *Journal of Climate*, 29(14) :5103–5122, 2016. ISSN 08948755. doi : 10.1175/JCLI-D-15-0669.1.
- E. Yankovsky and S. Legg. Symmetric and Baroclinic Instability in Dense Shelf Overflows. *Journal of Physical Oceanography*, 49(1) :39–61, 2019. ISSN 0022-3670. doi : 10.1175/jpo-d-18-0072.1.
- I. Yashayaev and D. Seidov. The role of the Atlantic Water in multidecadal ocean variability in the Nordic and Barents Seas. *Progress in Oceanography*, 132(December 2014) :68–127, 2015. ISSN 00796611. doi : 10.1016/j.pocean.2014.11.009. URL <http://dx.doi.org/10.1016/j.pocean.2014.11.009>.
- S. Yasunaka, A. Murata, E. Watanabe, M. Chierici, A. Fransson, S. van Heuven, M. Hoppema, M. Ishii, T. Johannessen, N. Kosugi, S. K. Lauvset, J. T. Mathis, S. Nishino, A. M. Omar, A. Olsen, D. Sasano, T. Takahashi, and R. Wanninkhof. Mapping of the air–sea CO₂ flux in the Arctic Ocean and its adjacent seas : Basin-wide distribution and seasonal to interannual variability. *Polar Science*, 10(3) :323–334, 2016. ISSN 18739652. doi : 10.1016/j.polar.2016.03.006. URL <http://dx.doi.org/10.1016/j.polar.2016.03.006>.
- P. Yiou and M. Nogaj. Extreme climatic events and weather regimes over the North Atlantic : When and where? *Geophysical Research Letters*, 31(7) :1–4, 2004. ISSN 00948276. doi : 10.1029/2003GL019119.
- M. Zahn and H. Von Storch. Decreased frequency of North Atlantic polar lows associated with future climate warming. *Nature*, 467(7313) :309–312, 2010. ISSN 14764687. doi : 10.1038/nature09388. URL <http://dx.doi.org/10.1038/nature09388>.
- L. Zakhirova. The International Politics of Water Security in Central Asia, 2013. ISSN 09668136. URL <http://dx.doi.org/10.1080/09668136.2013.848647>.

Annexe A

Supplementary Materials for Chapter 3

A.1 Satellite Based T-S Profiles

By rearranging the equations for *in situ* measurement of thermosteric and halosteric height we show a time-dependant temperature and salinity anomaly profile can then be derived at each grid point from a mean temperature/salinity profile and the thermosteric/halosteric height respectively :

$$T(z, t) = \bar{T}(z) + \frac{1}{\bar{\alpha}(z)} \frac{\partial \eta_T(t)}{\partial z} \quad (\text{A.1})$$

$$S(z, t) = \bar{S}(z) - \frac{1}{\bar{\beta}(z)} \frac{\partial \eta_S(t)}{\partial z} \quad (\text{A.2})$$

The combination of thermosteric, halosteric height and a mean T - S profile allows the determination of time-varying temperature and salinity profile at each grid point (Eq. A.1 and A.2). Differentiating the integrated water column value in Eq. A.1 and A.2 result in a discrete description of the original values, and would be expected to degrade the original signal. Next, we quantify how much the signal is degraded by this method. Figure A.1c,f illustrates the results of our method at our example location, and reveal that . the structure of the satellite profile does not vary in time. Figure A.1a,b quantifies how much vertical structure in a profile is lost through this method. In this figure, regression values are calculated between the satellite T - S data and the *in situ* T - S data at each depth level then averaged over the water column. In general this method produces a T - S profile with regression values greater than 0.8 across the Barents Sea. When the satellite-derived thermosteric and halosteric components are used to calculate the T - S profiles the regression values are lower because the satellite T - S profile inherits the differences between the satellite and *in situ* data already discussed in Section 3.3 (Figure A.1c,d). The spatial patterns of the satellite derived temperature and salinity are consistent with EN4 due to satellite measurements being used as anomalies relative to a mean profile from EN4.

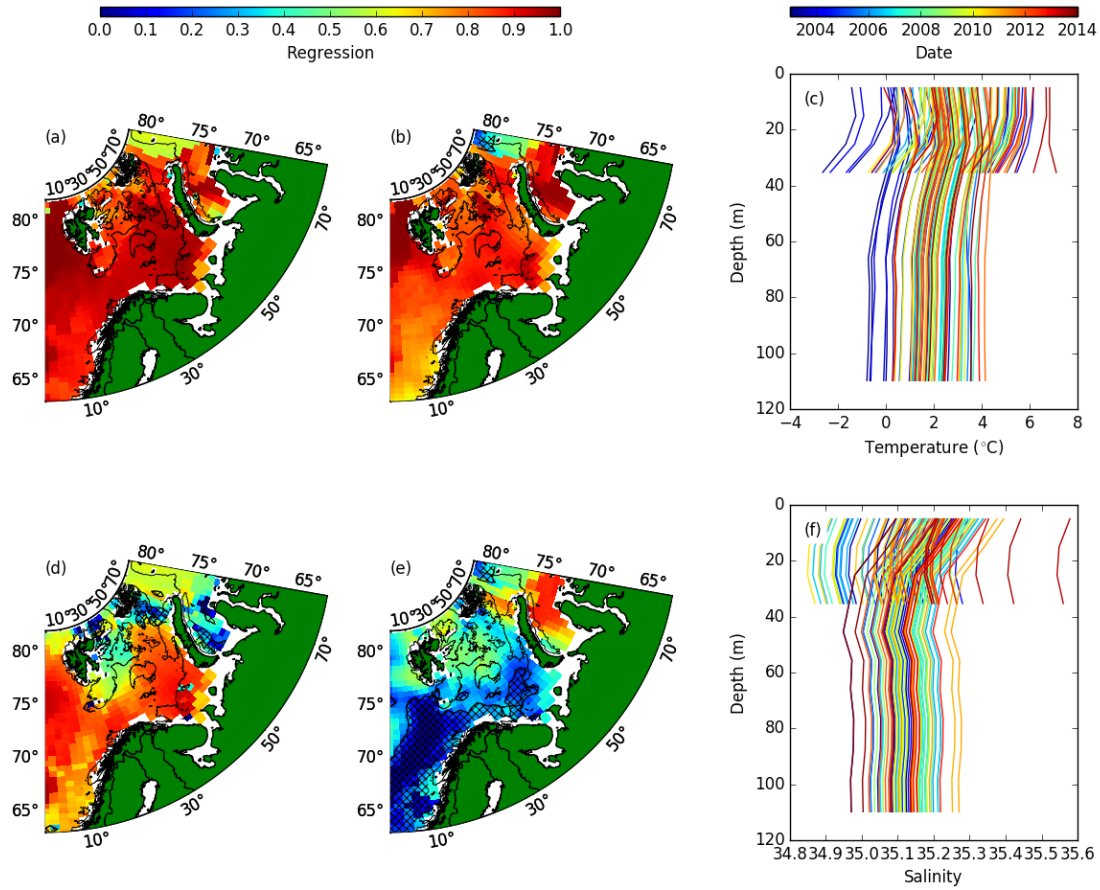


FIGURE A.1 – Depth averaged regression values between the surface and optimum integration depth found in Figure 3.2 of *in situ* (a) thermosteric height converted to a temperature profile against EN4 temperature profile, (b) halosteric height converted to a salinity profile regressed against EN4 salinity profile. (d) and (e) are the same as (a) and (b) but for regression between the satellite T-S profile and the respective EN4 profile at each grid point. Hatching shows areas with significance $< 95\%$. White, coastal areas show where data is not available. Satellite derived, time varying temperature profiles (c) and salinity profiles (f) for the location marked with a black cross on Figure 3.3b. The colour of the line shows the date. Shallow profiles are for the strong stratification season, deep profiles are for the weak stratification season.

Titre : Changements climatiques en mer Barents : Interactions glace-océan, formation et variabilité de la masse d'eau

Mots clés : Barents Sea Water, Front Polaire, Banquise, Satellite, Modélisation

Résumé : L'étendue hivernale de la banquise en mer de Barents n'a cessé de diminuer, et un certain nombre d'études suggèrent que cette diminution pourrait coïncider avec des hivers très froids en Europe et Asie. L'eau Atlantique (AW) transportée vers la mer de Barents, se réchauffe. En mer de Barents, l'AW se transforme en Barents Sea Water (BSW), plus froide et moins salée. Etudier cette dernière nous permet d'en savoir plus sur l'influence de la saisonnalité de la banquise Arctique sur la stratification et la circulation de l'océan.

Tout d'abord, nous utilisons des observations satellites pour localiser le Front Polaire (PF) qui matérialise la limite entre la BSW et l'eau Arctique. Nous établissons que l'étendue de la banquise était indépendante du PF jusqu'au milieu des années 2000, jusqu'à ce que le réchauffement de l'AW commence à limiter l'extension de la banquise hivernale au sud du

front.

Ensuite, en combinant données satellites et *in situ*, nous montrons que l'on peut surveiller 'à distance' les propriétés de la BSW : les variations de la température de surface de l'océan sont ainsi corrélées à celles du contenu en chaleur de la mer de Barents qui, associées à celles de la hauteur stérique, permettent également d'estimer son contenu en eau douce.

Pour finir, nous utilisons un modèle à haute résolution pour calculer les bilans de volume, transport et flux des masses d'eau. Le volume de la BSW atteint un minimum en 1990 et 2004 : l'étendue de glace de mer hivernale ayant fondue l'été suivant était alors conséquente, résultant notamment d'une masse d'AW plus froide. L'événement de 2004 a permis une entrée massive d'AW, de plus en plus chaude, dans la mer de Barents.

Title : Climate change in the Barents Sea : Ice-ocean interactions, water mass formation and variability

Keywords : Barents Sea Water, Polar Front, Sea ice, Satellite, Model

Abstract : Winter sea ice has declined in the Barents Sea and there is growing evidence that the low sea ice here coincides with cold, winter surface air temperature in Europe and Asia. Atlantic Water (AW) transported into the Barents Sea is warming and its temperature variability is correlated with variability in sea ice extent. As AW extends into the Barents Sea it is modified into a cooler, fresher water mass called Barents Sea Water (BSW). There are limited observations of BSW despite its importance in the Arctic Ocean system, leading to the question, how does the seasonal sea ice impact ocean stratification and mean flow ?

First, satellite observations are used to find the Polar Front, a water mass boundary between BSW and fresher Arctic Water to the north. The sea ice extent was found to be independent of the Polar Front until the mid-2000s when warming AW prevented the ex-

tension of winter sea ice south of the front.

Second, by combining satellite and *in situ* data, it is shown that sea surface temperature can approximate heat content in the Barents Sea. Using heat content with satellite steric height, freshwater content can also be estimated, showing the potential for remote monitoring of BSW properties.

Third, a high-resolution model is used to calculate the volume, transport and flux budgets within the AW and BSW domain south of the Polar Front. The model shows BSW volume minimum years in 1990 and 2004. Both events were preceded by extensive winter sea ice and substantial summer sea ice melt, a result of preceding, cool AW. The event in 2004 was more extreme and allowed warming AW a greater volume in the Barents Sea.